Università degli Studi di Perugia

Dottorato di Ricerca in Fisica
XVI Ciclo

Tesi di dottorato

Measurement of the Ξ^0 beta decay Branching Ratio in the experiment NA48/I at CERN

Candidato:
Mauro Piccini

Tutore:

Prof. **A. Nappi**

Coordinatore del dottorato:

Prof. **P. Sodano**

A. A. 2002-2003

Contents

Introduction

The study of hadron beta decays gives extraordinary opportunities in understanding the interplay between weak interaction and the hadron structure determined by the strong interaction. Both meson and baryon beta decays are useful in that sense.

The extraction of information from meson beta decay is simpler because only two quarks are involved and because the general structure of the decay amplitude involves a smaller number of form factors. Experimentally the meson beta decays have usually large branching ratios and the collection of adequate statistics is easier with the exception of $\pi^+ \to \pi^0 e^+ \nu_e$.

For what concerns hadron beta decays, only the neutron always decays through a beta decay; for all other hadrons, and in particular for hyperons [1] the beta decays have a small BR, of the order of percent or less. Another difficulty in the study of hyperon beta decays usually is the presence of high background.

On the other hand the fact that hyperons carry spin 1/2 makes the hadron part of their semileptonic decay matrix element richer in information on strong interaction than the corresponding one of semileptonic decays of spin zero mesons. In addition, hyperons carry strangeness, and the evidence of differences with respect to neutron beta decay should give precious information on the expected breakdown of the flavor SU(3) simmetry. Once hadronic effects are dealt with, the study of these channels is also useful to constrain the ratio of the coupling constants for strangeness changing and conserving weak currents (usually parametrized by the constant V_{us}).

These arguments explain the interest of the physics community in the study of

[1] hyperon is the name of hadrons carrying at least one s quark.

hyperon beta decays between 1960 and 1985.

After that period there was a lack of relevant experiments on hyperon physics essentially due to the difficulties to collect statistics and to the difficulties in the interpretation of the experimental results.

In the last decade a new interest on hyperon beta decays has grown. There are several motivations explaining this trend:

- New methods for the computation of strong interaction effects are now available and through these methods it is possible to exctract more precise predictions of the form factors.

- The development of detection and data acquisition technologies and the possibility to have high intensity beams allow to collect important statistics on hyperon semileptonic decays. New beta decays become now accessible, like, e.g., the case of the Ξ^0 semileptonic decays, the channel studied in this work.

- There are some difficulties in accommodating the data on neutron and kaon beta decays in the framework of the Cabibbo-Kobayashi-Maskawa (CKM) quark mixing matrix. More information on this item are now desidarable.

- The flavor symmetry SU(3) is expected to be broken due to differences in the characteristics of quarks with different flavor interacting through the strong force. Nevertheless up to now there is no clear and direct evidence of this breakdown. The presence of a *strange* quark in the hyperons of the fundamental baryon octect, makes those particles a privileged system for the study of SU(3).

In this context the work I'm going to describe is the determination of the branching ratio of the beta decay of the neutral cascade, $\Xi^0 \to \Sigma^+ e^- \bar{\nu}_e$. From the experimental side, the Ξ^0 beta decay is interesting from many points of view but, up to now, its contribution , e.g., to the determination of V_{us} is not very significant, due to the large errors, still limited by statistics.

On the other hand it has a clear signature for its recostruction: the possibility to recostruct the mass of the emitted hyperon Σ^+ from the decay $\Sigma^+ \rightarrow p\pi^0$, is enough to reduce the background substantially, since the 2 body decay with the same outgoing hyperon produced ($\Xi^0 \rightarrow \Sigma^+ \pi^-$) is kinematically forbidden.

The result is a better background rejection and a simplification of the study of the decay rate and of the kinematic variables with respect to other hyperon beta decays (for instance the study of the Λ beta decay $\Lambda \rightarrow pe^-\overline{\nu}$ is affected by the background coming from the non-leptonic decay $\Lambda \rightarrow p\pi^-$) .

After the successful study of direct CP violation[1] in $K^0 \rightarrow \pi\pi$ (1997-1999 and 2001 runs) the NA48 collaboration has started a new research program on K^0_S rare decays and neutral hyperons physics (NA48/I) with two periods of data taking in 2000 and 2002 years. In fact the proton beam, incoming from SPS and impinging on the "so called" K^0_S target, is also a good source of hyperon particles, with fluxes sufficient to study rare decays.

In the 2002 run NA48 has collected the largest world sample of Ξ^0 beta decay events. In the following, I will use this sample to measure the BR and to extract the Cabibbo angle V_{US} . Now I give a brief summary of this work.

In the first chapter I introduce the phenomenology of hyperon beta decays. I will work in the V-A theory framework and I will go back to the standard electroweak theory only to extract the radiative corrections to the transition amplitude. Some details will be given on the effect of the polarization of the decaying hyperon. The decaying Ξ_0s produced in our beam are expected to have a small but non-negligible polarization. We will see that such polarization implies some effects also on the decay of the emitted Σ^+ .

In chapter 2 I will describe the beam configuration for the 2002 run and all the subdetectors composing the experimental apparatus of the NA48 detector where the data to study the Ξ^0 beta decay were collected.

One of the main difficulties to collect the desired events is their online selection. In fact the interaction rate in the experimental region is very high and the identification of the events is crucial. To reach that aim NA48 uses 3 levels of trigger, which are described in chapter 3 together with the data acquisition system.

In chapter 4 I will describe the MonteCarlo simulation used to estimate the acceptance for the signal and for the normalization channel ($\Xi^0 \rightarrow \Lambda\pi^0$). Some work has been necessary to adjust the standard NA48 MC for the study of Ξ^0 physics. In particular the generated Ξ^0 spectrum plays a fundamental role for a reliable simulation of our decays. I will also show the modifications applied to the beam geometry to better fit the real data distributions. I will finally compare some relevant distributions between data and MC.

The chapter 5 contains the analysis description. The selection and recostruction strategies for both signal and normalization channels are described. Then I show the measurement of trigger efficiencies and our estimations for the acceptances. A study of the residual background in both the data and the normalization channel has been performed and it is reported. Finally, from the final sample, I extract the measurement for the Ξ^0 beta decay branching ratio and at the end of the chapter I list the systematic effects studied and their effect on the final result. The V_{us} extraction is model dependent and I will report a preliminary determination of this parameter under simplifying hypotheses.

The results reported in this thesis are still preliminary since some parts of the analysis are still in progress. Therefore the results are shown with the proviso that they are not official results of the collaboration but only entail my personal responsibility.

Chapter 1

Introduction to hyperon beta decays

We are interested to study the decay:

$$\mathbf{B} \rightarrow \mathbf{b} \mathbf{l}^{-} \overline{\nu}_{\mathbf{l}} \tag{1.1}$$

Where B indicates the decaying hyperon (the Ξ^0 in our case), b the emitted hyperon (the Σ^+), l^- the emitted lepton and $\overline{\nu}_l$ the associated neutrino.

In this chapter first I will introduce the reasons of interest of hyperon beta decays, explaining the open issues both in theoretical and experimental approach.

Then I will focus on the phenomenological description of Ξ^0 beta decay. Working in the V-A theory framework I will show formulas for the transition amplitudes. These formulas will be used as an ingredient for the Monte-Carlo generator, described in chapter IV, that I have developed in order to calculate the acceptance corrections.

Then I will show the radiative corrections (treated instead in the standard electroweak theory) and the corrections for the q^2 dependence of form factors.

I will introduce the more general case of the decay of a polarized hyperon and I will show the effect of that polarization on the outgoing particles and on their subsequent decays (the Σ^+ non-leptonic decay).

Finally some informations regarding the normalization channel $\Xi^0 \to \Lambda\pi^0$ will be also given.

1.1 Motivations

Going into more details with respect to what I anticipated in the introduction, the study of a particular hyperon semileptonic decay, the Ξ^0 beta decay, is important essentially for two reasons:

The first aspect is the study the unitarity of the CKM matrix; a more precise determination of the Cabibbo angle, the V_{US} element of CKM matrix, that arises from the measurement of some hyperon beta decay BRs, allows tighter constraints on the CKM unitarity and on the size of the other elements of this matrix.

One of the relations required by CKM unitarity is the following:

$$|V_{ud}|^2 + |V_{us}|^2 + |V_{ub}|^2 \simeq |V_{ud}|^2 + |V_{us}|^2 = 1$$

where the last approximation is explained by the current value estimed for V_{ub}[2][3]: $|V_{ub}|^2 \sim 10^{-5}$

Up to now V_{us} is measured from charged and neutral kaon beta decays, giving the following value[4][5]:

$$(V_{us})_{Ke3} = 0.2196 \pm 0.0026 \tag{1.2}$$

Asking for CKM unitarity we would then extract the following expected value for V_{ud}:

$$V_{ud}^U = 0.9756 \pm 0.0005 \tag{1.3}$$

where the U indicates the unitarity hypothesis.

Now V_{ud} is also precisely measured from free neutron decay and nuclear beta decays with the following averaged result[2][6][7]:

$$V_{ud} = 0.9734 \pm 0.0008$$

Between the two results there is a discrepancy of 2.7 standard deviations. In 2003 two new measurements of V_{us} from kaon beta decays have been published, the first one[8] is in agreement with the old V_{us} value from kaon decay, the second one[9] is instead in better agreement with the measured V_{ud} value. Thus the theoretical and experimental picture requires some clarifications.

The situation is slightly better for hyperon beta decays. Here, averaging the main experimental results, the measured value of the sine of the Cabibbo angle is[10][11]:

$$(V_{us})_{Hyp} = 0.2250 \pm 0.0027 \tag{1.4}$$

This value is substantially in agreement with both the set of measurements on kaon beta decays and on neutron beta decay, but the experimental and theoretical uncertainties are still large . Concerning the Ξ^0 beta decay, the existing measurement on the branching ratio comes from KTEV[14][15]:

$$BR(\Xi^0 \to \Sigma^+ e^- \bar{\nu_e} = (2.54 \pm 0.11_{stat.} \pm 0.16 syst.) \times 10^{-4} \tag{1.5}$$

and the corrisponding value for V_{us} is[11][16]:

$$(V_{us})_{\Xi^0 \to \Sigma^+ e^- \bar{\nu_e}} = 0.209 \pm 0.027 \tag{1.6}$$

The mean value appeears to be low with respect to both the other measurements and the expected values, nevertheless the error on the measurement is big and no conclusions can still be achieved on this side.

In this context new data on hyperon beta would be desiderable, in particular for what concerns Ξ^0 beta decay.

The second aspect is the study of the form factors appearing in the decay amplitudes of the decay: in particular from the measurement of form factors in hyperon beta decays we can search for SU(3) breaking effects and extract useful information on the mechanism of the possible breaking.

In the SU(3) simmetry framework, the form factors for neutron beta decay are exactly equal to the form factors for Ξ^0 beta decay. On the contrary some theories explaining SU(3) breaking, give significant differences for the form factor values between the two systems [10, 17, 18, 19, 20].

Up to now there is only one work extracting form factors for the Ξ^0 beta decay, again from KTEV[21]. That measurement gives the value of the ratio between g_1, the axial-vector form factor and f_1, the vector form factor (see next section for their definition):

$$\frac{g_1}{f_1}_{\Xi^0\to\Sigma^+e^-\bar{\nu}_e} = 1.32\ \pm^{0.21}_{0.17}\ \pm 0.05 \tag{1.7}$$

This measurement doesn't show differences with respect to the same ratio measured in neutron beta decay that I quote here for completeness[7][12][13]:

$$\frac{g_1}{f_1}_{n\to pe^-\bar{\nu}_e} = 1.2670 \pm 0.0030. \tag{1.8}$$

Indeed here more precise results are also useful.

For both these studies, looking at the statistics collected by NA48/I in the 2002 run, we expect to significantly improve the accuracy of these measurements.

1.2 Transition amplitude for $\Xi^0 \to \Sigma^+ e^- \bar{\nu}_e$

In fig. 1.1 is shown the first order Feynman diagram for the Ξ^0 semileptonic decay.

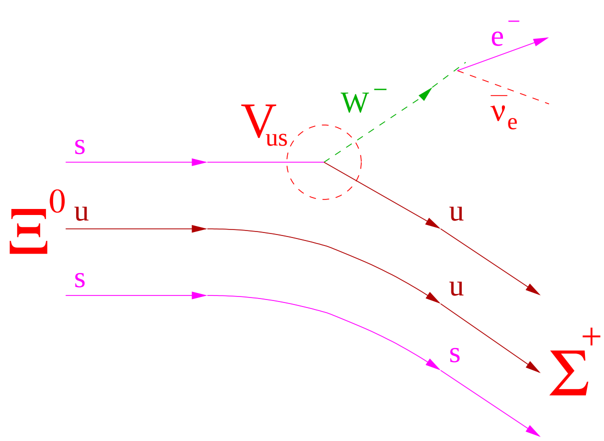

Figure 1.1: The first order Feynman diagram for Ξ^0 beta decay

In the standard electroweak theory the decay proceeds through the W^- propagator and the decay rate is proportional to the square of V_{US} , the sine of the Cabibbo angle, a parameter of the Cabibbo-Kobayashi-Maskawa matrix.

Nevertheless at the low energies involved in the center of mass of hyperon beta decay we can neglect the momentum transfer in the W^- propagator and its mass is absorbed in G_F, the Fermi's coupling constant. We will go back later to standard electroweak theory in order to introduce the radiative corrections to the transition amplitude.

By now we work in this simplified framework, where the normalized transition matrix element can be written as:

$$M = \frac{G_V}{\sqrt{2}}\sqrt{2m_{\Xi^0}2m_{\Sigma^+}2m_e}[\bar{u}_b H_\mu u_B][\bar{u}_e L^\mu u_\nu] \tag{1.9}$$

In our case $G_V = V_{us}G_F$. $\bar{u}_e$, u_ν, $\bar{u}_b$ and u_B, are Dirac spinors corresponding to the initial and final state particles, E, $\vec{p}$ and m represent respectively the energy and the momentum of the particles specified in the index. $\bar{u}_e L^\mu u_\nu$ is the matrix element of the leptonic weak current and it has the well established form with:

$$L^\mu = \gamma^\mu(1-\gamma_5) \tag{1.10}$$

$\bar{u}_b H_\mu u_B$ is the matrix element of the hadronic weak current. The calculation of this matrix element would require the treatment of strong interaction effects. In practice these effects are summarized introducing form factors in a parameterization of the most general form of H_μ compatible with its Lorentz covariance

$$H^\mu = f_1(q^2)\gamma^\mu + \frac{f_2(q^2)}{m_B}\sigma^{\mu\rho}q_\rho + \frac{f_3(q^2)}{m_B}q^\mu + g_1(q^2)\gamma^\mu\gamma_5 + \frac{g_2(q^2)}{m_B}\sigma^{\mu\rho}\gamma_5 q_\rho + \frac{g_3(q^2)}{m_B}\gamma_5 q^\mu \tag{1.11}$$

In this expression the terms f_1, f_2, f_3 come from the matrix element of the vector component of the hadronic weak current and those with a g_1, g_2, g_3 from its axial vector component. However besides the vector (axial vector) terms f_1 (g_1) the expression also includes tensor (axial tensor) terms, f_2 (g_2), and scalar (pseudoscalar) terms, f_3 (g_3) that could be induced by strong interactions.

The total decay rate comes out to be:

$$\Gamma = \frac{1}{(2\pi)^5} \int \frac{1}{E_{\Xi^0}} \frac{d^3 p_{\vec{\Sigma^+}}}{2E_{\Sigma^+}} \frac{d^3 \vec{p_e}}{2E_e} \frac{d^3 \vec{p_\nu}}{2E_\nu} \delta^4(p_{\Xi^0} - p_{\Sigma^+} - p_e - p_\nu) \frac{1}{2} \sum_{spins} |M|^2 \qquad (1.12)$$

Starting from 1.12 and summing over the final electron and neutrino spins we obtain the explicit espression of the decay rate.

In the final state we have 3 outgoing particles, corresponding to 9 kinematics variables. Applying the momentum and energy conservation laws we are left with 5 independent quantities. There are several ways to choose these 5 variables. We follow reference [22] using the lepton energy and the angles that define the directions of the lepton and of the neutrino respectively. As already discussed, we want to account for a possible polarization of the decaying hyperon.

In that case the differential decay distribution can be written as:

$$\begin{aligned} d\omega(\Xi^0 \to \Sigma^+ e^- \overline{\nu}_e) \quad = \quad & \frac{G_V^2}{(2\pi)^5} \frac{E_e|\vec{p_e}|(E^{MAX} - E_e)dE_e d\Omega_e d\Omega_\nu}{(1 - \frac{E_e}{m_{\Xi^0}} + \frac{|\vec{p_e}|}{m_{\Xi^0}} \hat{p}_e \cdot \hat{p}_\nu)^3} \times \\ \times \quad & \left\{ D_1 + \frac{|\vec{p_e}|}{E_e}(\hat{p}_e \cdot \hat{p}_\nu) D_2 + \frac{|\vec{p_e}|}{E_e}(\vec{s}_{\Xi^0} \cdot \hat{p}_e) D_3 + (\vec{s}_{\Xi^0} \cdot \hat{p}_\nu) D_4 \right\} \qquad (1.13) \end{aligned}$$

D_1, D_2, D_3 and D_4 are functions, given in appendix A, of the kinematic variables and of the form factors, $\vec{s}_{\Xi^0}$ is the polarization of decaying Ξ^0 . Finally $\hat{p} = \frac{\vec{p}}{|p|}$ are unit vectors identifying the direction of the corresponding momenta.

The form factors are functions of the squared momentum transfer $q^2 = (p_{\Xi^0} - p_{\Sigma^+})^2 = (p_e + p_\nu)^2$. For the generator I will use the limit of exact SU(3) invariance $f_1(0) = 1$ and the measured values of the other form factors for $q^2 = 0$, and then I will apply a correction to take into account the q^2 dependence of f_1 and g_1.

1.3 Radiative corrections

To first order in α_{EM}, the fine structure constant, the radiative corrections are given by 5 Feynman graphs accounting for virtual photon exchange and by 4 Feynman graphs taking into account real photon emission[22][23].

The corrections coming from virtual photon exchange can be split into two contributions, a model-dependent part and a model-independent part. The first one is translated into a re-definition of the electromagnetic form factors and it can be reduced, neglecting terms of order $\frac{\alpha_{EM}}{\pi}\frac{q}{m_{\Xi^0}}$, to:

$$\begin{aligned} f_1'(q^2=0) &= f_1^{bare}(q^2=0) + \frac{\alpha_{EM}}{\pi}c_{MD} \\ g_1'(q^2=0) &= g_1^{bare}(q^2=0) + \frac{\alpha_{EM}}{\pi}d_{MD} \end{aligned} \tag{1.14}$$

For the real photon emission the expected contribution of the model dependent part are smaller than the contributions of order $\frac{\alpha_{EM}}{\pi}\frac{q}{m_{\Xi^0}}$ already neglected for the virtual photons corrections.

At the end the model dependent corrections are summarized by the equations 1.14. They are function of the model dependent parameters c_{MD} and d_{MD}. However equation 1.14 can be interpreted as a redefiniton of the form factors. Since experiments determine the ratio of the corrected form factors, e.g. $\frac{g_1'(q^2)=0}{f_1'(q^2)=0}$ the knowledge of c_{MD} and d_{MD} is not necessary to determine the shape of the distributions, for example in our acceptance Monte-Carlo. Conversely the knowledge of c_{MD} and d_{MD} is important when absolute normalization is a concern, as in the determination of V_{us}.

The model independent part of the radiative corrections transform the differential decay distribution in the following way:

$$\begin{aligned} d\omega(\Xi^0 \to \Sigma^+ e^- \overline{\nu}_e) &= \frac{G_V^2}{(2\pi)^5}\frac{E_e|\vec{p}_e|(E^{MAX}-E_e)dE_e d\Omega_e d\Omega_\nu}{(1-\frac{E_e}{m_{\Xi^0}}+\frac{|\vec{p}_e|}{m_{\Xi^0}}\hat{p}_e\cdot\hat{p}_\nu)^3}\times \\ &\times \{D_1[1+\frac{\alpha_{EM}}{\pi}(\Phi_1+\Theta_1)] + \frac{|\vec{p}_e|}{E_e}(\hat{p}_e\cdot\hat{p}_\nu)D_2[1+\frac{\alpha_{EM}}{\pi}(\Phi_2+\Theta_2)] \\ &+ \frac{|\vec{p}_e|}{E_e}(\vec{s}_{\Xi^0}\cdot\hat{p}_e)D_3[1+\frac{\alpha_{EM}}{\pi}(\Phi_2+\Theta_2)] \\ &+ (\vec{s}_{\Xi^0}\cdot\hat{p}_\nu)D_4[1+\frac{\alpha_{EM}}{\pi}(\Phi_1+\Theta_1)]\} \end{aligned} \tag{1.15}$$

The model independent part of radiative corrections is contained in $(\Phi_1+\Theta_1)$ and in $(\Phi_2+\Theta_2)$ whose explicit form for neutral hyperon decays are:

$$(\Phi_1+\Theta_1) = 2(\frac{1}{\beta}tanh^{-1}(\beta-1))[\frac{(E_{MAX}-E_e)}{3E_e} - \frac{3}{2} + ln(\frac{2(E_{MAX}-E_e)}{m_e}]$$

$$
\begin{aligned}
&+ \quad \frac{2}{\beta}L(\frac{2\beta}{1-\beta}) + \frac{1}{2\beta}tanh^{-1}(\beta)[2(1+\beta^2) + \frac{(E_{MAX}-E_e)^2}{6E^2} - 4tanh^{-1}(\beta)] \\
&- \quad \frac{3}{8} + \frac{\pi^2}{\beta} + \frac{3}{2}ln(\frac{M_{\Xi^0}}{m_e}) \qquad (1.16)
\end{aligned}
$$

$$
\begin{aligned}
(\Phi_2+\Theta_2) \quad &= \quad 2(\frac{1}{\beta}tanh^{-1}(\beta-1))[\frac{(E_{MAX}-E_e)^2}{12\beta^2E_e^2} + \frac{2(E_{MAX}-E_e)}{12\beta^2E_e} - 3 \\
&+ \quad 2ln(\frac{2(E_{MAX}-E_e)}{m_e})] + \frac{2}{\beta}L(\frac{2\beta}{1+\beta}) - \frac{2}{\beta}tanh^{-1}(\beta)tanh^{-1}(\beta-1) \\
&- \quad \frac{3}{8} + \frac{\pi^2}{\beta} + \frac{3}{2}ln(\frac{M_{\Sigma^+}}{m_e}) \qquad (1.17)
\end{aligned}
$$

in these expressions β is the electron velocity, E_{MAX} is the electron maximum energy and L is the Spence function:

$$
L(x) = \int_0^x \frac{1-t}{t}dt \qquad (1.18)
$$

Φ_1 and Φ_2 come from virtual radiative corrections, Θ_1 and Θ_1 come from bremsstrahlung contribution.

1.4 Dependence on momentum transfer

The q^2 dependence of f_1 and g_1 is parametrized as[24]:

$$
f_1(q^2) = f_1(0) \cdot (1 - \frac{q^2}{M_V^2})^{-2} \qquad (1.19)
$$

$$
g_1(q^2) = g_1(0) \cdot (1 - \frac{q^2}{M_A^2})^{-2} \qquad (1.20)
$$

The 2 parameters M_V and M_A are extracted from neutron beta decay and again their values can be used here under the assumption of SU(3) validity[25]:

$$
M_V = 0.97GeV/c^2 \qquad\qquad M_A = 1.25GeV/c^2 \qquad (1.21)
$$

1.5 Form factor values

After the trace calculations the scalar f_3 and the pseudo-scalar form factors g_3 are always multiplied by a factor $\frac{m_l}{m_B}$; For the Ξ^0 beta decay this factor is less then $4 \cdot 10^{-4}$ and we can neglect the effect of the f_3 and g_3 form factors.

In addition defining the $G - parity$ operator:

$$G = Ce^{i\pi I_2}, \tag{1.22}$$

in which C is the charge conjugation operator and $e^{i\pi I_2}$ is a π rotation in the isospin space, the tensor (proportional to f_2) and the axial-tensor (proportional to g_2) currents have very different properties with respect to G.

We shall classify the weak currents as first-class currents if

$$\begin{aligned} GV_\mu G^{-1} &= V_\mu \\ GA_\mu G^{-1} &= -A_\mu \end{aligned}$$

and as second-class currents if

$$\begin{aligned} GV_\mu G^{-1} &= -V_\mu \\ GA_\mu G^{-1} &= A_\mu \end{aligned}$$

In the limit of exact $SU(3)$, if the weak currents are pure first class current then we need to have $g_2 = 0$ and $f_3 = 0$, if the weak currents are pure second class currents then we need to have $g_3 = 0$ and $f_2 = 0$. In the Standard Model framework and from the existing experimental results the second class currents are excluded. Then for our purpose (the BR measurement) we can put $g_2 = 0$; nevertheless it would be very interesting to release that condition and to try to measure g_2 directly from data in order to obtain experimental limit on the non-existence of second class currents.

By now we are dealing with 3 form factors. For the Ξ^0 beta decay only the ratio $\frac{g_1}{f_1}$ was measured by $KTEV$ in 1999. In order to have in our MonteCarlo generator reliable values for f_1, g_1 and f_2 we again invoke $SU(3)$ validity; in fact under this condition the effects of quark flavor differences vanish and the form factors for Ξ^0

beta decay are equal to the form factors for neutron beta decay. In the limit of exact $SU(3)$ symmetry for the fundamental barion octet, the form factors are given by (i=1,2,3):

$$\begin{aligned} f_i &= C(B,b)_F \times F_{f_i} + C(B,b)_D \times D_{f_i} \\ g_i &= C(B,b)_F \times F_{g_i} + C(B,b)_D \times D_{g_i} \end{aligned} \quad (1.23)$$

where $C(B,b)_F$ and $C(B,b)_D$ are $SU(3)$ Clebsch-Gordan coefficients. For $\Xi^0 \to \Sigma^+ e^- \bar{\nu}_e$ and $n \to p e^- \bar{\nu}_e$ both coefficients are equal to 1 and the form factors are the same for the two decays. Moreover in the neutron beta decay the ratio $\rho = \frac{g_1}{f_1}$ is experimentally measured and under the CVC (conserved-vector-current) hypothesis we can put $f_1 = 1$ and then we have $g_1 = \rho$. The Particle Data Group value for ρ is 1.2670 ± 0.0035, obtained by the weighted average of four experiment and the error includes a scale factor of 1.9 . Finally a value for f_2 is obtained using again the CVC hypothesis from the measured differences between the magnetic moment of proton and neutron:

$$f_2 = \frac{m_{\Xi^0}}{m_p} \frac{(\mu_p - \mu_n)}{2} = 2.6 \quad (1.24)$$

The value is corrected to account for the difference between the Ξ^0 and proton masses in equation 1.9.

Summarizing, under our assumptions and using the available experimental results, the best estimates for the 3 non-vanishing form factors are:

$$\begin{aligned} f_1(q^2 = 0) &= 1. \\ f_2(q^2 = 0) &= 2.6 \\ g_1(q^2 = 0) &= 1.267 \end{aligned} \quad (1.25)$$

1.6 Polarization of the out-going hyperon

The formalism described in the previous paragraphs does not account for the polarization of the outgoing Σ^+ , which determines the angular distribution of its decay products. For completeness I also give here the expression for this polarization, derived from the full expression of the differential decay rate as a function of both the polarization of the decaying hyperon and of the emitted one given by [26]. From that work, using the density matrix formalism, one can find the equation that connects P_b^μ, the polarization of the Σ^+ , with P_B^λ, the polarization of the Ξ^0 :

$$P_b^\mu = \frac{\mathcal{K}_\rho^{(\mathrm{b})} + \mathcal{K}_{\rho\lambda}^{(\mathrm{B,b})}\mathrm{P}_\mathrm{B}^\lambda}{\mathcal{K}_{00} - \mathcal{K}_\lambda^{(\mathrm{B})}\mathrm{P}_\mathrm{B}^\lambda} g^{\mu\rho} \tag{1.26}$$

$\mathcal{K}_\rho^{(\mathrm{b})}$, $\mathcal{K}_{\rho\lambda}^{(\mathrm{B,b})}$, $\mathcal{K}_{00} - \mathcal{K}_\lambda^{(\mathrm{B})}$ and $\mathcal{K}_\lambda^{(\mathrm{B})}$ are functions of the kinematic variables and of the form factor which can be extracted from reference [26]. Here we have used the polarization four vectors P^μ; for a generic particle it obeys the following conditions:

$$(P_\mu p^\mu) = 0, \qquad (P_\mu P^\mu) = -1$$

and it reduces to purely spatial unit vectors in the rest system of the corresponding particle, giving the spin direction.

The explicit form for the K parameters which I derived from 1.26 is given in appendix B and they are used in the MC simulation and listed for future reference.

1.7 The decay $\Sigma^+ \to p\pi^0$

Once we know the Σ^+ polarization, the kinematics of the two body decay $\Sigma^+ \to p\pi^0$ is fully described by the distribution of θ, the angle between the Σ^+ direction and the proton direction in the Σ^+ rest frame, in the following way[30]:

$$I(cos(\theta)) = \frac{N(cos(\theta))}{N_{TOT}} = A(1 + \alpha_{\Sigma^+}|P_{\Sigma^+}|cos\theta) \tag{1.27}$$

where A is a normalization constant, α_{Σ^+} is a decay parameter and P_{Σ^+} is the Σ^+ polarization.

In the MonteCarlo I will use the measured value for the α_{Σ^+} parameter listed on table 1.1.

1.8 The normalization channel $\Xi^0 \to \Lambda\pi^0$

To well describe this decay we need to go in more details on the treatment of hyperon non-leptonic decays introduced in the previous section.

In the V-A framework the decay amplitude can be written in the following form:

$$M = G_F m_{\pi^0}^2 \bar{u}_\Lambda (A - B\gamma_5) u_{\Xi^0} \tag{1.28}$$

where A and B are constant. Then the transition rate evaluated in the Ξ^0 rest frame is proportional to:

$$\begin{aligned} R &= 1 + \gamma_{\Xi^0} \hat{s}_\Lambda \cdot \hat{s}_{\Xi^0} + (1 - \gamma_{\Xi^0})(\hat{s}_\Lambda \cdot \hat{n})(\hat{s}_{\Xi^0} \cdot \hat{n}) \\ &+ \alpha_{\Xi^0}(\hat{s}_\Lambda \cdot \hat{n} + \hat{s}_{\Xi^0} \cdot \hat{n}) + \beta_{\Xi^0} \hat{n} \cdot (\hat{s}_\Lambda \times \hat{s}_{\Xi^0}) \end{aligned} \tag{1.29}$$

where $\hat{n}$ is a unit vector in the direction of Λ momentum, $\hat{s}_{\Xi^0}$ and $\hat{s}_\Lambda$ unit vectors in the direction of Ξ^0 and Λ spins respectively and α_{Ξ^0}, β_{Ξ^0}, γ_{Ξ^0} are decay parameters related to A and B.

These three parameters satisfy the following relation:

$$\alpha^2 + \beta^2 + \gamma^2 = 1 \tag{1.30}$$

It is also useful to introduce the parameter ϕ related to the previous ones in the following way:

$$\beta = \sqrt{1 - \alpha^2} sin\phi \tag{1.31}$$

ϕ and α are most closely related to experimental measurements and are essentially uncorrelated. α is analogous to the α_{Σ^+} parameter introduced for the Σ^+ decay and β is expected to be equal to 0 under the validity of time reversal invariance and in the absence of final state interactions.

In the two body decay α_{Ξ^0}, β_{Ξ^0} and γ_{Ξ^0} are needed if we are in presence of a starting Ξ^0 polarization. In that case we can exctract the polarization of the outgoing Λ from the following relation:

$$\vec{P_\Lambda} = \frac{(\alpha_{\Xi^0} + \vec{P}_{\Xi^0} \cdot \hat{n})\hat{n} + \beta_{\Xi^0}(\vec{P}_{\Xi^0} \times \hat{n}) + \gamma_{\Xi^0} \hat{n} \times (\vec{P}_{\Xi^0} \times \hat{n})}{1 + \alpha_{\Xi^0} \vec{P}_{\Xi^0} \cdot \hat{n}} \tag{1.32}$$

It can easily be seen that in absence of Ξ^0 polarization the polarization of the Λ along its direction is equal to α_{Ξ^0}. In our MonteCarlo, after the extraction of the Λ polarization we proceed with the decay $\Lambda \to p\pi^-$ working with the equation 1.27 already introduced for the Σ^+ decay.

In table 1.1 I list the measured values of the decay parameters α and ϕ for the three hyperon non-leptonic decays involved in this analysis. From equation 1.31 the value of β, using the measured value of α and ϕ, is always compatible with 0. I also list the value of γ that can be exctracted from 1.30 knowing α and β.

decay	α	ϕ (degrees)	γ
$\Sigma^+ \to p\pi^0$	-0.980$^{+0.017}_{-0.015}$	36±34	0.16
$\Xi^0 \to \Lambda\pi^0$	-0.411±0.022	21±12	0.85
$\Lambda \to p\pi^-$	0.642±0.013	-6.5±3.5	076

Table 1.1: decay parameters

1.9 V_{us} extraction

From relation 1.13 is clear that the square of V_{US}, the sine of Cabibbo angle, can be related to the differential decay rate which is proportional to it. From the measurement of the branching ratio of the Ξ^0 beta decay, the decay rate Γ can be extracted, using the Ξ^0 lifetime, from the relation:

$$\Gamma = \frac{BR_{\Xi^0 \to \Sigma^+ e^- \bar{\nu_e}}}{\tau_{\Xi^0}} \tag{1.33}$$

The decay rate can be obtained from the integration of 1.13; neglecting the terms multiplied by the electron mass and considering the form factors as costant (no q^2 dependence), we have[22]:

$$\begin{aligned}\Gamma &= G_F^2 V_{US}^2 \frac{\Delta m^5}{60\pi^3}\Big[(1-\frac{3}{2}\beta+\frac{6}{7}\beta^2)|f_1^2|+(3-\frac{9}{2}\beta+\frac{12}{7}\beta^2)|g_1^2| \\ &+ (\frac{12}{7}\beta^2)|g_2^2|+(\frac{6}{7}\beta^2)\Re(f_1 f_2^*)+(-4\beta+6\beta^2)\Re(g_1 g_2^*)\Big]\end{aligned} \tag{1.34}$$

where

$$\begin{aligned}\Delta m &= m_{\Xi^0} - m_{\Sigma^+} = 0.12546 \pm 0.00021 \quad GeV/c^2 \\ \beta &= \frac{\Delta m}{m_{\Xi^0}} = 0.09542 \pm 0.00011.\end{aligned} \tag{1.35}$$

For Ξ^0 beta decay $\beta^2 = 0.009$ and we can indeed neglect the terms of $O(\beta^2)$ obtaining the simpler formula:

$$\Gamma = G_F^2 V_{US}^2 \frac{\Delta m^5}{60\pi^3} \left[(1 - \frac{3}{2}\beta)(|f_1^2| + 3|g_1^2|) \right] \tag{1.36}$$

where the hypothesis of non-existence of second class currents ($g_2 = 0$) is also used.

If we want also to include the radiative correction and the q^2 dependence of form factors we obtain the following relation[22][31][32]:

$$\Gamma = (1 + \frac{\alpha}{\pi}\frac{\Psi_1}{b}) G_F^2 V_{US}^2 \frac{\Delta m^5}{60\pi^3} \left[(1 - \frac{3}{2}\beta)(|(f_1')^2| + 3|(g_1')^2|) \right] \tag{1.37}$$

where for the Ξ^0 beta decay:

$$\Psi_1 = \int_{m_e}^{E_{MAX}} dE_e E_e p_e (E_{MAX} - E)^2 (\Phi_1 + \Theta_1) \tag{1.38}$$

$$b = \int_{m_e}^{E_{MAX}} dE_e E_e p_e (E_{MAX} - E)^2 = \tag{1.39}$$

(Φ_1 and Θ_1 are the functions defined in section 1.3) and from the numerical integration finally we have:

$$\frac{\alpha}{\pi}\frac{\Psi_1}{b} = 0.0226 \tag{1.40}$$

Equations 1.37 also takes into account the model dependent corrections to the form factor, since f_1' and g_1' are related to the bare form factor f_1 and g_1 from equations 1.14.

Clearly for the V_{us} extration we need to determine the absolute normalization. Then in such a case we have to treat correctly the model dependent parameters c_{MD} and d_{MD} appearing in equations 1.14.

For our determination of V_{us} I will use the “reasonable” values given by [23] [22]:

$$\frac{\alpha}{\pi} c_{MD} = \frac{\alpha}{\pi} d_{MD} \simeq 0.0105 \tag{1.41}$$

In those works the values of c_{MD} and d_{MD} are dominated by contributions coming from the standard electroweak theory.

Chapter 2

The NA48/I detector

The NA48 apparatus was built to measure the double ratio of $K^0 \to 2\pi$ decay rates:

$$R = \frac{\Gamma(K_S^0 \to \pi^+\pi^-)}{\Gamma(K_L^0 \to \pi^+\pi^-)} \frac{\Gamma(K_L^0 \to \pi^0\pi^0)}{\Gamma(K_S^0 \to \pi^0\pi^0)} \simeq 1 - 6\Re(\epsilon'/\epsilon) \tag{2.1}$$

A schematic view of the complete detector is shown in fig. 2.1. A magnetic spectrometer was used to measure the K decays into two charged pions and a muon detector to reject Kμ3 background. For the reconstruction of the decay into two neutral pions a quasi homogeneous liquid krypton calorimeter (LKr) was built. This detector has a good energy and time resolution for photons. The LKr is followed along the beam line by a hadronic calorimeter mainly used for triggering, but also to provide additional information for particle identification. A scintillator hodoscope placed between the fourth drift chamber and the LKr provided the time resolution for charged decays needed for the tagging technique. This technique allowed to separate K_L and K_S decay by a coincidence with a detector[37] placed on the proton beam feeding the K_S target.

For a detailed explanation of the measurement technique and of the results obtained with data collected between 1996 and 2001 I refer you to several papers[1][33].

Most of the detectors used in the NA48/I run in 2002 are the same used for the ϵ'/ϵ measurement. The main differences concern the beam, the removal of the tagger detector and of the AKS[38], a veto detector placed on the K_S beam to delimit the fiducial region for K_S decays. A new read-out for the drift chambers was also used in 2002.

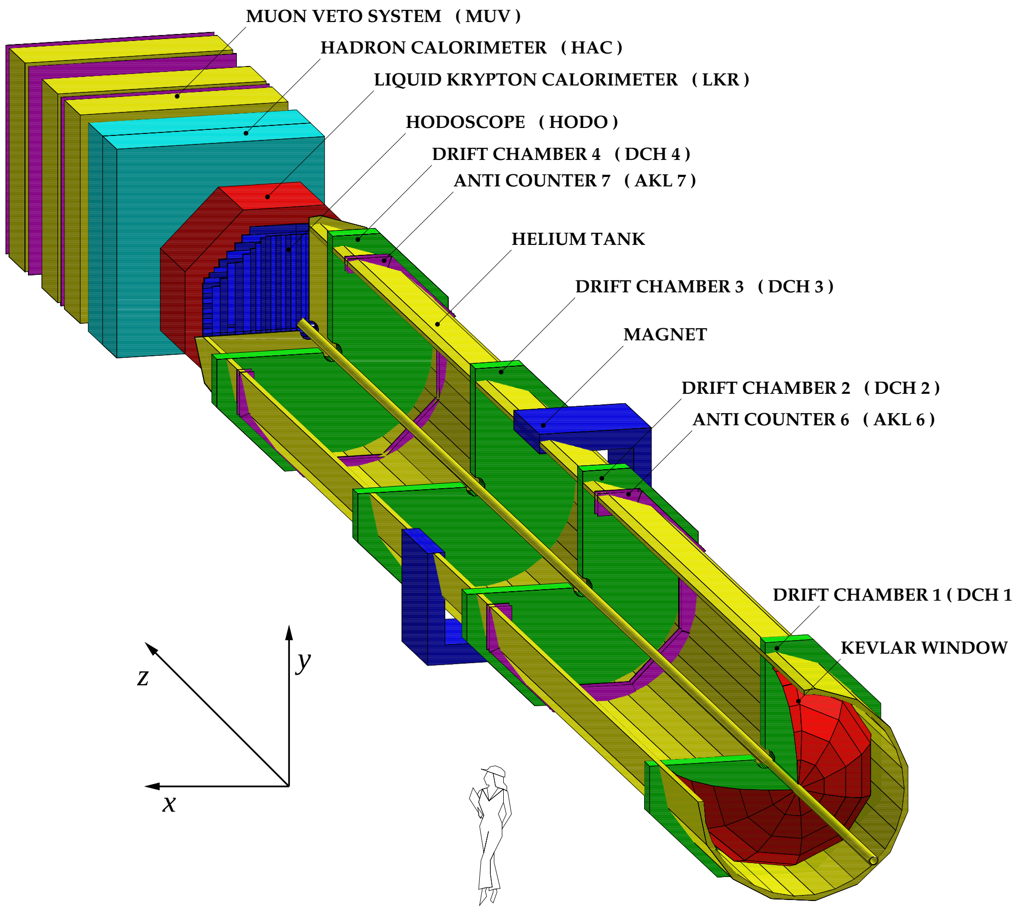

Figure 2.1: The NA48 detector. The orientation of the axes in the laboratory rest frame is also shown.

Now we define the NA48 orthogonal rest frame: the z axis follows the axis of the old K_L^0 beam (it is also the symmetry axis of the detector) the 0 is defined at the position of K_S^0 target and it points from the target to the detector. The x and y orientation are horizontal and vertical respectively. The y axis points up and the 0 is defined at the intersection point with the K_L^0 beam. The x axis orientation is fixed to have a right-handed rest frame and the 0 is defined at the K_S^0 target.

In the rest of the chapter 4 I will describe in detail the detector configuration as it was in the 2002 run and for each sub-detector I will illustrate the geometry and the relevant performances.

I start with the beam description and with the definition of the fiducial decay region.

2.1 The beam and the fiducial decay region

NA48/I was performed at the CERN SPS accelerator and used a 400 GeV/c proton beam impinging on a Beryllium target to produce a neutral beam.

In the SPS protons were accelerated up to 400 GeV/c with the 200 MHz RF systems. Then the RF is switched off and the beam is extracted using the slow resonant extraction[34] scheme.

The secondary beams are based on the same transport line[35] used for the ϵ'/ϵ measurement but the K_L^0 beam was blocked and several changes were also applied to the K_S^0 beam line. First of all, for protons feeding the K_S^0 target magnetic bending, rather than crystal channeling[36], was used, in order to maximize the intensity. In fact in the ϵ'/ϵ runs the intensity of K_S^0 beam was $\sim 3 \cdot 10^7$ protons per burst, in the 2002 run this intensity was increased up to $\sim 3 \cdot 10^{10}$ protons per burst.

The duty cycle was also changed and in 2002 the spill length was 4.8 s out of 16.2 s cycle time (very similar to the duty cycle of the last ϵ'/ϵ run in 2001).

Fig. 2.2 shows the K_S^0 station and the final collimator for the 2002 run. To reduce the number of photons in the neutral beam, primarily from π^0 decays, a platinum absorber 24 mm thick was placed in the beam between the target and the sweeping magnet. To allow the introduction of the absorber the K_S^0 target was displaced upstream by 0.234 m with respect to the previous ϵ'/ϵ runs.

A 5.1 m thick collimator (see again fig. 2.2) selected a beam of neutral long lived particles (K_S^0 , K_L^0 , Λ, n, Ξ^0 and γ) at an angle of 4.2 $mrad$ with respect to the proton beam direction. The angle of 4.2 $mrad$ was chosen to reduce the flux of neutrons reaching the fiducial decay region and then the detector region.

The defining aperture was at 5.03 m downstream from the K_S^0 target and it had a radius of 3.6 mm The collimator is such that the beam converges (with an angle

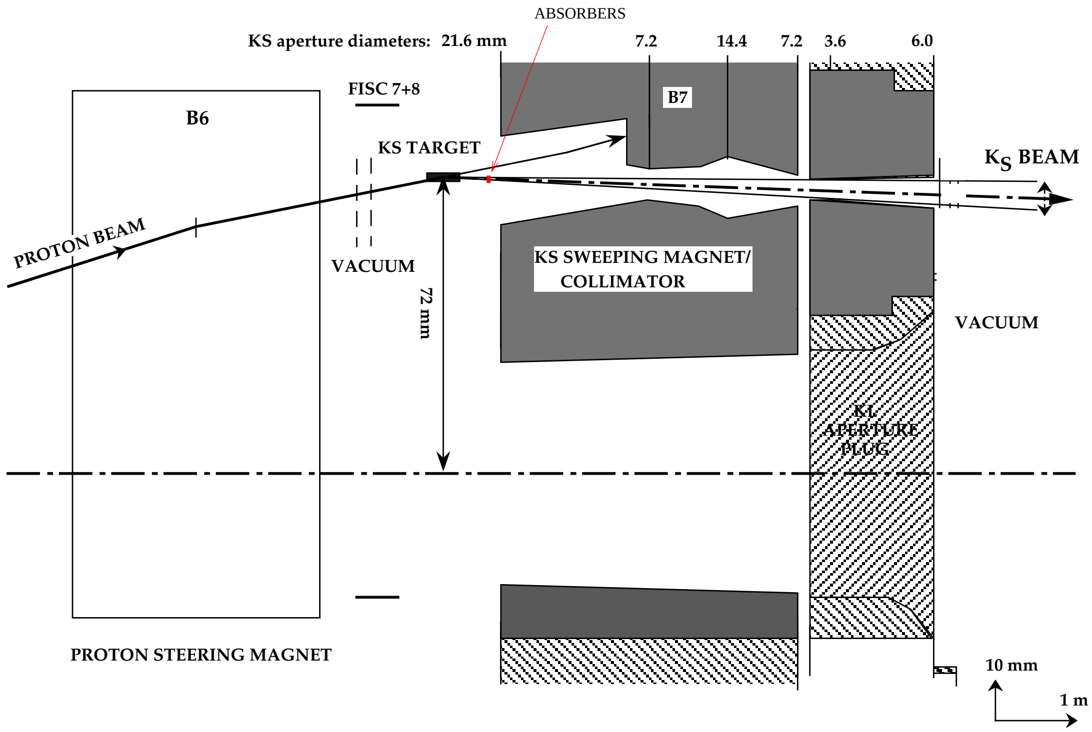

Figure 2.2: Schematic view of K_S^0 station, including the K_S^0 target and the collimator, for the 2002 run.

of 0.6 $mrad$) to the center of the detector, ~ 120 m downstream.

In table 2.1 I summarize the characteristics of 2002 beam.

SPS proton momentum	400 GeV/c
Duty Cycle	4.8 s/16.2 s
Protons per pulse on target	$5 \cdot 10^{10}$
Production angle	-4.2 $mrad$

Table 2.1: Beam characteristics for 2002 run.

After the collimator, 6.2 m downstream the K_S^0 target, the fiducial decay region begins (see figure 2.3). Here the K_S^0 beam divergence is ± 0.375 $mrad$.

The decay region is contained in an evacuated (pressure $< 10^{-7}$bar) tank 89 m in length, with a 0.003 radiation lengths thick polymide (Kevlar) window at the end (see "vacuum tank" in fig. 2.3).

The neutral beam continues in a $\sim$ 150 mm diameter tube going through the detector elements to the beam dump. The tube, later referred to as beam pipe, is evacuated to avoid particle interactions, mainly from photons and neutrons, inducing accidental activity in the detector.

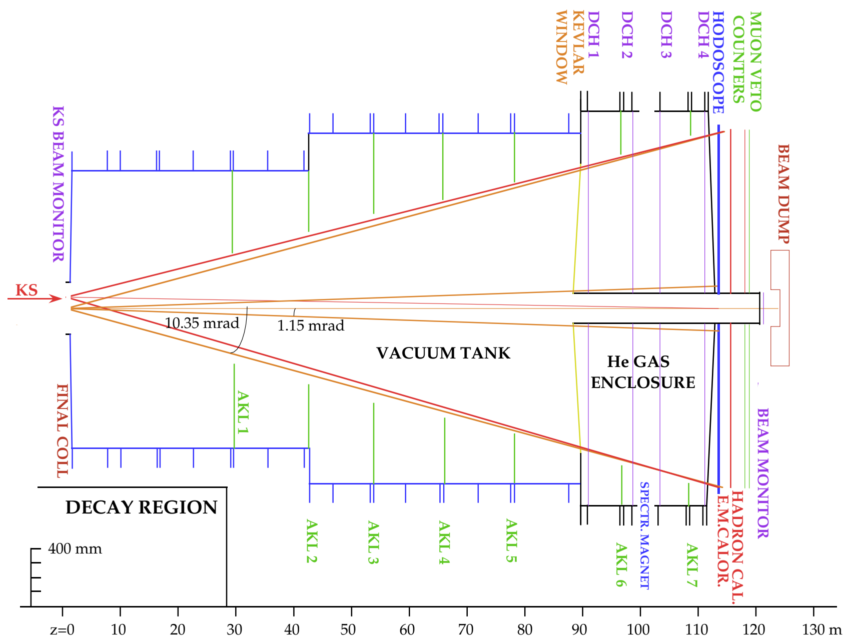

Figure 2.3: Schematic view of the decay regions upstream the detector, in green are shown the AKL's rings.

2.2 The AKL

The K_L^0 anti-counter(AKL) system[39] consists in seven "rings" of iron and scintillator, which enclose the decay volume, as shown in figure 2.3. 5 rings are located in the vacuum tank containing the decay region and two rings are instead located in the helium tank containing the drift chambers.

The detector covers an angular region starting at $\sim 10\ mrad$ with respect to the beam axis, which is complementary to the central detector one. A ring is made of two pockets. A pocket consists in a 3.5 cm thick iron layer, acting as photon converter, followed by a scintillator counter which is read-out on both sides. A total of 144 counters are present. The efficiency for photon detection is $\sim 95\ \%$.

The AKL was originally built to veto the decay of K_L^0 into 3 neutral pions, with one or more γs outside the detector acceptance, in the ϵ'/ϵ measurement.

2.3 The magnetic spectrometer

To detect the charged particles coming from the decay fiducial region and to measure their momentum NA48 has a conventional magnetic spectrometer. Moving along the beam axis the magnetic spectrometer is made by two drift chambers(DCH) to measure the initial direction of the charged particles, by the magnet to deflect them and then again by two drift chambers to measure the final direction. The first drift chamber is located immediately after the Kevlar window. The momentum and the charge of the particle are extracted from the angle between the initial and final direction of the track. From the final direction it is also possible to reconstruct the impact points of the tracks in the following detectors.

The magnet[41] gap is 2.45 wide m and 2.2 m high and its bending power is $\int \vec{B} \cdot \vec{dl} = 0.83\ T \cdot m$. Inside the magnet the field is uniform within 5 % of its nominal value. In fig. 2.4 it is shown a schematic drawing of spectrometer.

The DCHs[40] are located inside a cylinder filled with Helium at atmospheric pressure. The helium isolates the chambers from the low pressure of the vacuum tube without increasing too much the interaction probability and the multiple scattering probability of particles coming from the decay region. The DCHs borders are octagonal, their width is 2.9 m and they are filled with a gas mixture containing the same amount of argon and ethane, and less than 1 % of water. Each chamber corresponds to $4 \cdot 10^{-3}$ radiation lengths of material. The overall Helium corresponds to $4 \cdot 10^{-3}$ radiation lengths too. A chamber is constituted by 4 views and each view

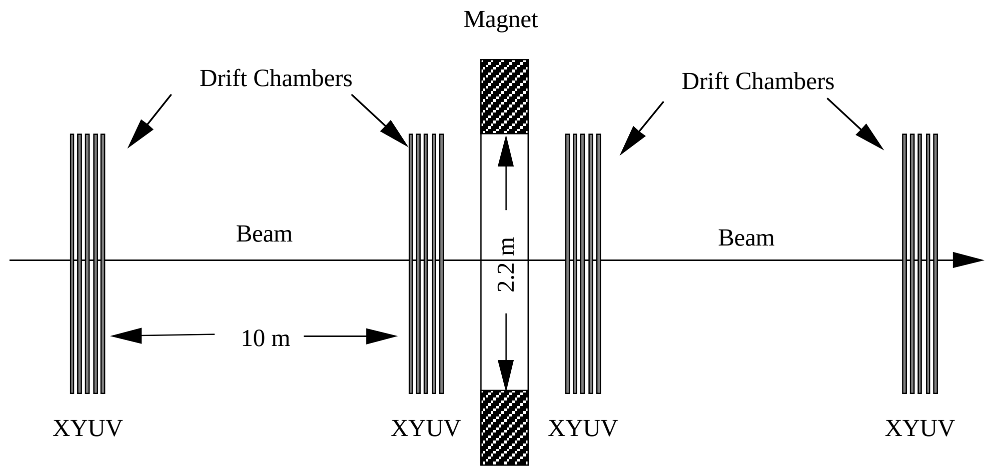

Figure 2.4: Schematic of NA48 spectrometer with the 4 DCHs and the magnet.

contains two planes of electrode wires. The views are separated from each other and from the Helium by foils of graphite coated mylar.

In fig. 2.5 are showed the wire orientation of the 4 views. The first view has wires along the x coordinate, the second one along y and the third and fourth with an angle of 45 and - 45 degrees with respect to the x direction. These two views are called U and V view respectively. The orientation of the U and V view allows to remove ambiguities in the reconstruction of 2 or more tracks. Each plane is made of 256 anode wires stepped by 10 mm ($\pm 10 \mu m$). Each wire of one plane is positioned in the central position with respect to two wires of the other plane of the same view (see fig. 2.6). That disposition allows to remove the right-left ambiguity and improves space and time resolution.

The distance between the two planes of the same view is 12 mm and each plane is placed between two planes of cathodic wires held at high voltage in working conditions. The anodic wires are grounded through the preamplifiers. The diameter of the anode wires is 20 μm and the diameter of cathode wires is 120 μm.

The electric field is generated by the cathodic wires and the mylar-graphite planes; their voltage in 2002 was -2200 V and -1405 V respectively.

After the preamplifier the signals goes to TDC cards to measure the drift times. These times are stored into a "ring buffer" where they are accessible to the trigger (see section 3.3) and to the DCH read-out. Fast multiplicity conditions are also formed in this system to be used in the level 1 trigger.

In 2002 the DCHs were equipped with a new read-out system. In fact the old read-out could collect no more than 7 hits for each DCH plane. In the standard ϵ'/ϵ runs the probability to have more than 8 hits was around 20 % and was even bigger in 2002. The new read-out system avoids this problem and it allows to collect 63 hits per plane (this limit comes from the DAQ system).

2.3.1 Performances

The space resolution in a single view is 120 μm. For the momentum resolution we have two contributions:

$$\frac{\delta P}{P}(\%) = 0.42 \oplus 0.010P(GeV/c), \tag{2.2}$$

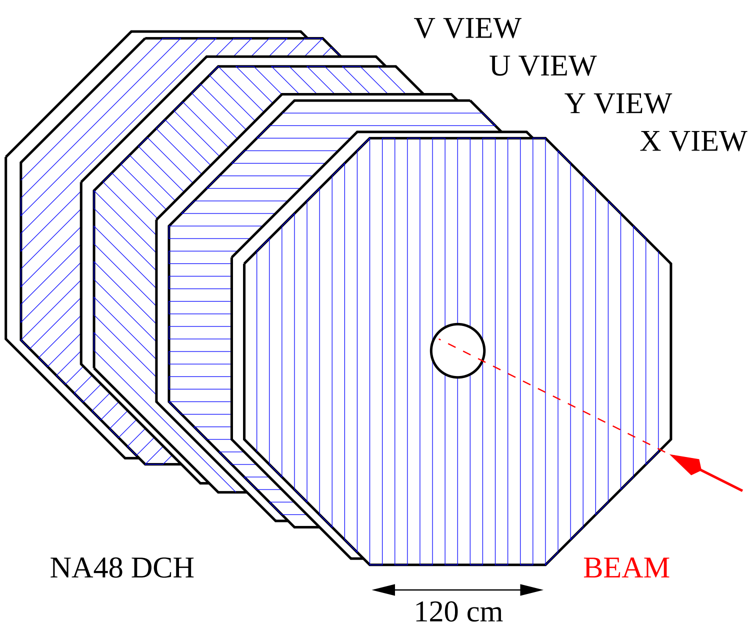

Figure 2.5: Schematic of wires orientation for the 4 DCHs views

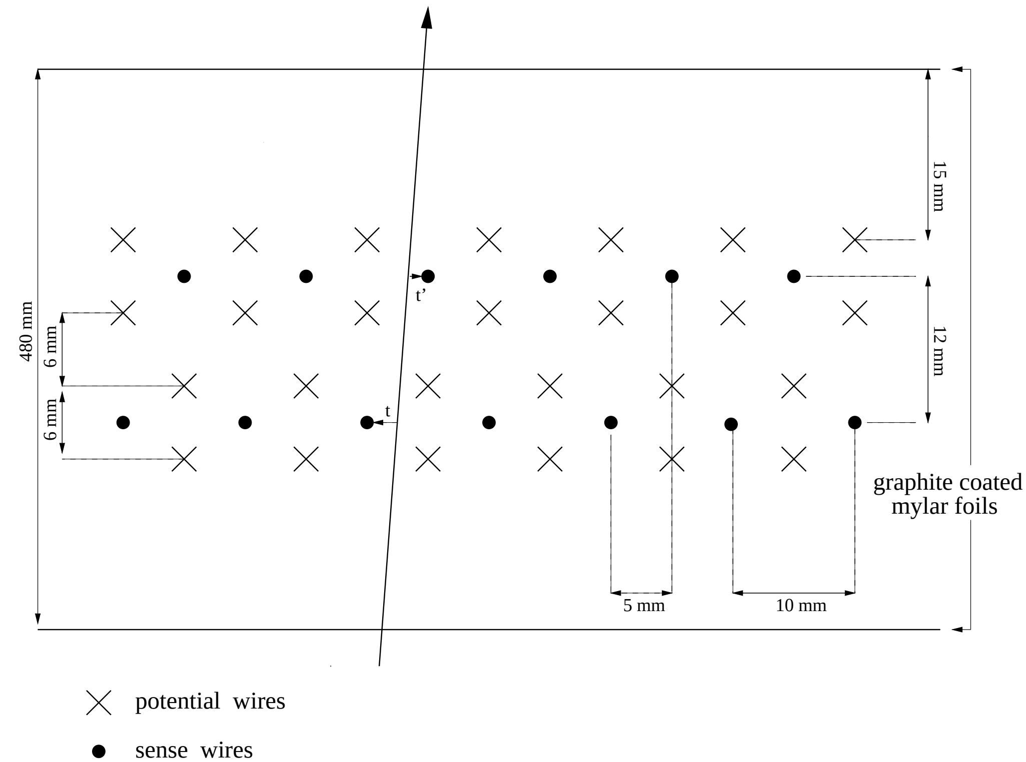

Figure 2.6: Disposition of potential and sense wires in two planes of the same view for the NA48 DCHs.

where the first term comes from multiple scattering and the second one from the space resolution on the hit positions. The mass resolution is 2.5 MeV/c^2 for the kaon decays $K \rightarrow \pi^+\pi^-$ (ϵ'/ϵ analysis) and 1.0 MeV/c^2 (see fig. 2.7) for the decay $\Lambda \rightarrow p\pi^-$ (secondary vertex of our normalization channel $\Xi^0 \rightarrow \Lambda\pi^0$).

2.4 The “charged” hodoscope

In the ϵ'/ϵ measurement the “charged” hodoscope[45] ($CHOD$) was used to provide a fast topological trigger for the charged events, and to measure their time, both at trigger level and off-line.

In 2002 run the charged hodoscope still gave the time of charged events at trigger level and I will also use the off-line information in my selections. Instead for the

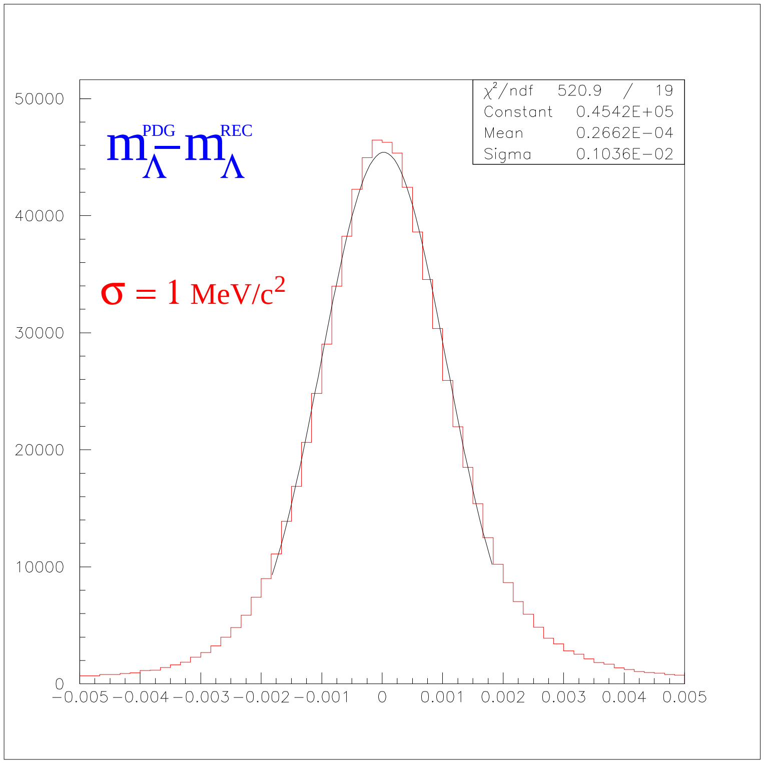

Figure 2.7: Difference between the reconstructed proton-pion invariant mass from the data and the PDG value of Λ mass. The distribution is centered at 0 and the resolution is $\sim 1.0\ MeV/c^2$

hyperon decays the topological trigger has been replaced by a simpler request for at least a time and space coincidence between the two planes of this detector.

In fact the hodoscope (see figure 2.8) consists of a first plane of 64 vertical scintillators, followed by a second plane of 64 horizontal scintillators.

The counters are made of NE110 plastic scintillator, with a high light output. The scintillation light is collected from one edge of the counter through a Plexiglas light guide, with a fish-tail shape, and detected by a XP2262B Philips photomultiplier.

The distance between the two planes (75 cm), and the position of the second plane with respect to the entrance wall of the LKr (80 cm downstream), are chosen to reduce the effects of back-scattering from the calorimeter.

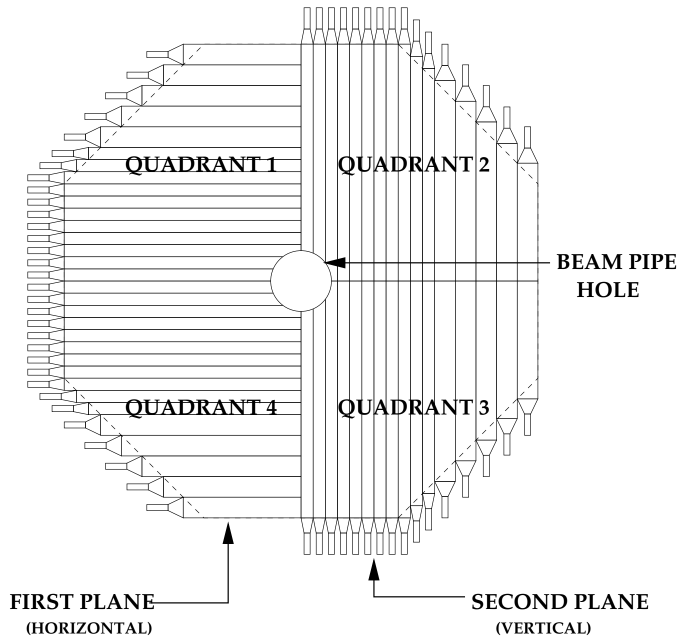

Figure 2.8: Layout of the charged hodoscope.

The counter thickness is 2 *cm*, corresponding to $\sim 0.05\ X_0$. The widths are either 6.5 *cm*, in the region near to the beam pipe, or 9.9 *cm* far from it. The lengths vary from 121 *cm* to 60 *cm* going from the beam pipe to the external region.

Each analog pulse coming from the photo-multiplier is connected to a high impedance input of the FADC (Fast Analog to Digital Converter) and then fed to a discriminator. The discriminators, working in “burst guard” operation mode with a threshold of 60 mV, are used to produce the input signals for both the FTDC (Fast Time to Digital Converter) and the fast logic electronics. The fast logic electronics produces topological triggers and multiplicity triggers used in our Level 1 (see section 3.2).

The read-out electronics is hosted in modules called PMB [46] (Pipeline Memory Board), whose functionalities are schematically illustrated in fig. 2.9. In this module the analog signal is shaped, digitized, sampled every 25 ns (40 MHz) and read out by 10 bits FADC card. At the same time the discriminated signal triggers a fast linear voltage ramp between two fixed levels which is sampled every 25 ns. This

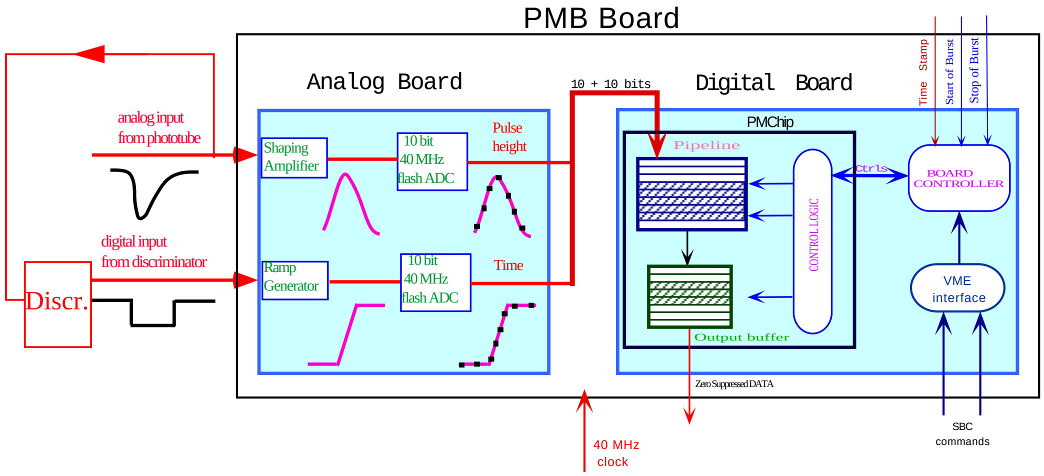

Figure 2.9: Illustration of the *PMB* boards. The PMB modules have been specifically designed for the charged hodoscope system, but are also used for the read-out of the *AKL* and *NHOD* detectors, and of the neutral trigger systems.

circuit acts as a FTDC, because by fitting the ramp it is possible to reconstruct the time of the hit with a good resolution.

In fact after off-line corrections the time resolution on the single track is better than 250 *ps* (see fig 2.10). The main off-line corrections applied are the following:

- The discriminators producing the trigger for FTDCs are threshold discriminators and the starting time of the ramp depends from the signal amplitude. We can correct for this effect using the signal amplitude measured by the FADC (the correction is calibrated with the data).

- Depending on the impact point of the tracks in the scintillators, the path of the light to the photo-multiplier varies from few centimeters to more than 1 meter. In order to take this effect in the time measurement into account, a correction is applied using the impact point of the particle in the hodoscope that can be reconstructed from the spectrometer's data.

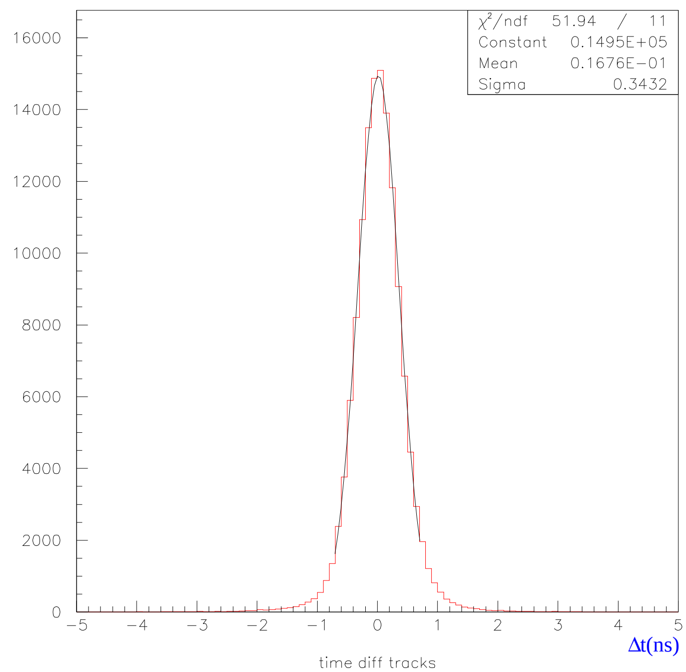

Figure 2.10: $CHOD$ time resolution: this plot shows the distribution of the time difference between the two tracks coming from the decay $\Lambda \to p\pi^-$ (The Λ comes from the decay $\Xi^0 \to \Lambda\pi^0$).

2.5 The electromagnetic calorimeter

The electromagnetic calorimeter [42, 43] (LKr) of NA48 is a liquid Krypton quasi homogeneous calorimeter and it is located 80 cm downstream from the $CHOD$.

The liquid Krypton is used both as absorber and active medium. The ionization, produced by an electromagnetic shower in the calorimeter, is very well correlated to the energy of the incoming photon or electron.

The calorimeter volume (9 m^3) is divided into 13248 towers, also called cells, each defined by three Cu–Be–Co 40 μm thick ribbon electrodes, as shown in figures 2.11 and 2.12. The cells are $\sim 2 \times 2cm^2$ in cross section, and 127 cm long in the longitudinal direction (equivalent to $27X_0$ and $2\lambda_{int}$ lengths).

The ribbon in the middle of the cells acts as a collecting anode. The outer strips

Properties of liquid Kripton

Atomic number	36
Mass number	84
Density	2.4 g/cm^3
Interaction length	60 cm
Radiation length	4.7 cm
Molière radius	6.1 cm
Boiling point at 1 bar	119.8° K
Radioactivity	500 Bq/cm^3
Electron drift velocity at 1 kV/cm	0.27 cm/μs
Electron drift velocity at 5 kV/cm	0.37 cm/μs
Dielectric constant	~ 1.7

Table 2.2: Properties of liquid Krypton.

(cathodes) are connected to ground, while a voltage of 5 kV is applied to the anodes. The ionization current induced on the anode is measured by the electronic chain. Only the initial current is read out from each cell, in order to achieve a very good time resolution.

To control the transverse size of the cells, which must be fixed and known with high precision (50 μm), each of the electrodes is stretched between five accurately machined spacer plates and the front and back plates of the calorimeter. The spacer plates apply an "accordion" ("zig-zag") geometry to the electrodes which undergo a tension of $2N$. The angle applied to the electrodes by the spacer plates is 48 $mrad$. The accordion geometry minimizes the effect of the inefficient collection of ionization for showers which develop close to the electrodes, and leads to a smearing of the the non-linearity effects depending on the transverse position of the impact point.

The geometry of the tower is projective: it points towards the average K_S^0 decay position (~ 5 m after the K_S^0 collimator).

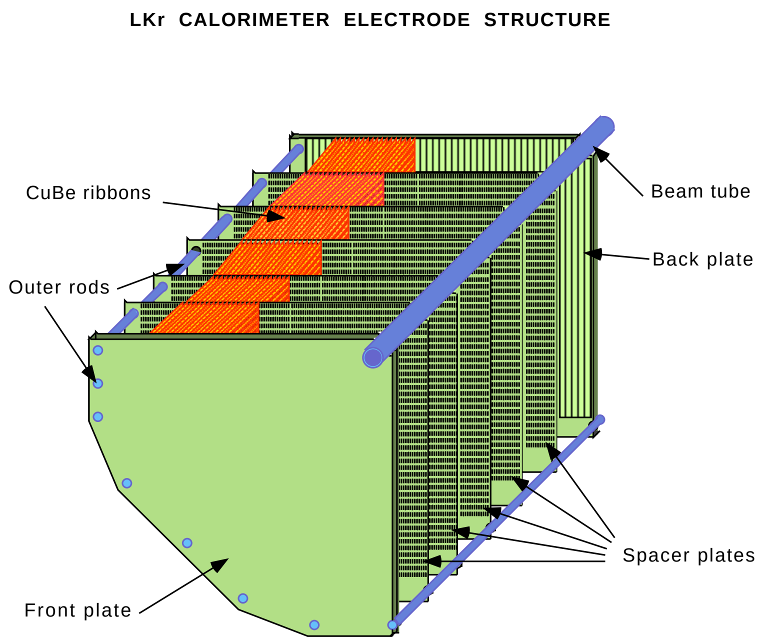

Figure 2.11: The internal structure of the calorimeter

The detector is contained in a cryostat, formed by an outer aluminum vessel and an inner steel vessel, which maintains the Krypton at a temperature of $121°K$.

The front-end "cold" electronics is directly mounted on the detector back-plate in order to minimize the noise, and to optimize the timing of signal extraction. It includes a preamplification stage and a calibration system. (see figure 2.13). Outside the cryostat, a transceiver drives the output signals to custom read-out modules, later called CPD[44] (Calorimeter Pipeline Digitizer). The analog card of the CPD signal generates a shaped pulse with a 70 ns FWHM, which is processed by means of a optimal filtering algorithm to evaluate pulse height and extract energy and time. Synchronous digital sampling is done every 25 ns by a 10 bit FADC. In order to increase the dynamic range, the signals are amplified with variable gain before digitization. The gain is set automatically by the electronics and is recorded in two additional bits.

A dedicated processor, the "data concentrator", identifies the cells with energies above a predefined threshold, and those in an extended region around them defined

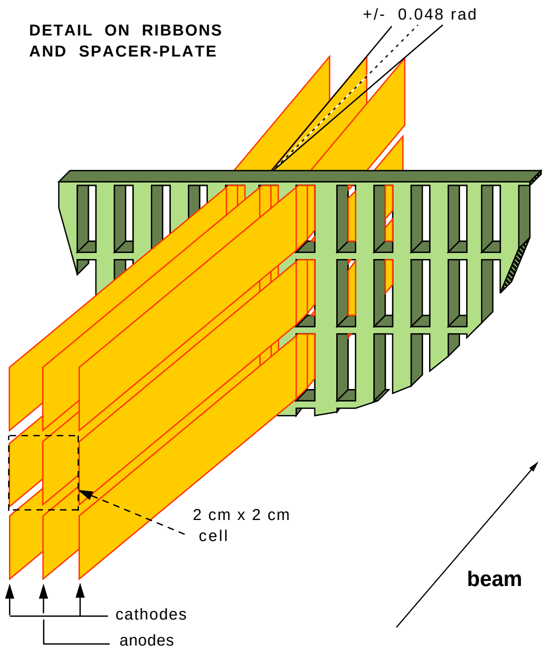

Figure 2.12: Tower's definition in the LKr. The "accordion" geometry is also shown.

by a suitable algorithm. Only digitized information from the cells of these regions are selected and read out. In 2002 run the "data concentrator" threshold was set to 72 ADC counts corresponding to $\sim$ 233 MeV. This threshold allows a fully efficient energy reconstruction for electromagnetic showers of 2 GeV.

2.5.1 Performances

After calibration factors are applied, the energy resolution is:

$$\frac{\sigma(E)}{E} = \frac{3.2\%}{\sqrt{E_{[GeV]}}} \oplus \frac{10\%}{E_{[GeV]}} \oplus 0.5\% \tag{2.3}$$

where the first term relates to the sampling fluctuations, the second to the stochastic fluctuations (electronic noise) and the third to inter-calibration errors, inhomogeneities and energy absorbing material in front of the calorimeter. Fig. 2.14 shows the LKr energy resolution as a function of energy. The energy resolution for an energy of 25 GeV is $\sim$ 1%. In the ϵ'/ϵ analysis residual non-linearities were measured at the level of 0.2% in the energy range $[5 \div 100]$ GeV.

The position resolution of photon clusters is better than 1.3 mm in the x and y direction for photon energies above 20 GeV. Combining the energy and position measurements, the longitudinal vertex position of the $\pi^0 \to \gamma\gamma$ decays determined using the π^0 mass constraint is reconstructed with a resolution of $\sigma_z = 1$ m.

The transverse geometric scale of the calorimeter is known with a maximum error of 100 μm in x direction and 150 μm in y direction.

The time resolution for the single clusters is $\sigma_t \simeq 400$ ps. (see fig. 2.15). During the 2002 run about 50 cells of the calorimeter had either faulty preamplifiers or no voltage applied to the electrodes (they are later referred to as “dead cells”). Events where the shower maximum for a photon is close to a dead cell are rejected.

2.6 The “neutral” hodoscope

The “neutral” hodoscope [47] ($NHOD$) is made of 256 bundles of scintillating fibers, each contained in an epoxy-fiberglass tube (7 mm in diameter and 2 m in length). The bundles are immersed in the liquid Krypton volume, at a position corresponding to the average maximum of the electromagnetic shower in the ϵ'/ϵ runs (average

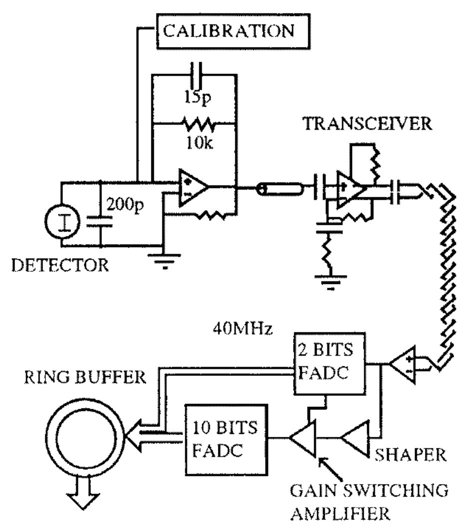

Figure 2.13: Scheme of the Kr read-out electronics

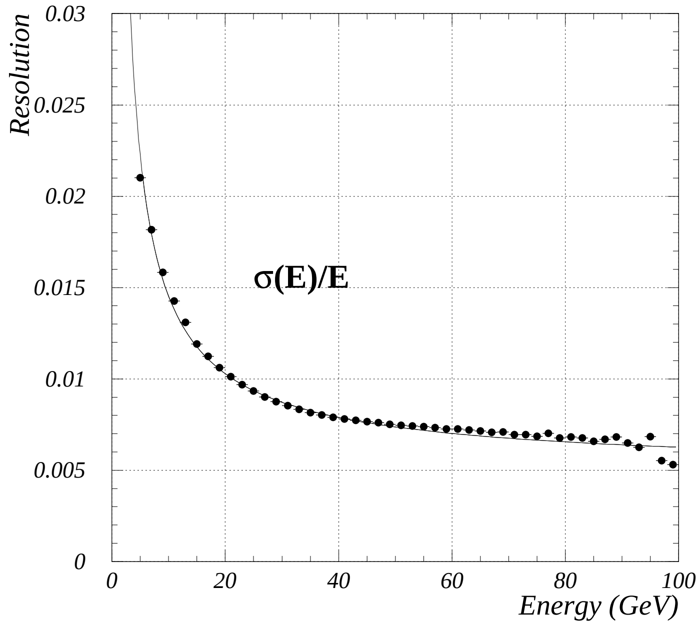

Figure 2.14: The *LKr* energy resolution as a function of energy. In the data the resolution can be evaluated looking to the clusters produced by electrons of known momentum.

photon energy $\sim 25\ GeV$. The tubes are fixed to the second spacer plate (at a depth of 9.5 radiation lengths) and extend horizontally from the center to the outer edge /see fig. 2.16. The signals are read-out by 32 photo-multipliers HAMAMATSU 6A61BA1B.

The time of electromagnetic showers is measured with a resolution better than 300 ps. This measurement could be used to cross check the time measurement by the calorimeter.

The neutral hodoscope signals are also used to form an independent "minimum bias" trigger for events with electromagnetic showers, used to measure the efficiency of the main triggers (see section 3.2).

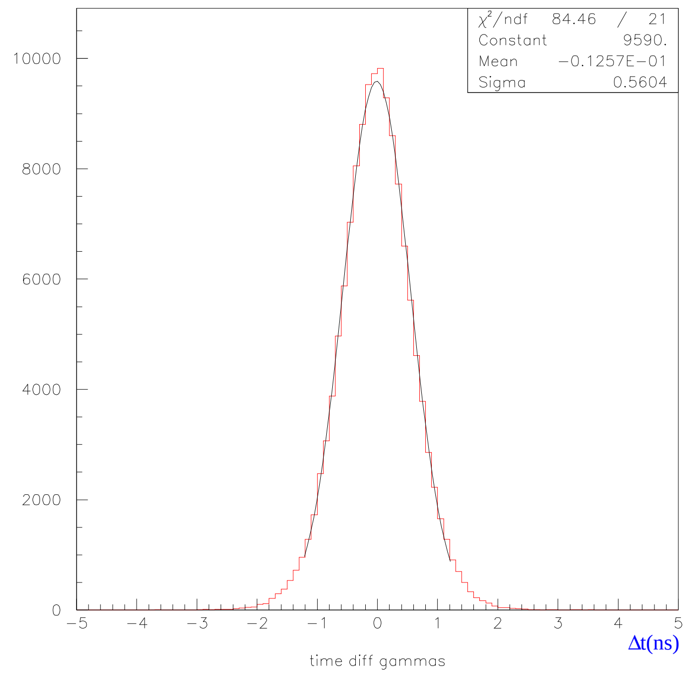

Figure 2.15: LKr time resolution: this plot shows the distribution of the time difference between the two clusters produced by the γs of the decay $\pi^0 \to \gamma\gamma$ (The π^0 comes from the decay $\Xi^0 \to \Lambda\pi^0$).

2.7 The hadronic calorimeter

A conventional iron-scintillator sandwich calorimeter (HAC), $6.7 L_{INT}$ thick, follows the LKr calorimeter, to measure the hadronic shower leakage mainly for triggering purpose. The HAC is composed by two modules ("front" and "back"), each made of 24 scintillator planes. Each plane is divided into 22 strips divided in the middle and read-out at the extremities. The strips are arranged alternatively along the vertical and horizontal direction (see fig. 2.17).

Signals from groups of planes are read out by 176 photomultipliers (44 for each module/orientation). The off-line reconstructed energy resolution is $\sigma_{E_{had}}/E_{had} \sim 65\%/\sqrt{E_{[Gev]}}$.

The digitized sum of the signals (obtained with the same electronic of the LKr

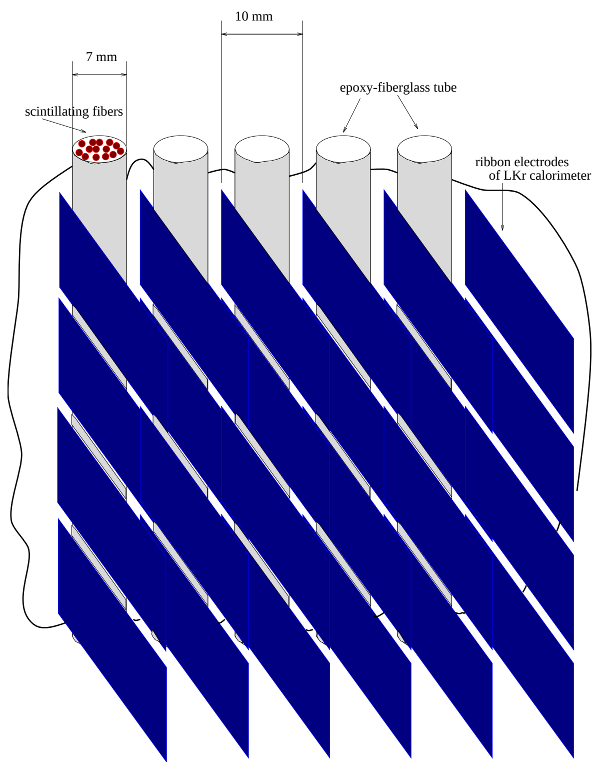

Figure 2.16: Location of the neutral hodoscope in the LKr

calorimeter) after proper shaping of the PM signals is sent to the neutral trigger to determine the hadronic contribution to the total energy ($ETOT$).

2.8 The muon counter

The muon veto (MUV) consists of three 80 cm ($\sim 5L_{INT}$) thick iron walls[1], which act as muon filters, each followed by a plane of scintillator strips. The strips are alternately vertical and horizontal, partially overlapping, and equipped with photomultipliers on both sides. The first two planes have 11 strips of scintillator. Plane three has 6 strips of scintillator in the vertical direction.

The time resolution of the muon counter was $\sim$500 ps during the 2002 run. The inefficiency for μ rejection was measured to be less than 0.3% in the ϵ'/ϵ analysis.

[1]Muon loose on average $\sim$2.5 GeV when crossing 80 cm of iron due to ionization.

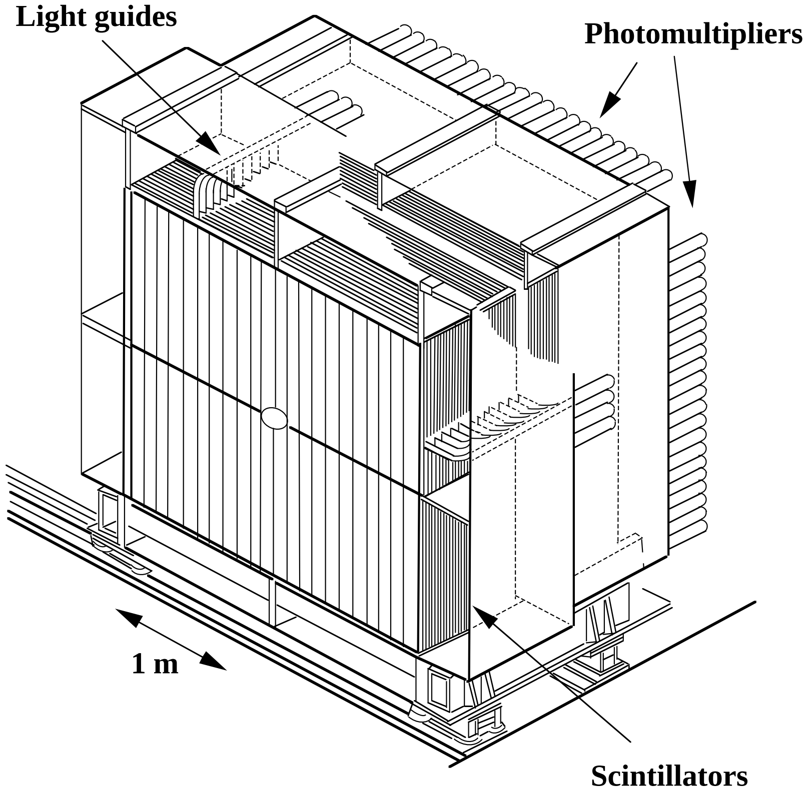

Figure 2.17: Schematic layout of hadronic calorimeter.

Chapter 3

Data collection

The NA48 trigger used to select hyperon beta decay is organized in 3 stages. The first Level, the so called "Level 1" ($LV1$ in the following), is built using fast information from hits in the AKL, in the Hodoscope and in the DCHs and from the energy measured in the LKr and in the hadron calorimeter. The second Level ($LV2$ in the following) uses the responses available on line from the so called Mass-Box, a system including 8 fast processors. The Mass-Box (MBX), using information coming from the DCHs 1, 2 and 4, is able to calculate the track's momenta, the position of charged vertices and their invariant masses. The MBX can also apply conditions on the reconstructed values and sends to the Trigger supervisor the response for those requests. The MBX is triggered by the $LV1$ output triggers. Both the LV1 and LV2 trigger's output go to the "trigger supervisor", this system correlates all the trigger information and produces the final decision to record the data. A scheme of the NA48 trigger system is shown in fig. 3.1, including also the neutral part. The neutral trigger is not used in our selection and it is described elsewhere[48].

The data of triggered events are collected from all the sub-detectors and written on disk by the NA48 acquisition system based on an array of PCs.

Finally the Level 3 trigger ($LV3$ from now on) is a software trigger and it uses all the collected information to apply off-line a complete event reconstruction and a raw selection to the reconstructed events.

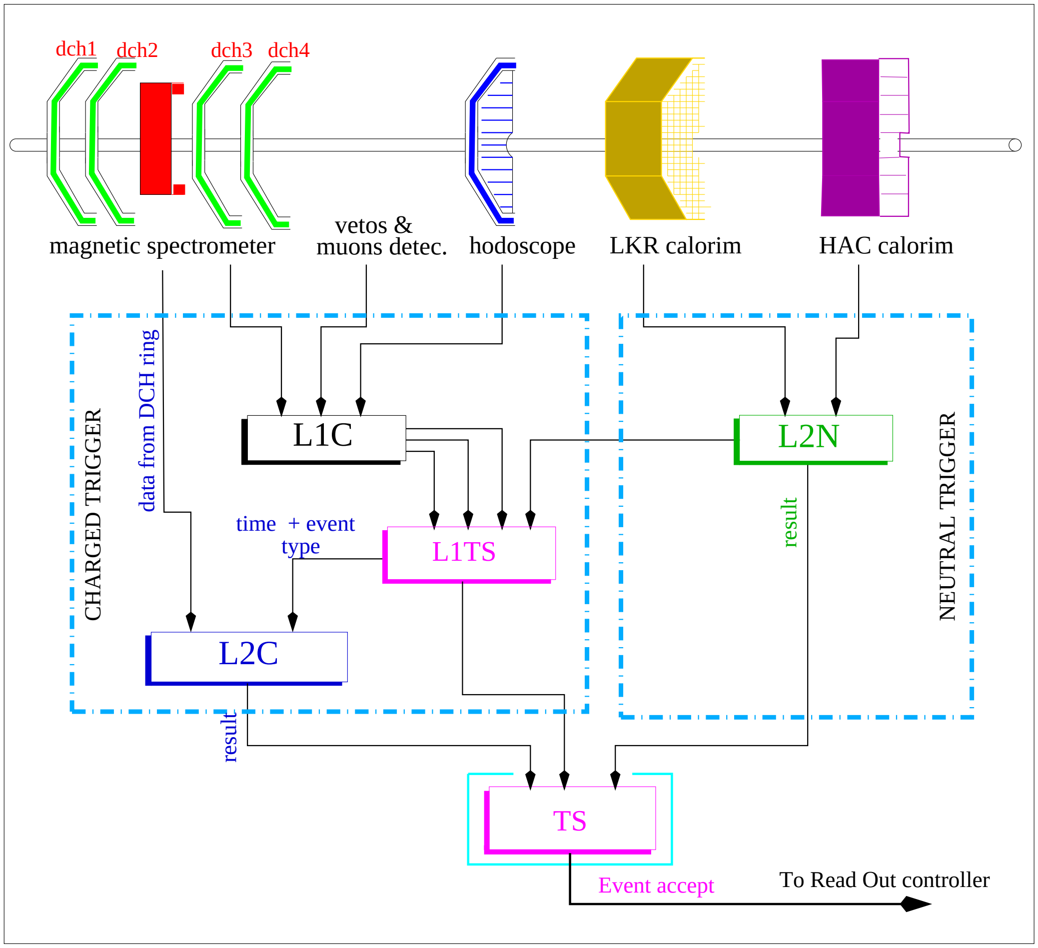

Figure 3.1: Scheme of the NA48 trigger system. Two independent systems trigger on charged and neutral decays (charged trigger and neutral trigger respectively). A third system (the trigger supervisor) correlates the former trigger information and produces the final decision to record the data.

3.1 The trigger supervisor

The whole NA48 experiment is synchronized by a 40 MHz clock[49] and the time is defined for all subsystems by this clock in units of 25 ns (time-stamps). All events are associated with a time-stamp value, representing the time at which the event was detected in some part of the detector. Data from all sub-detectors are continuously digitized and stored in circular memory buffers (ring buffers) 200 μs deep every 25

ns.

The NA48 Trigger Supervisor[50] (TS) is a fully pipelined 40 MHz digital system which correlates and processes the information from the local trigger sources. It provides the final trigger word, indicating the required conditions fulfilled, and including the event time-stamp (event time in clock units). The TS broadcasts the trigger word to all Read Out Controllers (ROCs) that control the ring buffers and interface them to the data acquisition PC's. The trigger word transmission is de-randomized, in order to guarantee a minimum interval between two consecutive read-out requests. Fig. 3.2 shows a schematic view of the TS electronic.

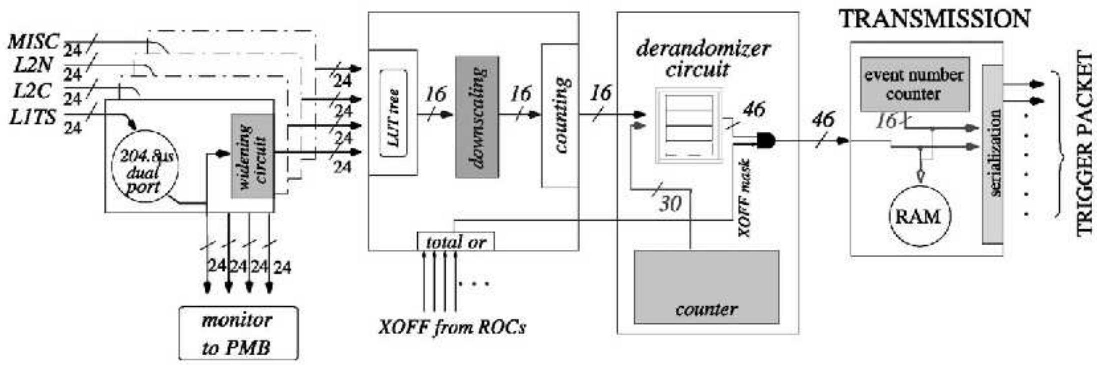

Figure 3.2: Scheme of the trigger supervisor. The TS has been implemented on 8 VME boards, connected by a private bus and monitored by a single board CPU.

3.2 The L1 Trigger

The LV1 trigger is a hardware trigger built from fast information coming from subdetectors. The LV1 for semileptonic hyperon trigger is composed in the following way:

$$Q1 \cdot \overline{AKL} \cdot \overline{1TRK} \cdot (E_{LKr} + E_{TOT}) + Q1/D$$

Here and in the following sections the dot means logical *and*, the plus means logical *or*.

As explained later, in the initial part of the data taking period (before run 13941) the $\geq 2TRK$ condition was used in place of the $\overline{1TRK}$ condition. Now I will explain the meaning of each request:

$Q1$ **:** At least one sub-coincidence between the horizontal and the vertical plane of the charged hodoscope. The definition of the sub-coincidences comes from a time and space coincidence between the hits in a group of horizontal scintillators and the hits in a group of vertical scintillators. The groups are composed of 7 scintillators near the beam pipe or from the remaining 9 scintillators of the quadrant far from it. Hence for each quadrant we have 4 sub-coincidences for a total number of 16 sub-coincidences. After that definition we can ask for a single coincidence (Q1), for two (Q2) and so on. In our semileptonic hyperon decay we have two tracks and then it would be natural to ask for a Q2, but the space region covered by a single sub-coincidence is at least 50×50 cm in the x-y plane and it may happen that the two tracks hit the same sub-coincidence. The choice to use Q1 rather than Q2 was based on data collected in the 1999 test run where we measured an inefficiency of the Q2 near 10% for our signal events.

$\overline{1TRK}$ **:** A number of hits in the planes of the first DCH consistent with the presence of more than 1 track. In particular the request is at least 3 views with more than 2 hits, (in standard conditions 1 track corresponds to 2 hits, one for each plane).

$(\geq 2TRK)$ **:** A number of hits in the planes of the first DCH consistent with the presence of 2 or more tracks. In particular the request is at least 3 views with more than 3 hits. It turns out that this request has an intrinsic inefficiency at the level of 30 %. The inefficiency comes for the events with two tracks in which we have two or more inefficient wires on $DCH1$. The inefficiency is also related to defective areas in the DCH read-out in 2002 run (see chapter V). During the run the change of the LV1 configuration was due to the discovery of this inefficiency.

$\overline{AKL}$ **:** No in-time hits in the pocket 6 and 7 of the AKL.

E_{LKr} **:** The total energy of the event measured in the LKr must be bigger than 15 GeV.

E_{TOT} **:** The total energy of the event measured in the LKr and in the hadron calorimeter has to be bigger than 30 GeV.

$Q1/D$ **:** Trigger $Q1$ downscaled by a factor 1000. This loose trigger is used to monitor the efficiency of the main LV1 trigger component.

Essentially the LV1 trigger requires the presence of 2 tracks with some electromagnetic interaction in the LKr (E_{LKr}) or/and some hadronic interaction (E_{TOT}).

The output rate of LV1 in 2002 was of $\sim$ 50000 events/s (250000 events/burst); a small amount of these triggered events were directly written on disk (the downscaling factor was 25 before run 13941 and it was 35 from run 13941 until the end of run), without applying a further LV2 selection. The change in the downscaling factor was adopted to balance the increased number of events coming from the better efficiency of the 2TRK request after run 13941.

To take into account the change in the definition of LV1 I will perform two separated analyses for the two different periods.

Another useful LV1 trigger is the $T0N$; it asks for a left-right or for a top-bottom coincidence in the neutral hodoscope counters and I will use it to measure the efficiency of the main LV1 trigger. In fact a sample (with a downscaling factor of 100) of events coming from this trigger goes directly to the off-line filters.

The events passing this LV1 trigger were sent in input to the MBX. This was not the only input to the MBX, in fact in 2002 we also had another level 1 trigger essentially asking for the presence of two muons.

Finally during 2002 run for the normalization channel $\Xi^0 \to \Lambda\pi^0$ we also have a LV2 radiative hyperon trigger, looking for the decay of a Λ into a proton and a pion. Nevertheless for this channel the events collected into the downscaled LV1 sample and directly acquired are sufficient for our purpose of measuring the BR of

Ξ^0 beta decay. The use of these data gives two advantages, first we can reconstruct a Ξ^0 sample with a low bias coming from trigger selection, second we avoid the calculation of a complex LV2 trigger efficiency.

3.3 The Massbox

The MBX trigger subsystem[51] is based on a partially pipelined hardware and a small processing farm (see fig. 3.3). For each accepted charged LV1 event it analyzes information from the first, second and fourth drift chambers of the magnetic spectrometer. Dedicated FPGA-based components associate hits in this chamber to the coordinates of crossing particles. A event builder, the Event Dispatcher (ED), routes all computed coordinates within the event, to an Event Worker (EW) processor of the farm. The processor reconstructs tracks of the particles, evaluates invariant masses of multi-track systems and applies various kinematic constraints in order to accept or reject the event. The EW processor farm is composed of eight single board computers. For the first available event, ED sequentially routes event data fragments from its inputs to the first ready Event Worker. Upon reception of all event data fragments, the EW processor executes event selection algorithm and produces a trigger word that summarizes some characteristics of the event. It then sends the trigger word to the TS.

The MBX logic is an asynchronous real-time queuing system that produces event decisions in a time which can vary from event to event. However, a fixed upper limit of 100 μs for generation of trigger words is imposed by the 204.8 μs data persistency interval in the sub-detectors ring buffers.

Events that require more computation time than the given upper limit are flagged as being "out of time events". In 2002 run, apart for a small fraction acquired (downscaling factor = 10), this kind of events were discarded. This solution may be one of the source of our LV2 inefficiency; nevertheless in the downscaled sample of "out of time events" I didn't find events satisfying my signal selection.

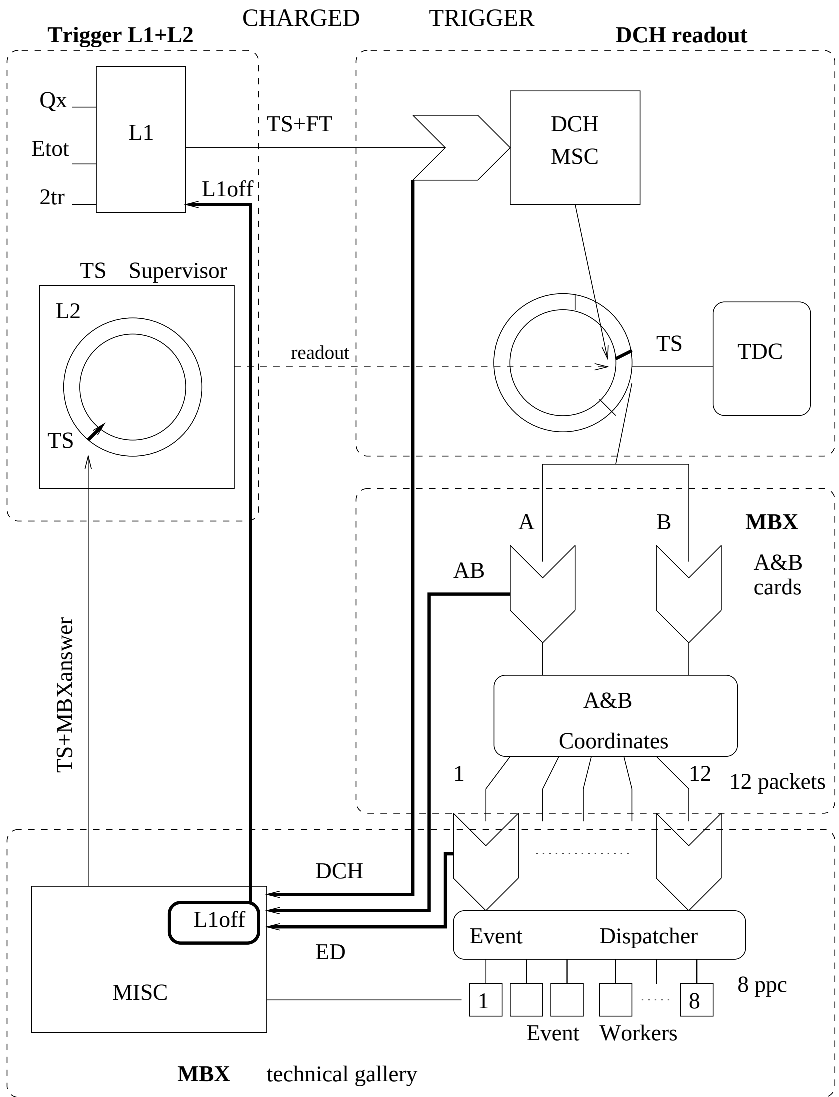

Figure 3.3: Scheme of MBX. The inter-links with the DCH read-out and the TS are also shown.

3.4 The L2 trigger

For the events with LV1 on, the information on charged particles collected from the DCHs read-out are sent to the MBX. Here the LV2 requests are applied to the on-line reconstructed quantities. For the events coming from hyperon beta decays the LV2 trigger as defined as follow:

$$z_{OK} \cdot DCH1_{DIST} \cdot \overline{(M_K \cdot P_R^T)} \cdot \overline{M_\Lambda} \cdot \overline{M_{\overline{\Lambda}}} \cdot P_{RATIO}^L \tag{3.1}$$

The meaning of the different components is:

z_{OK} **:** two tracks giving a vertex with z between 100 cm and 5100 cm from K_S^0 target. A vertex is defined if the two tracks have a closest distance of approach lower than 5 cm

$DCH1_{DIST}$ **:** The distance between the hits of two tracks in the first DCH has to be bigger than 5 cm

$\overline{(M_K \cdot P_R^T)}$ **:** If the momenta of the two tracks are balanced (the ratio between these momenta is not too high or too low) than the invariant mass of the same two tracks, supposing that they are produced by two charged pions, must not be consistent with the mass of a neutral kaon. Precisely the following relation must not be satisfied: $(\frac{p_{bigger}}{p_{smaller}} < 5) \cdot [(m(\pi,\pi) - m_{K^0}^{PDG})^2 < 0.1(m_{K^0}^{PDG})^2]$. This cut obviously is applied to reject events coming from the decay $K_S \to \pi^+\pi^-$.

$\overline{M_\Lambda}$ **:** The invariant mass of the two tracks, supposing they are produced by a proton and a pion, has not to be consistent with the mass of a Λ. Namely the following relation has not to be satisfied: $(m(p,\pi) - m_\Lambda^{PDG})^2 < 0.02(m_\Lambda^{PDG})^2$ This cut is applied to reject events coming from the decay $\Lambda \to p\pi^-$. In fact a large number of Λ are produced in the K_S target, additional Λs come also from the decay $\Xi^0 \to \Lambda\pi^0$.

$\overline{M_{\overline{\Lambda}}}$ **:** The invariant mass of the two tracks, supposing they are produced by an anti-proton and a pion, has not to be consistent with the mass of a Λ. The following relation has not to be satisfied: $(m(p,\pi) - m_\Lambda^{PDG})^2 < 0.02(m_\Lambda^{PDG})^2$. The cut is applied to reject the $\overline{\Lambda}$ coming from K_S target.

P_R^L **:** The momenta of the two tracks must be unbalanced. We are looking for a beta decay in which a big amount of Ξ^0 energy is taken from the Σ^+ and then from the proton. Indeed the MC indicates that the ratio between proton and electron momenta is always bigger than 4 in the laboratory frame. The trigger request is: ($\frac{p_{bigger}}{p_{smaller}} > 3.5$).

In 2002 the output rate of this LV2 trigger was $\sim$ 10000 events/burst

A complication for the calculation of LV2 trigger efficiency is intrinsically present in the MBX algorithm. As showed in fig. 3.4 all inputs are processed following the same iter and if one event satisfies a certain request it is flagged as good skipping the evaluation of the remaining LV2 triggers. In such a case we have a so called "short cut". In principle we would decrease our LV2 trigger efficiency if we disregard this class of events, since in our trigger logic no response from a trigger is treated as a negative response. Then in order to avoid trivial inefficiencies we have to include in our analysis also the trigger producing "short cuts" with respect to our main trigger.

There are two LV2 triggers of this kind:

4 tracks: at least 4 reconstructed tracks in the MBX

2 μ: at least 2 reconstructed tracks in the MBX associated with 2 hits in the muon detector

Nevertheless I will show that in the final sample the number of events coming from **4 tracks** and from **2 μ** are small. Indeed a posteriori we can assert that the exclusion of these triggers from our analysis does not introduce any trigger inefficiency for the signal.

3.5 The L3 trigger for the signal

The LV3 trigger is a software selection of events; it works off-line, with a delay going from 30 minutes to some hours with respect to the data taking, depending on the efficiency of data acquisition. All the information about the event can be used and the only difference with respect to the final sample used for the analysis is the fine calibration of sub-detectors, still not available at this stage.

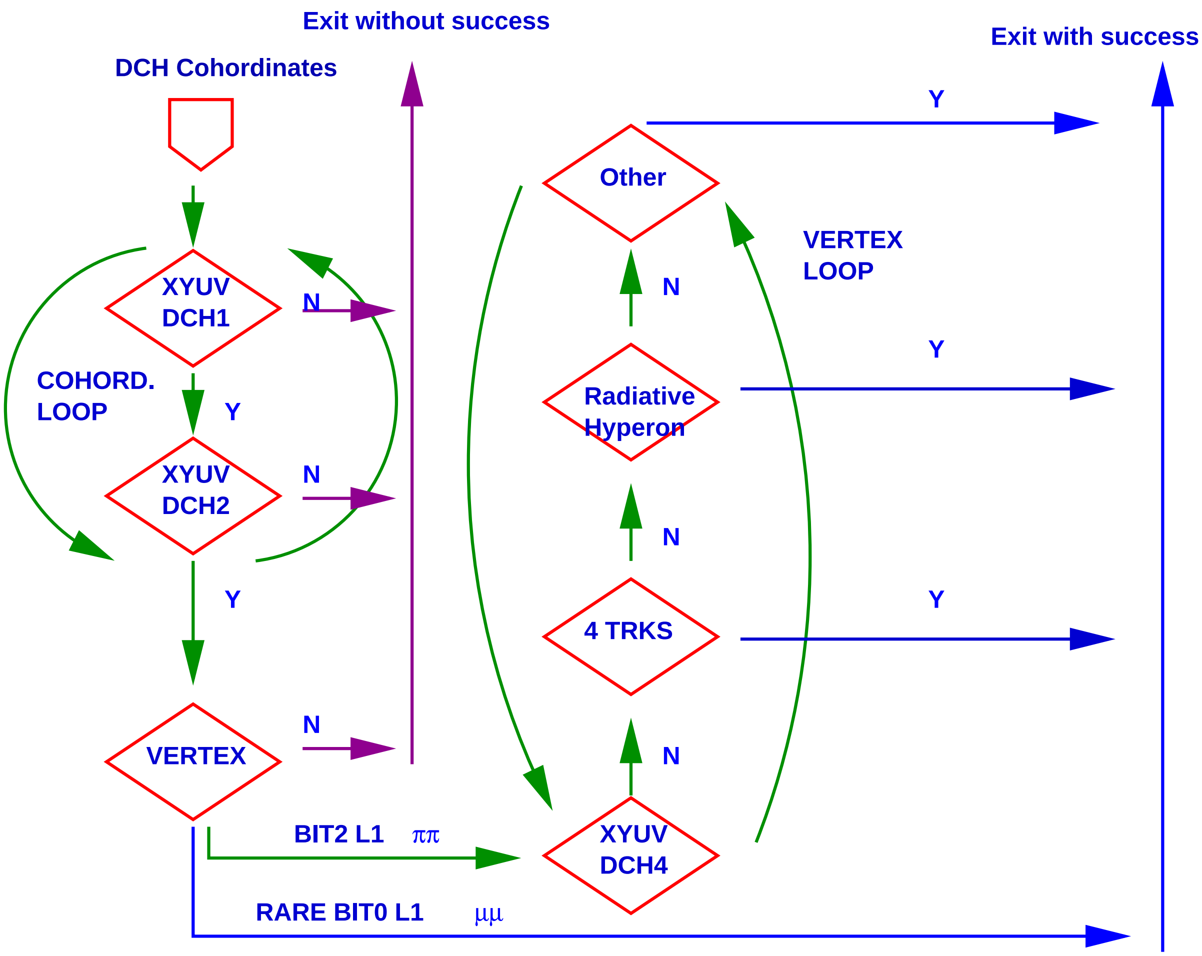

Figure 3.4: Description of MBX algorithm.

The inputs to the LV3 filter of Ξ^0 beta decay are the events collected by the following triggers:

- LV2 Hyperon beta decay
- 4 tracks
- 2 μ
- $T0N$ (downscaling 70)
- main LV1 trigger downscaled

The cut applied are:

- At least 1 positive track reconstructed in the spectrometer
- At least 1 negative track reconstructed in the spectrometer
- less than 25 electromagnetic clusters in the LKr calorimeter; this cut is applied to reject events with hight accidental activity.
- At least 2 clusters in the LKr calorimeter with an energy greater than 2 GeV. In fact the signal events produce at least 3 clusters in the electromagnetic calorimeter, 2 clusters coming from the photons produced by the π^0 decay and 1 cluster produced by the electron.
- At least 1 track with a momentum greater than 20 GeV/c
- At least 2 tracks with a momentum ratio greater than 3.5 or lower than $\frac{1}{3.5}$
- At least 1 track with the ratio between the energy of the associated cluster measured in the LKr (E)and the momentum measured from the spectrometer (p) greater than 0.85 . This cut is applied to identify the presence of an electron (positron) that is completely absorbed in the LKr
- At least 1 track with E/p less than 0.95 . This cut is applied to identify the proton, that typically is not absorbed in the LKr.

The output of this LV3 trigger was $\sim$ 3000 events/burst, 2000 of which coming from the LV2 hyperon beta decay and the remaining from the minimum bias triggers and from the short cuts. A 2% of events going in input to LV3 are directly written on disk without any LV3 selection. These events are the control sample to measure the LV3 trigger efficiency.

3.6 The L3 trigger for the normalization channel

The hyperon radiative trigger was built to select all the events containing at least a decay $\Lambda \to p\pi^-$ and some more activity in the LKr. In this way we can collect several interesting decays like $\Xi^0 \to \Lambda\pi^0$, $\Xi^0 \to \Lambda\gamma$, $\Xi^0 \to \Lambda e^+e^-$, and $\Xi^0 \to \Sigma^0\gamma$ with $\Sigma^0 \to \Lambda\gamma$. For our analysis this LV3 trigger is important because it ensures the acquisition of the normalization channel $\Xi^0 \to \Lambda\pi^0$. The radiative hyperon LV3 trigger takes the input from the following on-line triggers:

- LV2 hyperon radiative decay
- 4 tracks
- 2 μ
- $T0N$ (downscaling 70)
- main LV1 trigger downscaled

Nevertheless, as already explained and taking also into account the abundance of detected events coming from the normalization channel, I will only consider the output of the downscaled LV1.

Now I will review the cuts applied on the LV3 hyperon radiative trigger:

- At least 1 vertex between 2 tracks with $CDA \leq 5\ m$
- At least 1 vertex with$|m(p,\pi^-) - m_\Lambda^{PDG})| \leq 10\ MeV$ (charged vertex consistent with the decay $\Lambda \to p\pi^-$)
- At least 1 cluster in the LKr with distances greater than 5 cm from the reconstructed impact points of the tracks defining the Λ vertex.
- The last cut is applied on the cluster candidates selected by the previous cut: At least 1 cluster with energy $\geq 10\ GeV$ <u>or</u> at least 2 clusters with energy $\geq$ 2 GeV

Asking for a Λ vertex this LV3 trigger reduces drastically the output rate with respect to the input one. E. g., the LV1 trigger downscaled produces an input rate to the LV3 of $\sim$ 8000 events/burst; after the application of this filter only $\sim$ 200 events survive and are written on the tape. In table 3.1 are summarized the output rates of the triggers I use in my analysis and the size of the final samples.

decay	LV1 out	LV2 out	LV3 out	final 2002 sample
$\Xi^0 \to \Sigma^+ e^- \bar{\nu}_e$	50 KHz	2 KHz	2500 events/burst	600 M events
$\Xi^0 \to \Lambda\pi^0$	1.6 KHz	no LV2	200 events/burst	50 M events

Table 3.1: Trigger rates for 2002 run. The LV1 input can roughly be assumed to be equal to the Q1 rate that in 2002 was of ~ 1.5 millions events/burst (300 KHz).

3.7 Data acquisition

If a trigger is issued by the Trigger Supervisor, the sub-detectors send data for that event to the on-line PC farm[52]. The PC farm consists of 9 sub-detector PCs, 8 event building PCs and a control PC, each running Linux.

For each sub-detector the NA48 read-out system has one PC (four PCs for the LKr) receiving and storing data from the buffers contained in the ROCs. The event building PCs rearrange the data from each sub-detector PC and build the complete “event”.

The transfer of information between the PCs is performed by a fast ethernet switch. Each PC can send (receive) information to (from) the switch at a rate of 200 $Mbit/s$. During the SPS bursts the sub-detector PCs collect data. At the end of the burst, during the inter-spill time, the data are checked and partitioned into eight blocks. Each block is sent to one of the eight event builder PCs and the complete events are then rearranged. The data are then sent, via a 7 km fast ethernet link, to the CERN computing center and stored into disks. At this point the events are fully reconstructed and then they are processed by the LV3 filters.

The events satisfying the LV3 filters are saved to tape mainly in two formats: $GOLDRAW$ and $GOLDCOMPACT$. The $GOLDRAW$ data format contains the unreconstructed sub-detector information. The $COMPACT$ data format contains a subset of reconstructed quantities and it is used for a preliminary physics analysis.

After the definition of all the sub-detector calibrations, and on the basis of the analysis of the $COMPACT$ stream, the $GOLDRAW$ data are reprocessed to produce the final version of the $COMPACT$ data and finally the $SUPERCOMPACT$ stream, containing for all the events only the information useful for the final analysis. In table 3.2 I show the size of the samples used for the analysis.

For the 2002 run the $SUPERCOMPACT$ sample was later transfered to the NA48-Italy farm of Pisa and then from this farm I transfered the sub-sample needed for the measurement to the NA48 farm of Perugia where the analysis was performed.

2002 samples	$GOLDRAW$	$COMPACT$	$SUPERCOMPACT$
$HYPERON$	25 TB	3000 GB	600 GB
$LV3\ auto - pass$	2 TB	250 GB	50 GB

Table 3.2: The data size of 2002 samples used for the BR measurement of the Ξ^0 beta decay. The first sample ($HYPERON$) contains the signal and normalization events, the second one ($LV3\ auto - pass$) was used to estimate the LV3 filter efficiency.

Chapter 4

The Monte-Carlo simulation

A Monte-Carlo simulation is used in this analysis, to determine geometrical acceptances and to perform background studies. For this purpose the standard NA48 Monte-Carlo program, called $NASIM$, has been adapted to include the possibility to simulate hyperon decays. This chapter introduces the main features of the program and describes the work performed to introduce hyperon decays and tune some of the generation parameters.

Section 4.1 gives a general introduction to the Monte-Carlo. Here the main options of the particle simulation are described and the aspects for which the simulation cannot be relied upon are explicitly emphasized.

The characteristics of the beam have been adjusted using experimental data. The momentum spectrum is discussed in section 4.2. From the data collected in a special run in 1999 the Ξ^0 and Λ spectra were fitted and introduced in the generator. Due to the different proton energy used in the 2002 run, this represents only a first approximation and corrections were developed in order to reproduce the data distributions. The correct reproduction of the geometry of the beam requires fine tuning of the target and collimator position. This aspect is discussed in section 4.3.

Decay generators developed include those for the signal channel $\Xi^0 \to \Sigma^+ e^- \bar{\nu}_e$, for the normalization channel $\Xi^0 \to \Lambda\pi^0$ and for the dominant sources of background. The decay amplitudes used and the assumptions made for the values of the form factors have been discussed in chapter 1 and will not be repeated here. Section 4.4 presents instead some checks that have been performed to verify the results. In particular the calculation of the Σ^+ polarization in the semileptonic decay channel, which has required heavy algebraic calculations, has been checked comparing the results with explicit results found in the literature for a special case.

The chapter ends with a comparison between data and Monte-Carlo for the signal and normalization channel, presented in section 4.5.

4.1 General feature of the Monte-Carlo

With the exception of AKL and $NHOD$ sub-detectors the $NASIM$[53] Monte-Carlo describes accurately the geometry of all sub-detectors according to their descriptions given in chapter 2.

In $NASIM$ physical processes, such as multiple scattering, conversions, etc.. are simulated with the $GEANT3$[54] package. The available processes are listed in table 4.1. The magnet current and its polarity can also be set. I use this feature to generate samples with both magnet polarities. In fact in the 2002 run the magnet polarity was inverted every week, usually during the SPS machine development.

Full $GEANT3$ simulation of shower development in the NA48 calorimeters is a very CPU-intensive task which takes several CPU-seconds per particle. In order to reduce this time we use a shower library file that is read from $NASIM$ during its execution. This file contains the energy deposited channel-by-channel in the calorimeters by single particle events. In this way we can simulate the calorimeter response taking $\sim 50\ ms$ per event of CPU-time. The shower library is produced using real data. The library I use in my simulation was created from data of a 1998 run. Nevertheless, after data-MC comparison, we see some discrepancies in the simulation of hadronic showers. For this reason I will not apply cuts on the HAC quantities in order to avoid the introduction of a bias resulting from an inaccurate reproduction of the same cut in the MC.

Other critical quantities in the MC are the particle's times. Time cuts are then

NASIM options

Physics process	used
Positron annihilation	yes
Bremsstrahlung	yes
Compton scattering	yes
Decay in flight	yes
δ-ray production	yes
hadron interaction	yes
Continuous energy loss	yes
Multiple scattering	yes
Photoelectric effect	no

Table 4.1: NASIM options for the simulation of physics processes.

applied symmetrically for the signal and for the normalization channel only in the data.

Again exclusively from data I will estimate the effect of the accidental activity from the K_S^0 beam that is not reproduced at all in the MC.

Finally, again to gain CPU-time, we can avoid the full simulation of events outside the geometrical acceptance of the sub-detector. I will use this option for the normalization channel $\Xi^0 \rightarrow \Lambda\pi^0$, where in order to generate an amount of events comparable with the final sample I found in real data, I need to speed up the event-generation. This decay produces two tracks (proton and pion) and two clusters (γs) from π^0 decay. If one of the two tracks has a distance greater than 150 cm from the beam pipe axis at the first DCH or if one of the two gammas has a distance greater than 125 cm from the beam pipe at the LKr, the event is not simulated through the sub-detectors.

In fig. 4.1 I give a graphic representation of these kinematic cuts. Of course for the calculation of the acceptance I take into account the events that do not satisfy the kinematic checks. Before applying this procedure for the final MC production of the normalization channel I checked in a test sample that before and after the application of the kinematic cuts the number of events passing my selection did not change.

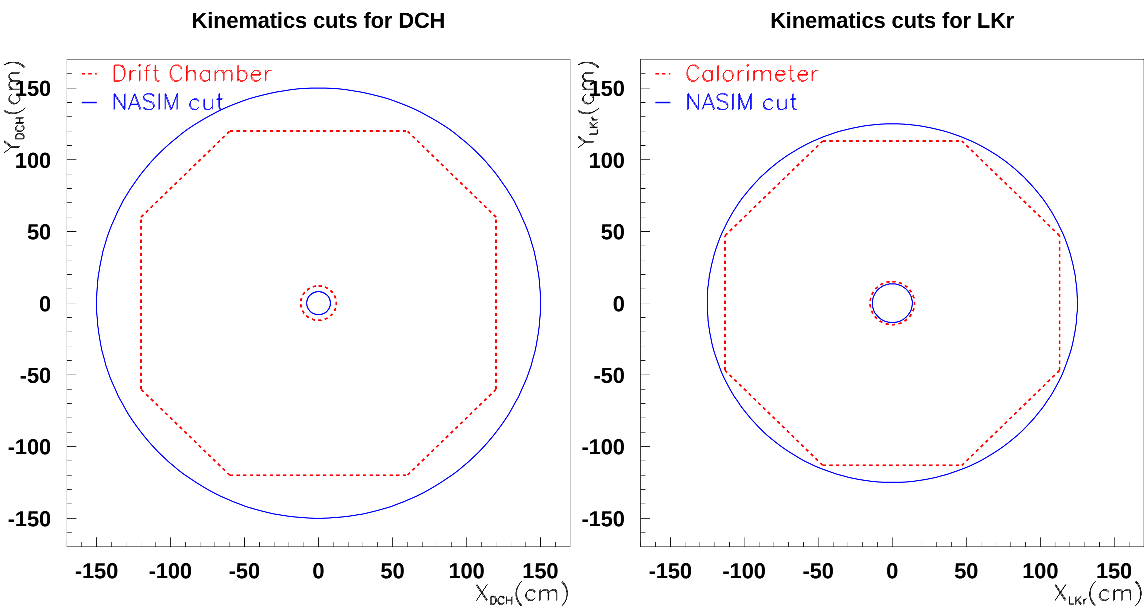

Figure 4.1: Kinematic cut to allow full simulation for tracks (left) and γs (right).

4.2 The Ξ^0 spectrum

The Ξ^0 spectrum was fitted using the $\Xi^0 \to \Lambda\pi^0$ contained in the data collected with a special run in 1999. This special run, 48 hours long, was taken with different beam conditions with respect to the 2002 run. The primary proton beam had an intensity of $1.5 \cdot 10^{10}$ protons per pulse (3 times lower than in 2002), the proton energy was 450 GeV and there was no absorber. The production angle (4.2 $mrad$) was instead the same.

The result of the fit was parametrized for the Monte-Carlo with the following function:

$$W(p_{\Xi^0}) = \frac{0.0144 p_{\Xi^0}^2}{p_p} e^{\frac{-13.37 * p_{\Xi^0}}{p_p}} \tag{4.1}$$

where p_p is the primary proton momentum.

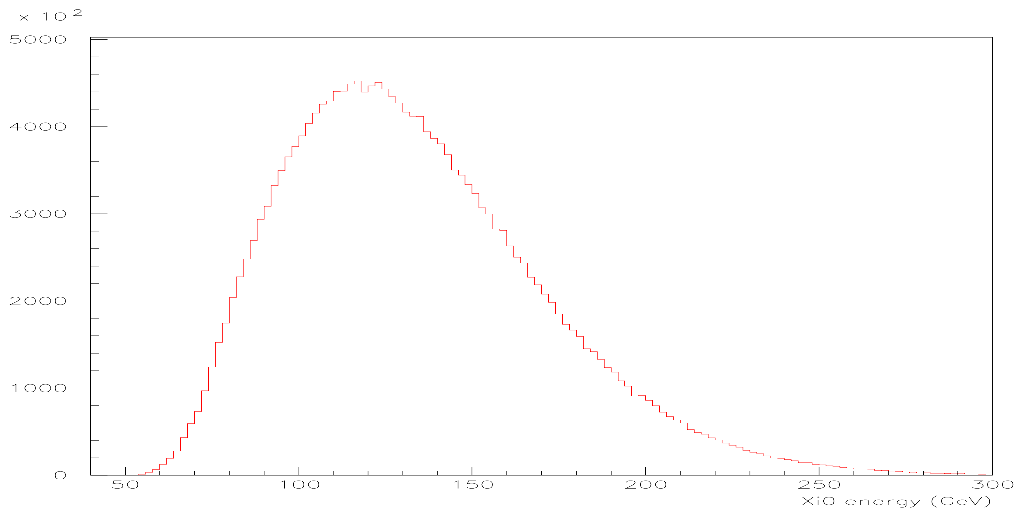

Figure 4.2: Ξ^0 spectrum on the laboratory rest frame directly from the generator; The MC data are generated with a starting Ξ^0 polarization along x axis of - 10% along the x axis.

Our final sample of $\Xi^0 \to \Lambda\pi^0$ decay, collected with a loose trigger (see next chapter) was the best sample to check the goodness of this spectrum with a data MC comparison. After applying the same selection to real data and to Monte-Carlo data we saw the presence of a small discrepancy. For that reason we apply a correction to the function 4.1 multiplying it by a polynomial of degree three.

The Ξ^0 spectrum we obtain is plotted in fig. 4.2 directly from the generator and after the selection in fig. 4.3 superimposed to the same distribution from real data. We now see a better agreement between data and MC.

Using the new spectrum we have produced MC samples for the signal, the normalization channel and the main background ($\Xi^0 \to \Lambda\pi^0$ with $\Lambda \to pe^-\bar{\nu_e}$). Using the PDG value for the Ξ^0 lifetime we generate Ξ^0 with a momentum between 40 GeV/c and 300 GeV/c and a z between 3 m (2 meter before the defining collimator) and 60 m from the K^0_S target.

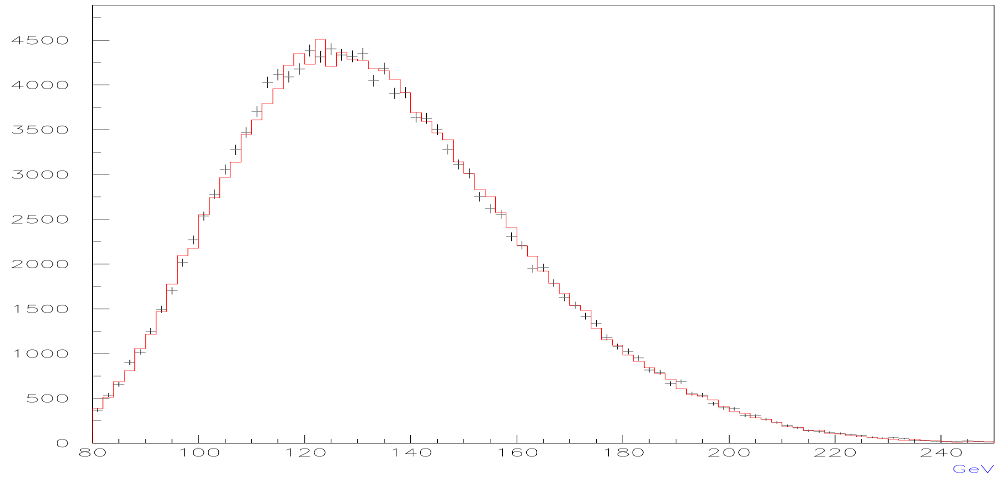

Figure 4.3: Ξ^0 spectrum in the laboratory rest frame for the normalization channel; in black the real data and in red the MC data. The MC data are generated with a starting Ξ^0 polarization along x axis of - 10%.

4.3 Reference frame and beam geometry

The collimator geometry is fully described in $NASIM$ together with the target. The relative position between them is used for the determination of the angular distribution of the generated Ξ^0s. In fact the Ξ^0s are flatly generated in the solid angle dΩ corresponding to the collimator aperture seen from the target.

Then the absolute position of the target and the relative position between the target and the collimator in the MC are fundamental for a reliable simulation.

As explained in section 2.1 to allow the introduction of the absorber and of its mechanical support the K_S^0 target was displaced upstream by 0.234 m. In the MC we take into account this change of the beam configuration, nevertheless for our purposes we need also a fine tuning of the K_S^0 target position along x and y direction.

To precisely measure from the collected data the target position I select $K^0 \rightarrow \pi^+\pi^-$ decays (I use a standard selection criterion developed for the ϵ'/ϵ analysis).

Then for the selected sample I plot the average displacement d between the nominal target position and the decay planes defined by the directions of the two πs defined by:

$$d = \frac{\vec{p}_{\pi^+} \times \vec{p}_{\pi^-}}{|\vec{p}_{\pi^+} \times \vec{p}_{\pi^-}|} \cdot V\vec{N} \tag{4.2}$$

where $V\vec{N}$ is the vector that joins the vertex position (V) and the nominal target position (N).

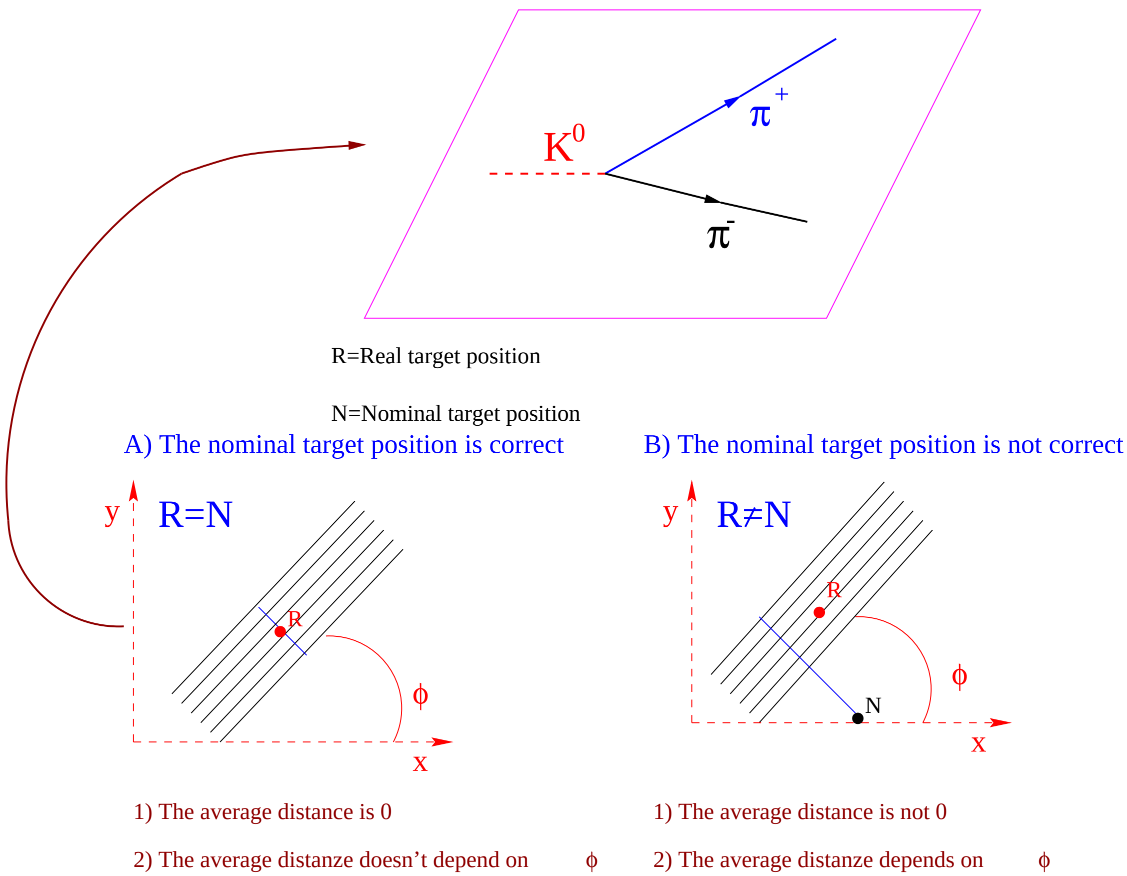

Figure 4.4: Effect of a wrong nominal position for the target position: if the nominal position of the target is correct then the average distance of the decay planes from this position is 0 for all the values of ϕ, on the contrary if the nominal position of the target is not correct this average distance is not 0 and it depends on ϕ.

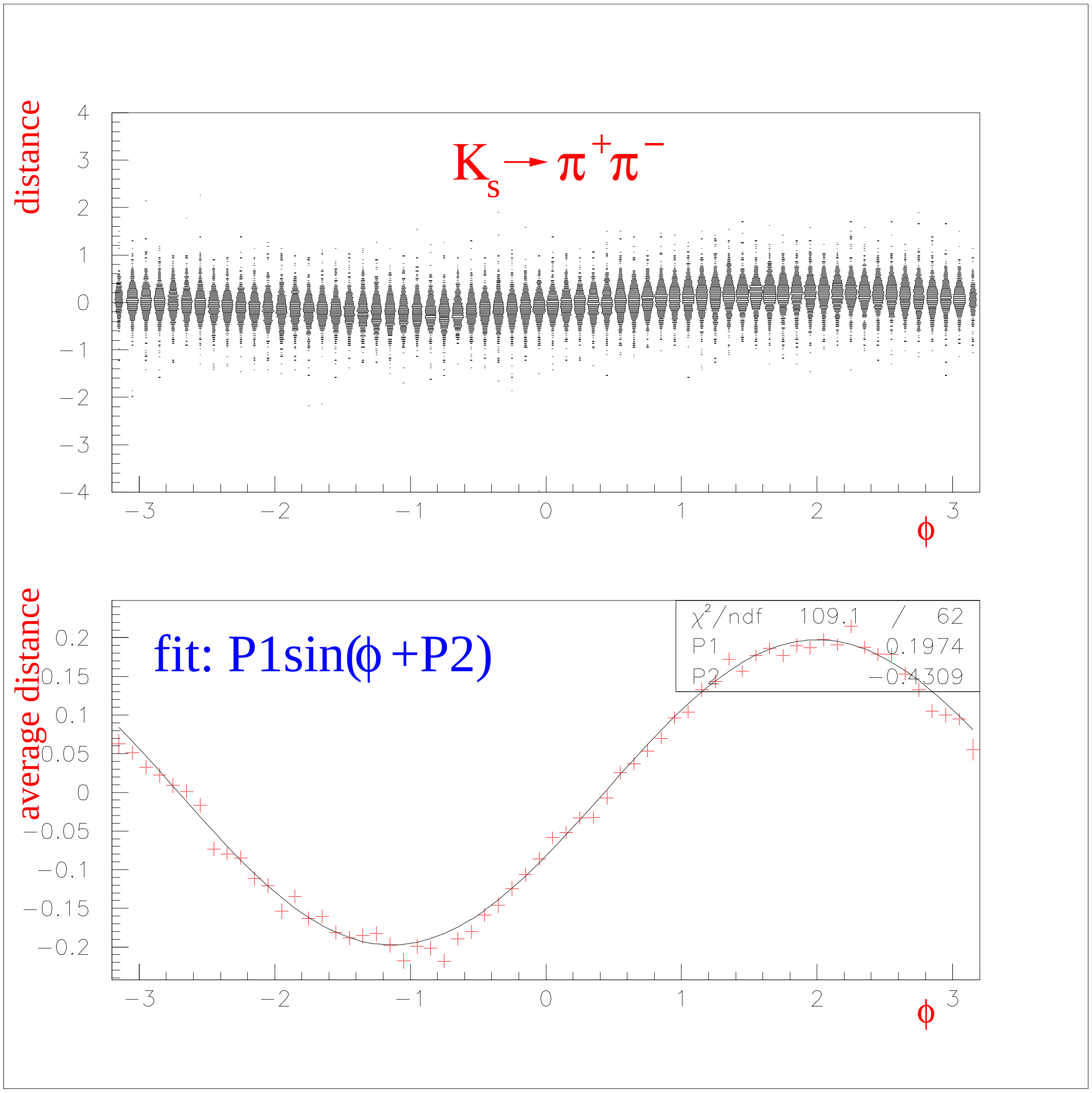

Figure 4.5: Distribution of the displacement in *cm* between the decay planes and the nominal position of the target as a function of the ϕ angle for $K^0 \rightarrow \pi^+\pi^-$ decays in the 2002 data <u>before</u> the correction of the target position. On the top the scatter-plot and on the bottom the profile histogram.

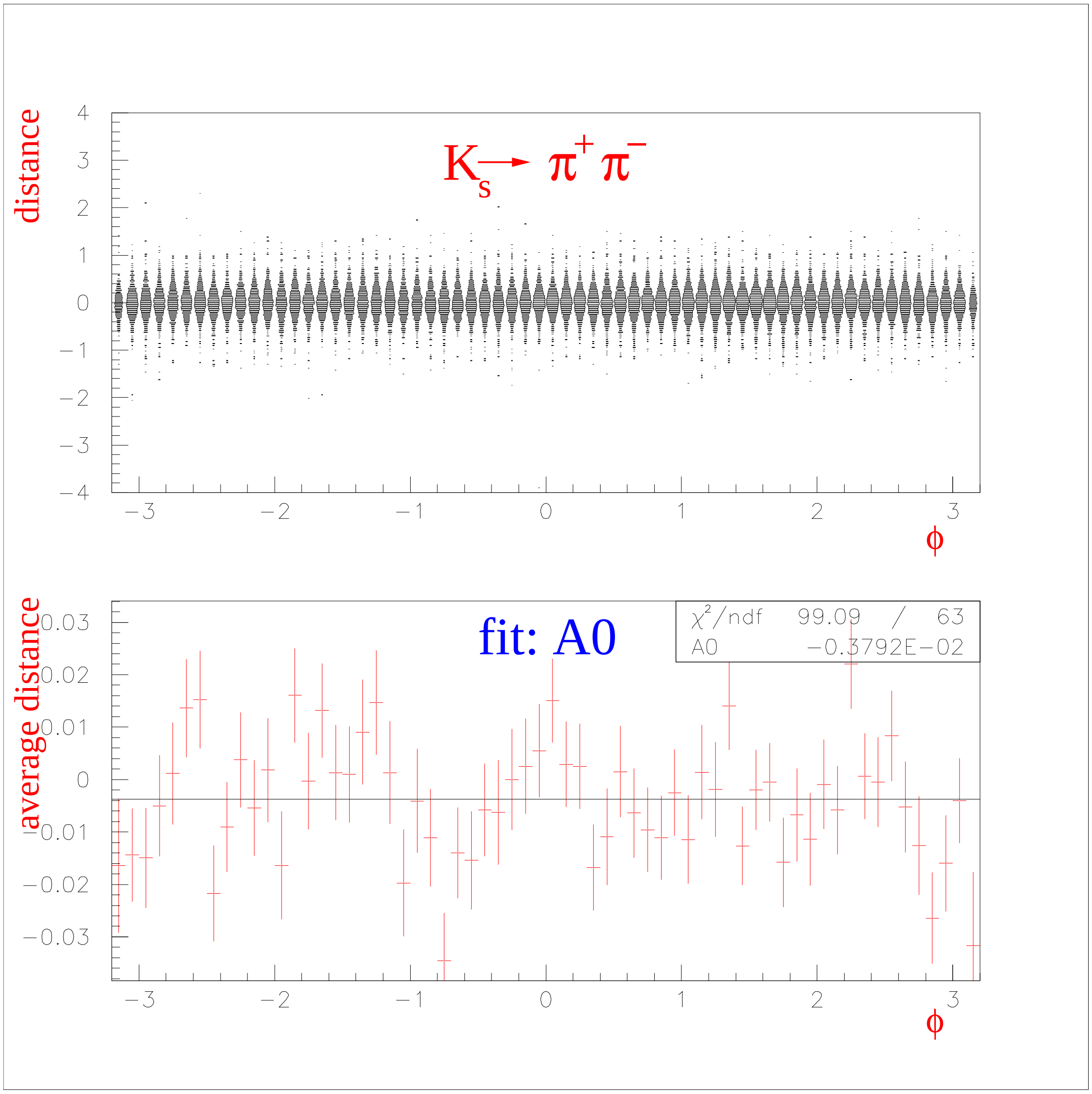

Figure 4.6: Distribution of the displacement in *cm* of the decay planes from the nominal position of the target as a function of the ϕ angle for $K^0 \rightarrow \pi^+\pi^-$ decays in the 2002 data <u>after</u> the correction of the target position. On the top the scatter-plot and on the bottom the profile histogram.

As explained in the sketch of fig. 4.4, if the nominal target position coincides with the real target position, this distribution is always centered at zero and it does not depend from ϕ (the azimuthal angle of the normal to the decay plane). Otherwise if the nominal position of the target does not coincide with the real target position this distribution is not centered at 0 and it will depend from ϕ.

The results we obtain are shown in fig. 4.5. The existence of a correlation between d and ϕ is clear.

Fitting this dependence with a sinusoidal function we find the magnitude of the mismatch between the nominal target position and the real one. The correction to apply is the following:

$$\Delta x = x_{real} - x_{nominal} = -0.880\ mm, \qquad \Delta y = y_{real} - y_{nominal} = 1.800\ mm \tag{4.3}$$

Taking into account the new target (x, y) position I reproduce the scatter plot of d versus ϕ; the new distribution is shown in fig. 4.6 and it doesn't show anymore a correlation between d and ϕ.

The target position is also checked tracking back the kaon momentum to the longitudinal position of the target and looking at the y versus x distribution. The results[55] obtained agree with the method explained here. From the distribution of the transverse kaon momentum we also check the relative position between the target and the collimator.

The position of the collimator has been adjusted checking that the distribution of the x and y component of the transverse momentum with respect to the nominal beam axis is the same in data and Monte-Carlo. These distributions are shown, for $K_S \rightarrow \pi^+\pi^-$ decays, in fig. 4.7.

4.4 Decay generators

The semileptonic decay of the Ξ^0 has been generated in the Ξ^0 rest frame using expression 1.15 for the differential decay rate as a function of the electron energy and the electron and neutrino directions. In this expression the D functions have

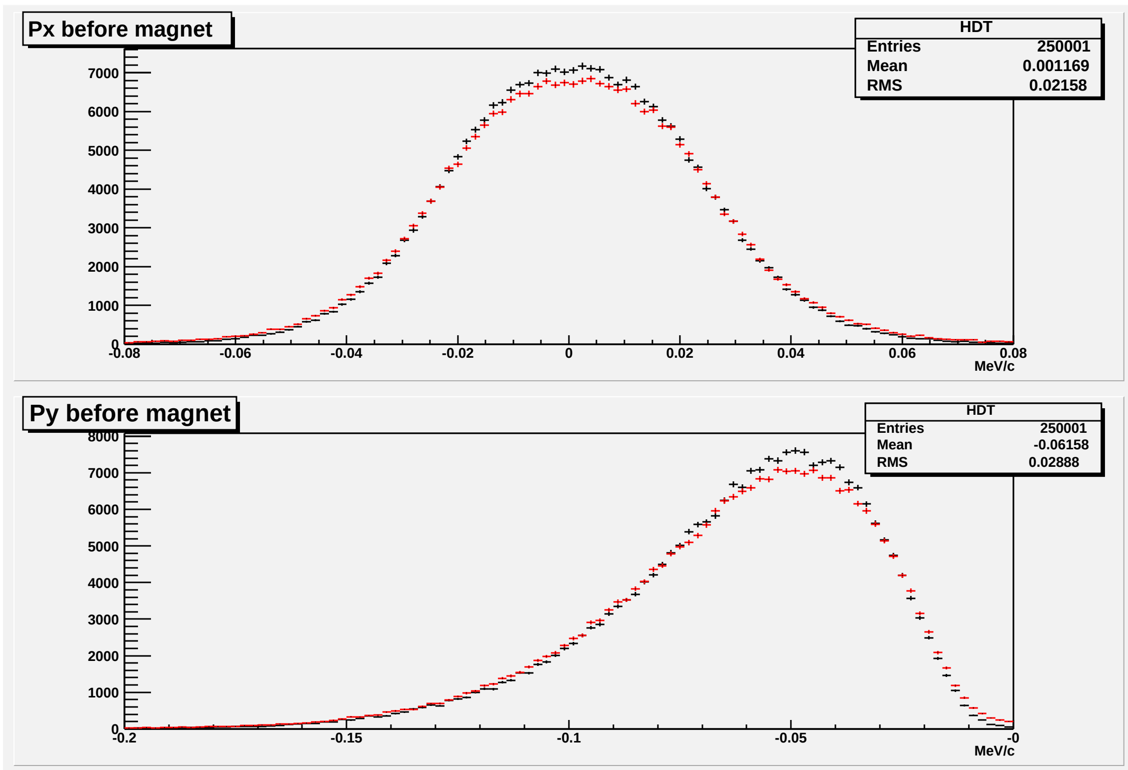

Figure 4.7: Distribution of the kaon momenta along x and in the y directions. The plots show the comparison between the data (red) and the MC after the fine tuning of the collimator position.

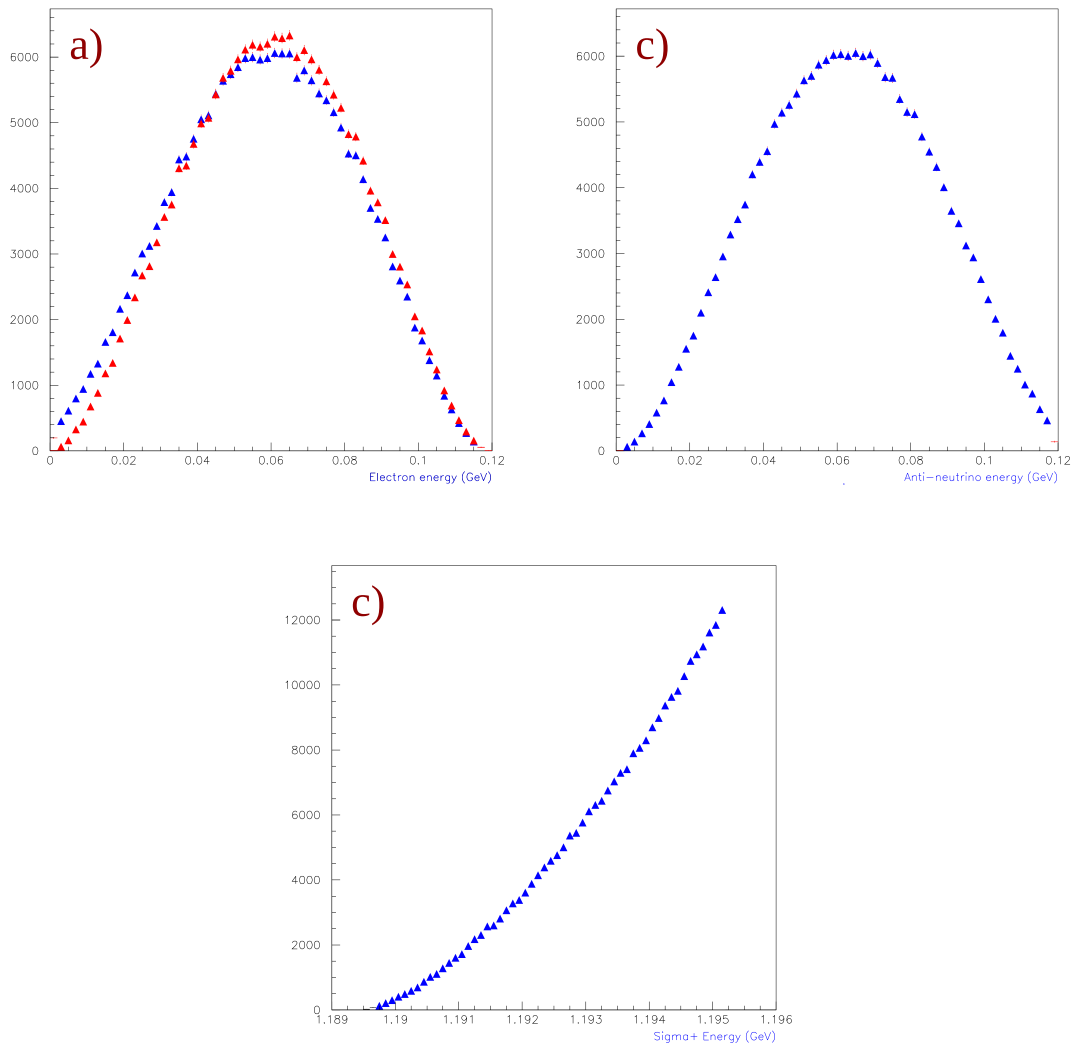

Figure 4.8: Energy spectra in the Ξ^0 RF for the electron (a), antineutrino (b) and Σ^+ (c): Phase space would give a flat distribution in these variables. The blue points include the radiative corrections and the effects of form factors dependence from q^2, the red points in (a) do not include those corrections.

been computed with form factors depending on q^2, the electron-neutrino effective mass, according to formulae 1.19, 1.20, and 1.21 and with their value at $q^2 = 0$ given by 1.25. Radiative corrections are included, following the treatment described in section 1.3. Figures 4.8 show the distributions obtained for the energies of the daughter particles in the Ξ^0 rest frame. For the electron spectrum (figure 4.8a) the effect of neglecting the radiative corrections and the q^2 dependence of the form factors is also shown.

A full check of the generation procedure has been performed comparing the momentum distributions shown, with those obtained using a completely independent procedure in which the daughter particles are generated according to three body phase space and then weighted with the matrix element given in [24].

The polarization of the decay Σ^+ is not small and it has to be accounted for properly, since, as discussed in section 1.7, it determines the distributions of the detected particles (proton and π^0). The polarization of the Σ^+ is also dependent on the polarization of the incoming Ξ^0, which is expected to be non zero, though small. A full treatment of the Σ^+ polarization, including the effects of the initial state polarization is only given in a paper by Linke[26]. The results have been given in section 1.6. Since the extraction of the information relevant for the Monte-Carlo generation from 1.26 required some heavy algebraic manipulation, I checked my results against those given, for the case of unpolarized Ξ^0, in [27].

Assuming the Ξ^0 polarization equal to 0, they give the Σ^+ polarization along the electron and anti-neutrino directions. In fact since the anti-neutrino is a right-handed particle and the electron is a left-handed particle (if we neglect its small mass), angular momentum conservation implies that the Σ^+ polarization is strongly correlated to these two directions. Putting to 0 the Ξ^0 polarization from 1.26 we obtain the simpler relation:

$$P_b^\mu = \frac{\mathcal{K}_\rho^{(\mathrm{b})}}{\mathcal{K}_{00}} g^{\mu\rho} \tag{4.4}$$

In fig. 4.9 and in fig. 4.10 I show the perfect agreement that I obtain in that particular condition. These plots show the Σ^+ polarization along the electron and anti-neutrino direction for different values of the g_1 form factor. They are obtained from two toy Monte-Carlos where I have implemented the two different calculations.

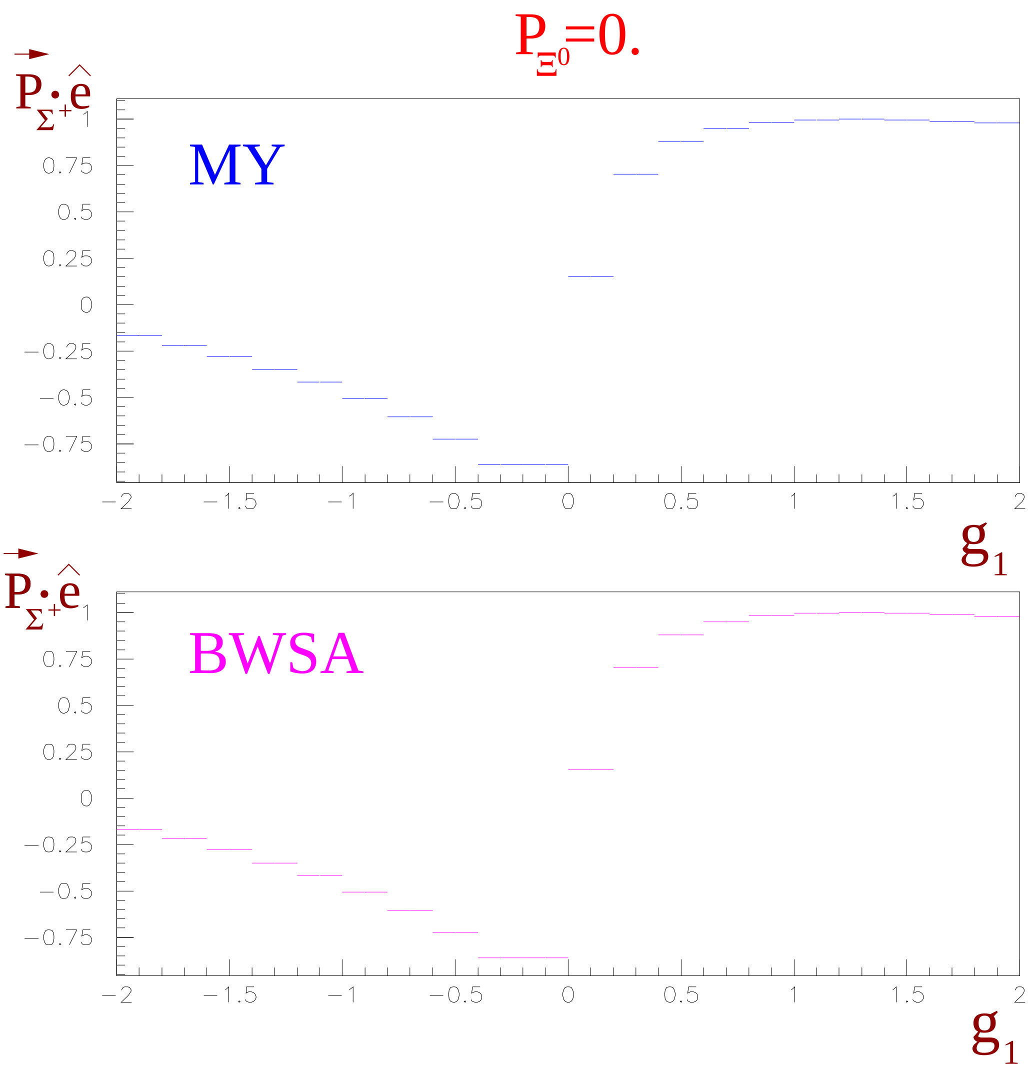

Figure 4.9: The first plot shows the Σ^+ polarization along electron direction from my generator, the second one shows the Σ^+ polarization along electron direction coming from [27] (BWSA indicates the initials of authors' name).

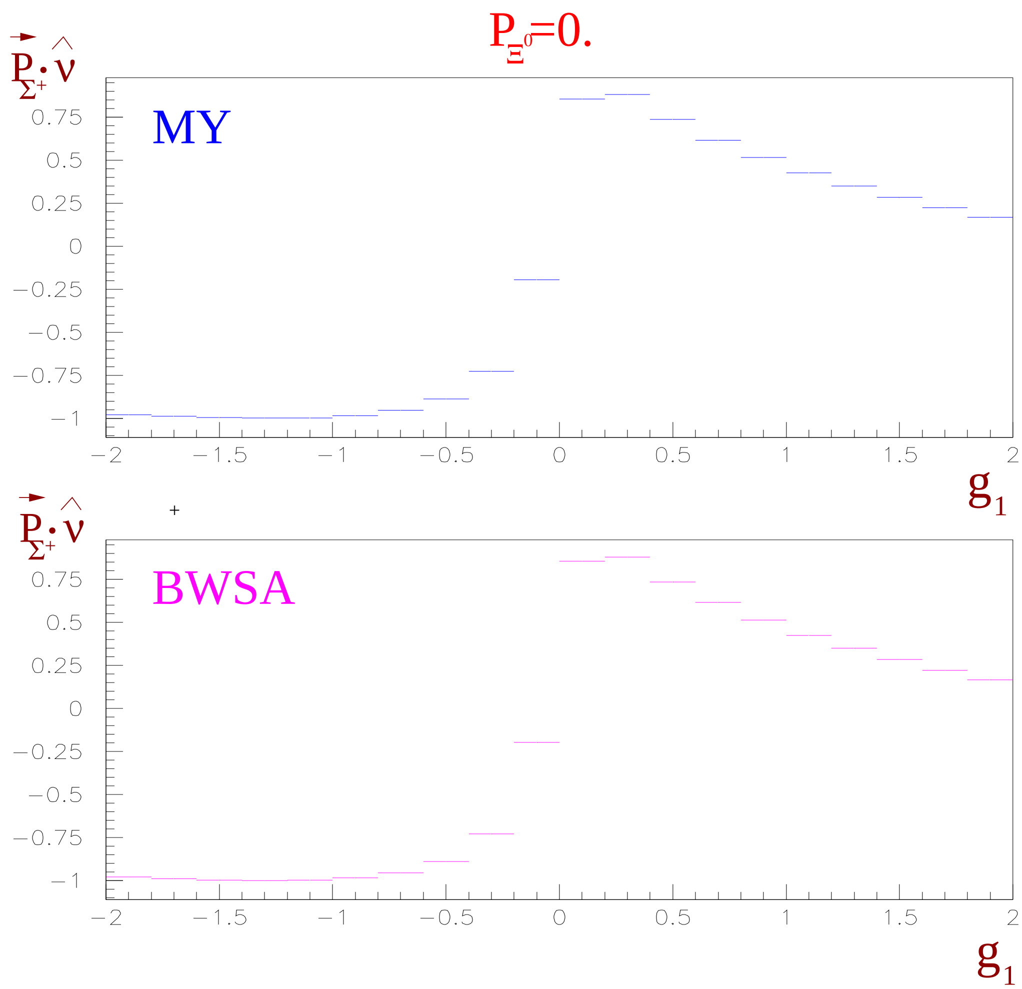

Figure 4.10: The first plot shows the Σ^+ polarization along anti-neutrino direction from my generator, the second one shows the Σ^+ polarization along anti-neutrino direction coming from [27].

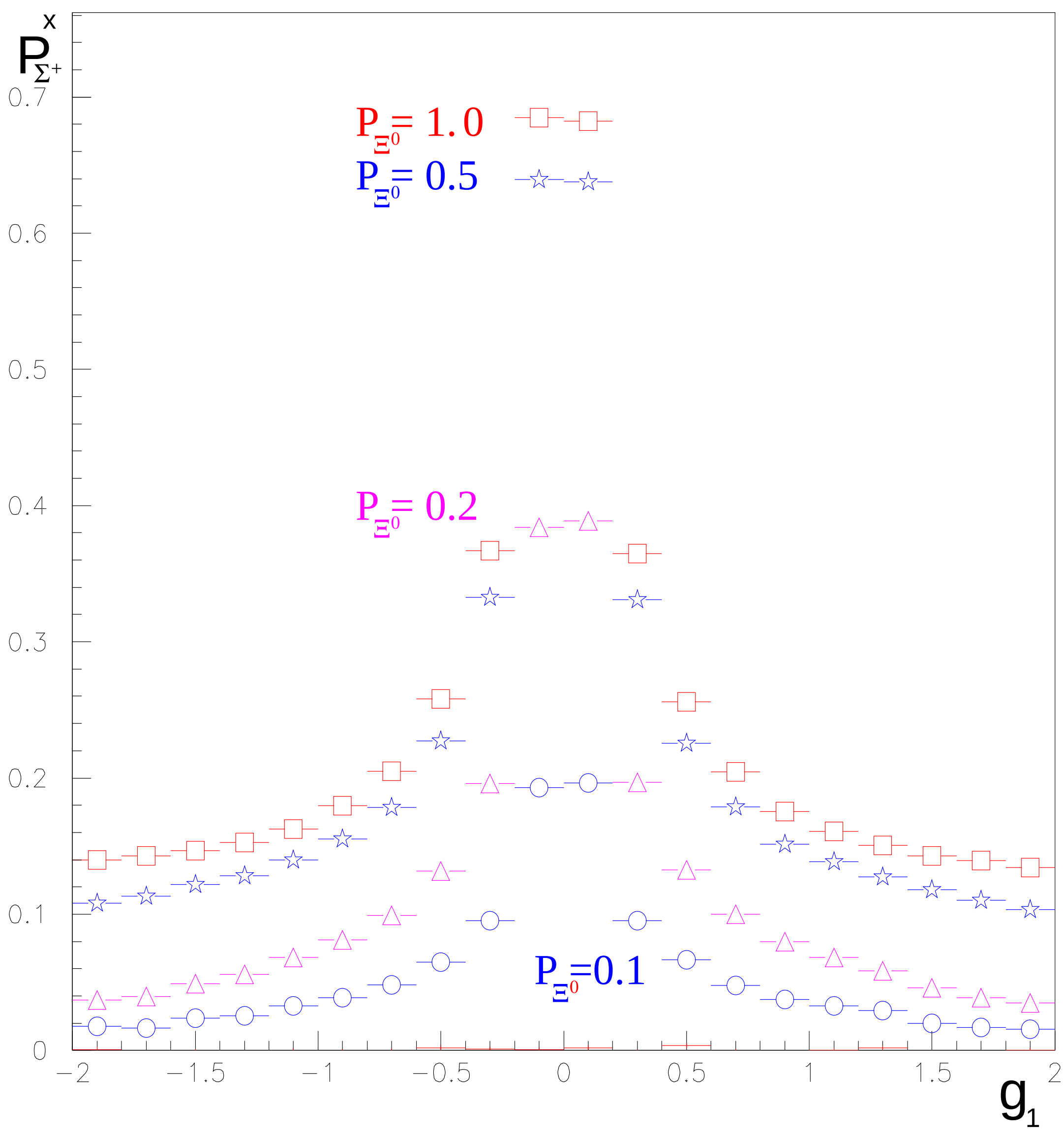

Figure 4.11: Σ^+ polarization along x direction from my generator, different symbols correspond to different polarization of the decaying Ξ^0 hyperon along x.

No quantitative checks were possible for the case of a non-zero Ξ^0 polarization along a fixed x axis in its own rest frame, for which the full expression 1.26 is needed. Here there is an extra privileged direction. Then again for the angular momentum conservation qualitatively one would expect an increase of the Σ^+ polarization along this direction. In fig 4.11 we can see how the Σ^+ polarization along x indeed grows increasing the Ξ^0 polarization along the same axis.

4.5 Data-MC comparison

The acceptance estimations are founded on the reliability of our Monte-Carlo simulation. In the fig. from 4.12 to 4.14 I show the results of the comparison between real data and simulated events after the implementation on the standard NA48 Monte-Carlo of the appropriate generators for all the decays involved in the measurement of Ξ^0 beta decay branching ratio.

The events entering those histograms are selected by the analysis cuts that I will describe in detail on the next chapter. For the Ξ^0 semileptonic decay, after the correction of the generator of the Ξ^0 spectrum and after the correction of the target position, this comparison still shows some differences in the Σ^+, proton and electron spectra (see fig. 4.12). The reason of this discrepancy is not fully understood yet. In the next chapter I will show a study concerning one of this aspect. Nevertheless, in order to reduce the effects of this discrepancy, in the final analysis I apply the acceptance correction in bins of Σ^+ energy for the signal events. For the normalization channel the acceptance correction is applied in bins of Ξ^0 energy.

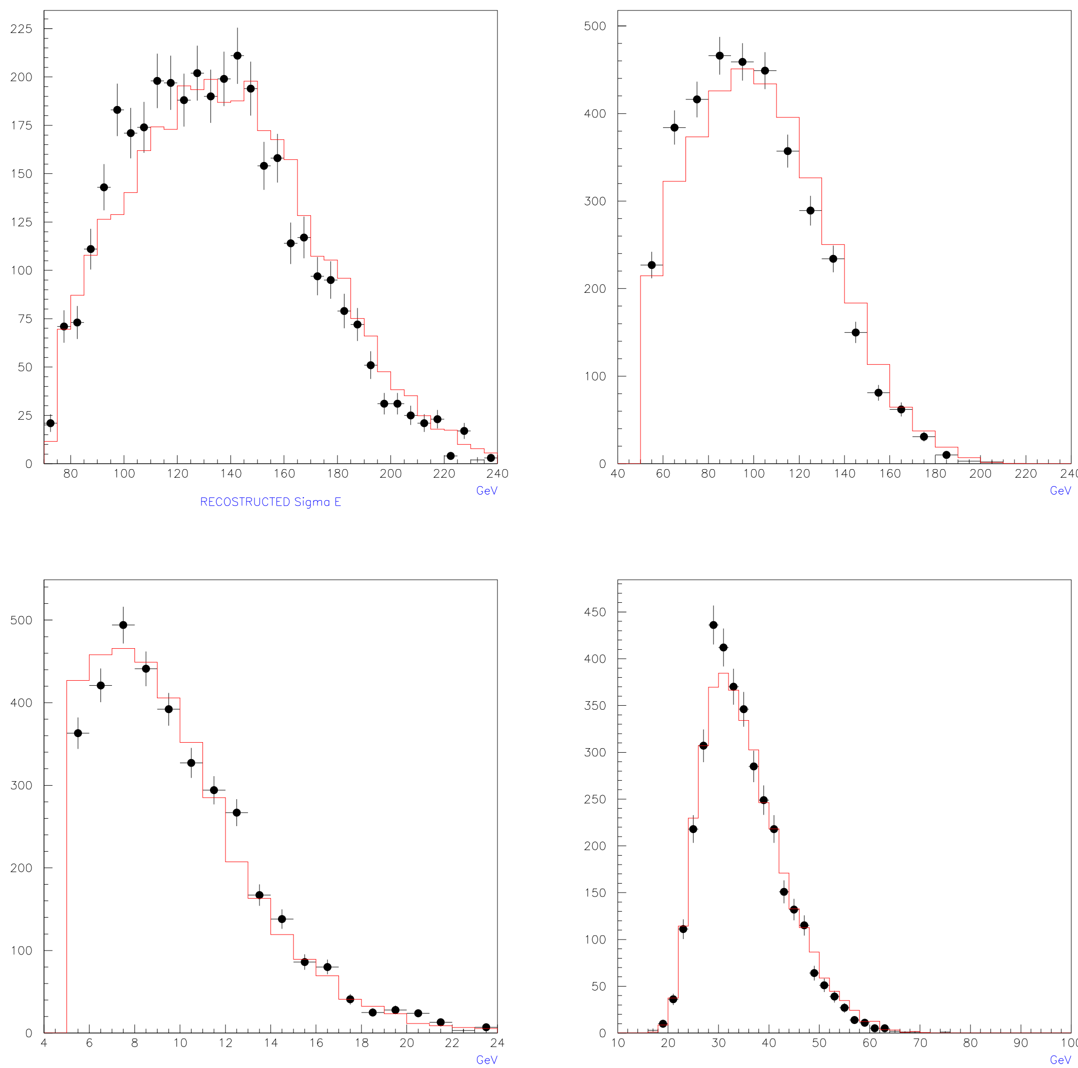

Figure 4.12: Energy Spectra in the laboratory rest frame for the signal channel; in black the real data and in red the MC data. The MC data are generated with a starting Ξ^0 polarization along x axis of - 10%. Going from left to right and from the top to the bottom we have the Σ^+ spectrum, the proton spectrum, the electron spectrum and the π^0 spectrum.

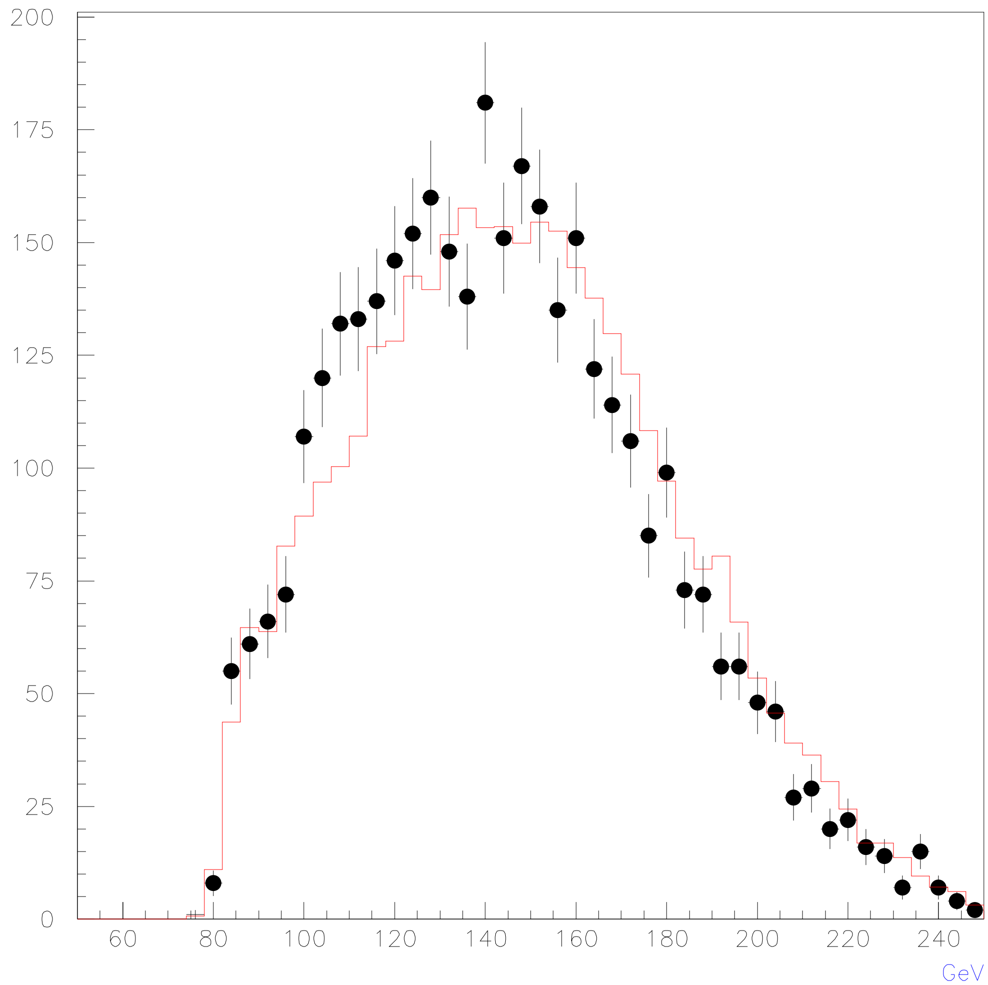

Figure 4.13: Total reconstructed energy on the laboratory rest frame; in black the real data and in red the MC data. The MC data are generated with a starting Ξ^0 polarization along x axis of - 10%

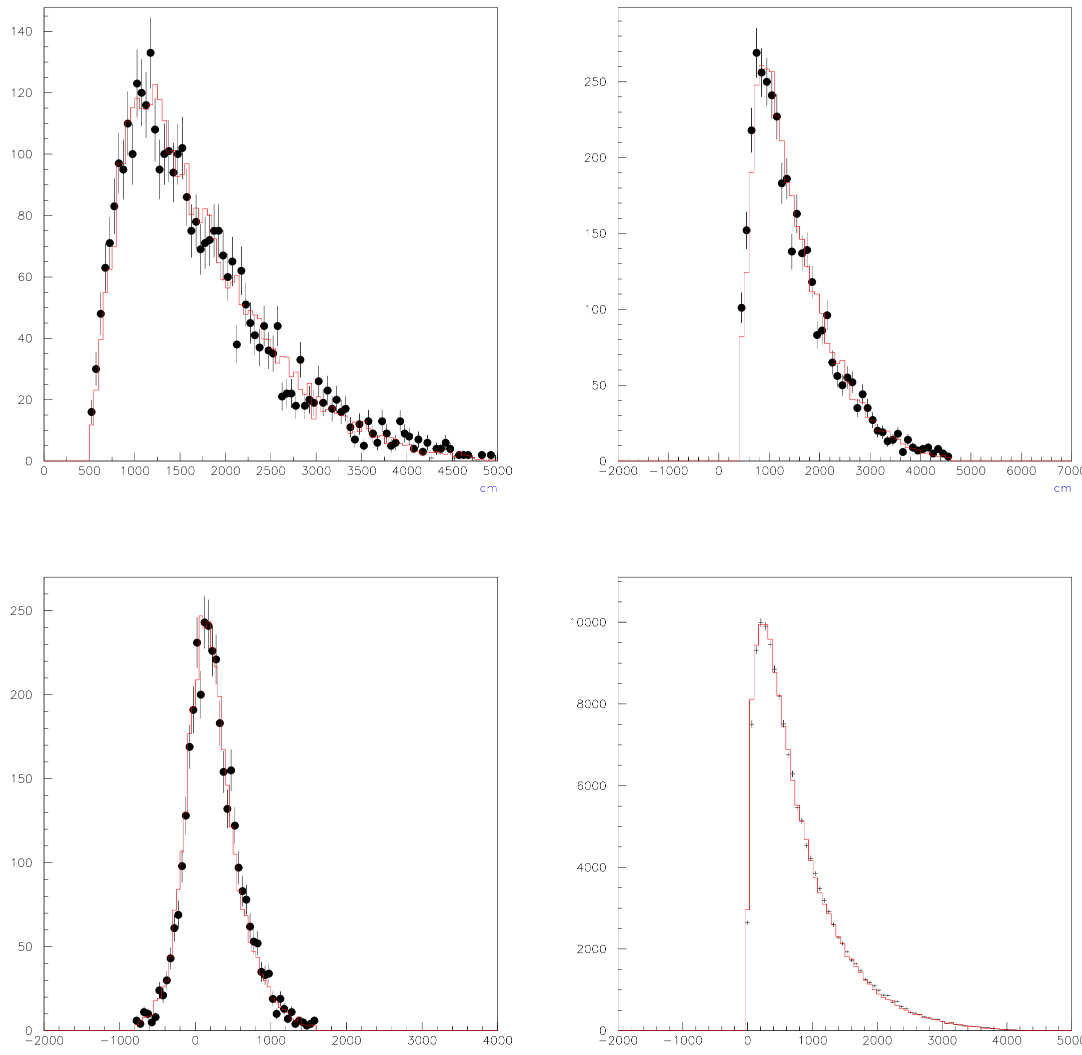

Figure 4.14: The plots show some z distributions for data (black) and for MC (red). On the top-left the z of Σ^+ decay vertex. On the top-right the z of Ξ^0 decay vertex. On the bottom-left the difference between the z of Σ^+ decay vertex and the z of Ξ^0 decay vertex. Finally on bottom-right the difference between the z of Λ decay vertex and the z of Ξ^0 decay vertex for the normalizzation channel. The MC data are generated with a starting Ξ^0 polarization along x axis of - 10%

Chapter 5

Data analysis and results

During 89 days of data taking in 2002 run NA48 has collected more than 300 thousands bursts. From that starting sample approximately 270 thousands burst were classified as “good bursts for physics” and they were reprocessed in the winter between 2002 and 2003 to include the final calibrations of all the sub-detectors and to create the standard data format for the analysis.

I start this chapter explaining the methods we use to reconstruct the events coming from the signal and the normalization channels. Then I will list the cuts applied to select those events, to reduce the background and to optimize the trigger efficiency. After the definition of the final samples I will show the results for the efficiencies measured for all the triggers involved in the data selection.

For the purpose of my analysis the data will be divided in three samples, isolating the initial and the last period where we had large inefficiencies in some component of the trigger[1].

[1]As already explained in the previous chapter I need to perform two different analyses to take into account a different LV1 configuration at the beginning of the run. Moreover during the analysis we found a malfunctioning on the $Q1$ request of LV1 trigger at the end of 2002 run. That problem affected both the trigger and the read-out of the charged hodoscope in such a way that the problem is not detected in the measurement of the trigger efficiency (the offending events are rejected both from the trigger and from our offline analysis). The effect, however, is present also for the normalization channel and cancels in the branching ratio.

From that point I start to show the different results for the three periods in which the analysis is divided.

Going on I show the results obtained with our Monte-Carlo on the acceptances of the signal and normalization channels.

Finally, after the study performed to understand the residual background in the signal sample, I present the preliminary results on the branching ratio measurement of Ξ^0 beta decay.

5.1 Reconstruction of $\Xi^0 \to \Sigma^+ e^- \bar{\nu}_e$

To reconstruct a signal event we need at least two detected tracks from DCHs and three clusters in the LKr. Two of these clusters are necessary to identify the pion decayed into two photons, the last one has to be associated to a negative track to identify the electron absorbed in the LKr. In the reconstruction algorithm first I search for a positive track compatible with the presence of a proton. After the proton identification I look for two well-separated clusters and, imposing the π^0 mass constraint, I use the following relation to find the longitudinal position of the Σ^+ decay vertex, where the π^0 originates:

$$z_{\pi^0} = \frac{1}{m_{\pi^0}} \sqrt{E_1 E_2 [(x_1 - x_2)^2 + (y_1 - y_2)^2]} \qquad (5.1)$$

where E_1 and E_2 are the energies of the two clusters respectively, (x_1, y_1) and (x_2, y_2) the positions of those clusters in the LKr.

Then at that z I take the x and y of the proton track to fix in this way the Σ^+ decay vertex.

Knowing the position of the Σ^+ (and π^0) vertex now I can determine completely the π^0 momentum. Since I already know the proton momentum measured from the spectrometer I can extract both the mass and the momentum of Σ^+ . Moreover I use the momentum found in this way to track back the Σ^+ and I look for the closest distance of approach (CDA) between that direction and the direction of a negative track compatible with the electron. The average point of the segment corresponding to this CDA is identified as the Ξ^0 primary decay vertex.

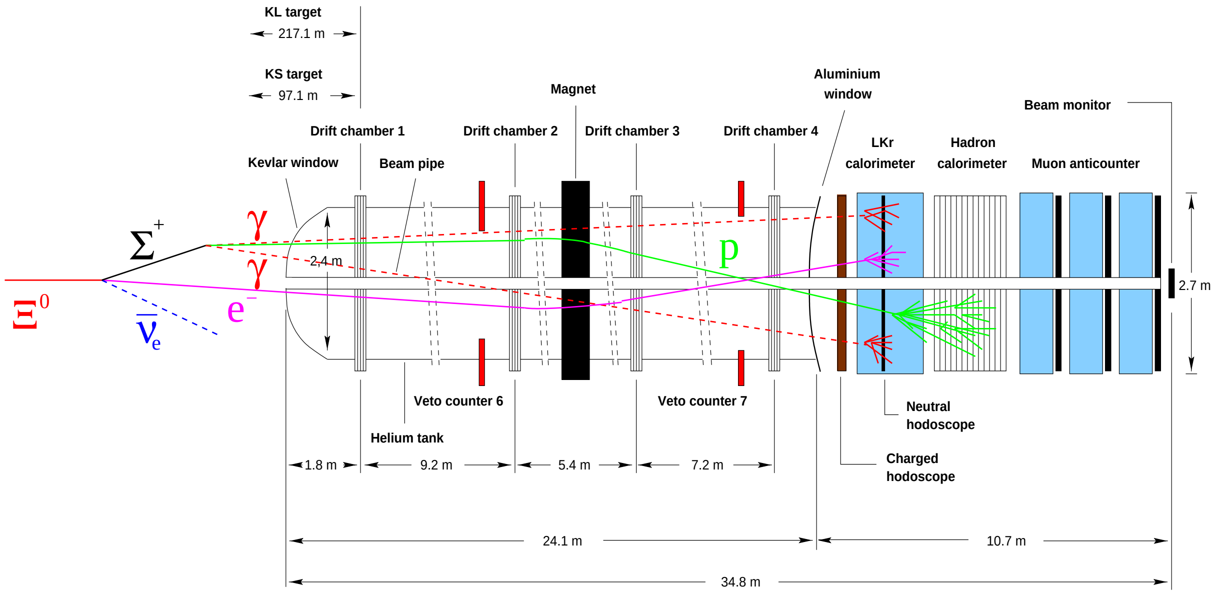

Figure 5.1: Sketch of a Ξ^0 beta decay superimposed to the NA48 detector. The red lines are the gammas producing two clusters in the LKr, the green line is the proton direction and the magenta one the electron direction. The plot is not to scale.

Now we have the Ξ^0 decay vertex, but, due to the missing neutrino energy, we can't reconstruct the Ξ^0 momentum and its mass. Nevertheless we will see that the availability of the (p, π^0) invariant mass allows us to fix a well defined signal region. In fact the Σ^+ mass peak is a clear signature of the Ξ^0 beta decay. Another tool for background reduction is the electron identification provided by the comparison of the energy E measured in the LKr calorimeter with the momentum p measured in the spectrometer. The ratio is expected to be near 1 for electrons which are completely absorbed in the LKr. On the other hand protons and charged pions typically reach the hadron calorimeter, and give E/p lower than 1.

5.2 Signal selection

The aim of the selection is to have a signal sample as clear as possible from background and with a good trigger efficiency since, as shown later, the measurement of trigger efficiency is a non negligible contribution to the error. In order to clean the signal the main background sources were studied and some of our cuts reflect this work. The good trigger efficiency was persecuted with safe cuts on the geometrical acceptance of detector and on the variables used in the LV2 trigger. In order to achieve these goals, we choose cuts that sacrifice some efficiency. A different choice would have been possible for the branching ratio measurement, which is the subject of this thesis. However in this way we obtain a sample that can be used also for a future study of the form factors, without the need of corrections which depend on the event kinematics and would be hard to estimate.

The selection criteria can be classified according to their aim in the following way:

1) Cuts to improve trigger efficiency

2) Cuts for proton selection.

3) Cuts for LKr clusters selection and π^0 reconstruction.

4) Cuts on reconstructed Σ^+

5) Cuts for electron selection

6) Cuts on reconstructed primary vertex

7) Cuts to clean the signal and to reject in-time extra-activity

5.2.1 Trigger efficiency cuts

LV2 trigger applies conditions based on a simplified event reconstruction. LV3 uses the same reconstruction algorithms as the offline reconstruction, but with preliminary calibration constants and therefore with a worse resolution. In order to keep

under control the final trigger efficiency we have to apply similar but tighter cuts on the same variables. The following cuts are applied for this reason and, taking into account the better offline resolution on all the measured quantities, they also are useful to reduce the background:
- No "overflows" in the DCHs read-out and in the MBX. Although the DCH read-out electronics can record up to 63 hits/plane, only 8 hits are sent to the MBX trigger system. In a class of events with abnormally high activity in the drift chambers (mainly due to superposition of the events of interest with high multiplicity accidentals) this creates an extra source of inefficiency. The occurrence of this condition is detected in the reconstruction program and flagged. Requiring the absence of this flag will increase the LV2 trigger efficiency of $\sim 4\%$, producing at the same time an acceptable loss in the statistics. Fig. 5.2 shows the distribution of the number of plane with an overflow, before applying the cut, for the LV2 efficient events and for the LV2 inefficient events found in a control sample collected without the LV2 condition (see chapter 3).

The statistics is low but nevertheless it is clear that the fraction of events with MBX overflow in the inefficient sample is bigger than the same fraction in the efficient sample.
- Distance between electron and proton at $DCH1$ greater than 8 cm. Here we apply a tighter cut with respect to the LV2 cut. In fig. 5.2 is shown the distribution of this distance for electron-proton candidates. The small fraction of events for which this distance is exactly equal to 0 is due to cases where the reconstruction program uses the same hit to reconstruct two different tracks.
- No vertex satisfying the request $(\frac{p_{bigger}}{p_{smaller}} < 7 \cdot |m(\pi,\pi) - m_{K^0}^{PDG}| < 0.035\ GeV/c^2$ (kaon rejection). Explicitly for each vertex I ask that, if the momentum ratio between the track with bigger momentum and the track with lower momentum is less than 7, then the invariant mass of the vertex, computed using the pion mass for the two tracks, has to be far from the K^0 mass.
- No vertex satisfying the request $|m(p,\pi) - m_{\Lambda}^{PDG}| < 0.014 GeV/c^2$ (Λ and $\overline{\Lambda}$ rejection); fig. 5.3 shows the distribution of proton-pion invariant mass from the events

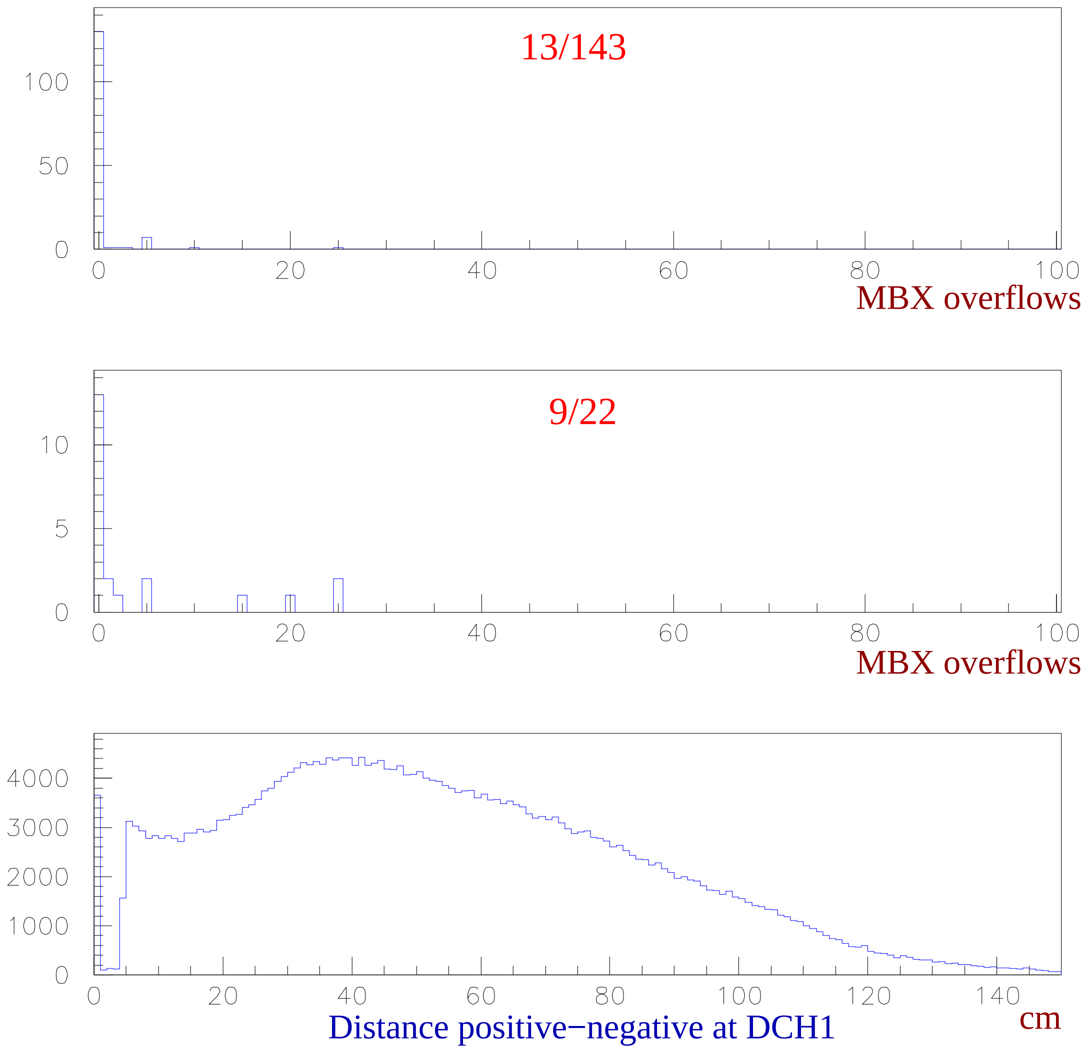

Figure 5.2: Distribution of the MBX overflow flag for $LV2$ efficient (top) and inefficient (center) events. The flag is defined as $N_1 + 5N_2 + 25N_4$ with N_1, N_2, N_4 equal to the number of views with an overflow in chambers 1,2 and 4 respectively. The bottom plot shows the distance between electron-proton candidates at the first DCH.

coming from the LV2 trigger. The depletion around the Λ mass is due to the MBX cut, but the plot shows that some Λs survive this cut (effect of low MBX resolution and of MBX inefficiencies). In order to reject these Λs and maximize the LV2 trigger efficiency I again apply a tighter cut.
- Closest distance of approach between proton and electron lower than 4 cm.
- Momentum ratio between proton and electron greater than 5.

5.2.2 Proton selection

- At least one track reconstructed from DCHs, with positive charge and with momentum bigger than 50 GeV/c. If we have more than 1 positive track I select the one with the biggest momentum.
- E/p of the track lower than 0.8.
- Distance of the track from beam pipe axis at $DCH1$, $DCH2$, $DCH4$ and at LKr greater than 12 cm and lower than 110 cm.

5.2.3 π^0 identification

I require two clusters in the LKr satisfying the following conditions:
- Energy greater than 4 GeV.
- Distance from the beam pipe axis greater than 15 cm and lower than 110 cm (clusters inside the geometrical acceptance of LKr).
- Distance from LKr dead cells greater than 2.5 cm.
- Distance from the reconstructed impact point of proton at the LKr greater than 20 cm.

For the two clusters so selected I further require:
- Distance between the two clusters greater than 10 cm.
- Time difference between the two clusters less than 3 ns using the time measured in the LKr (see fig. 5.10).
- z position of the decay vertex of π^0, computed with formula 5.1, between 6 and 50 m from K_S^0 target.

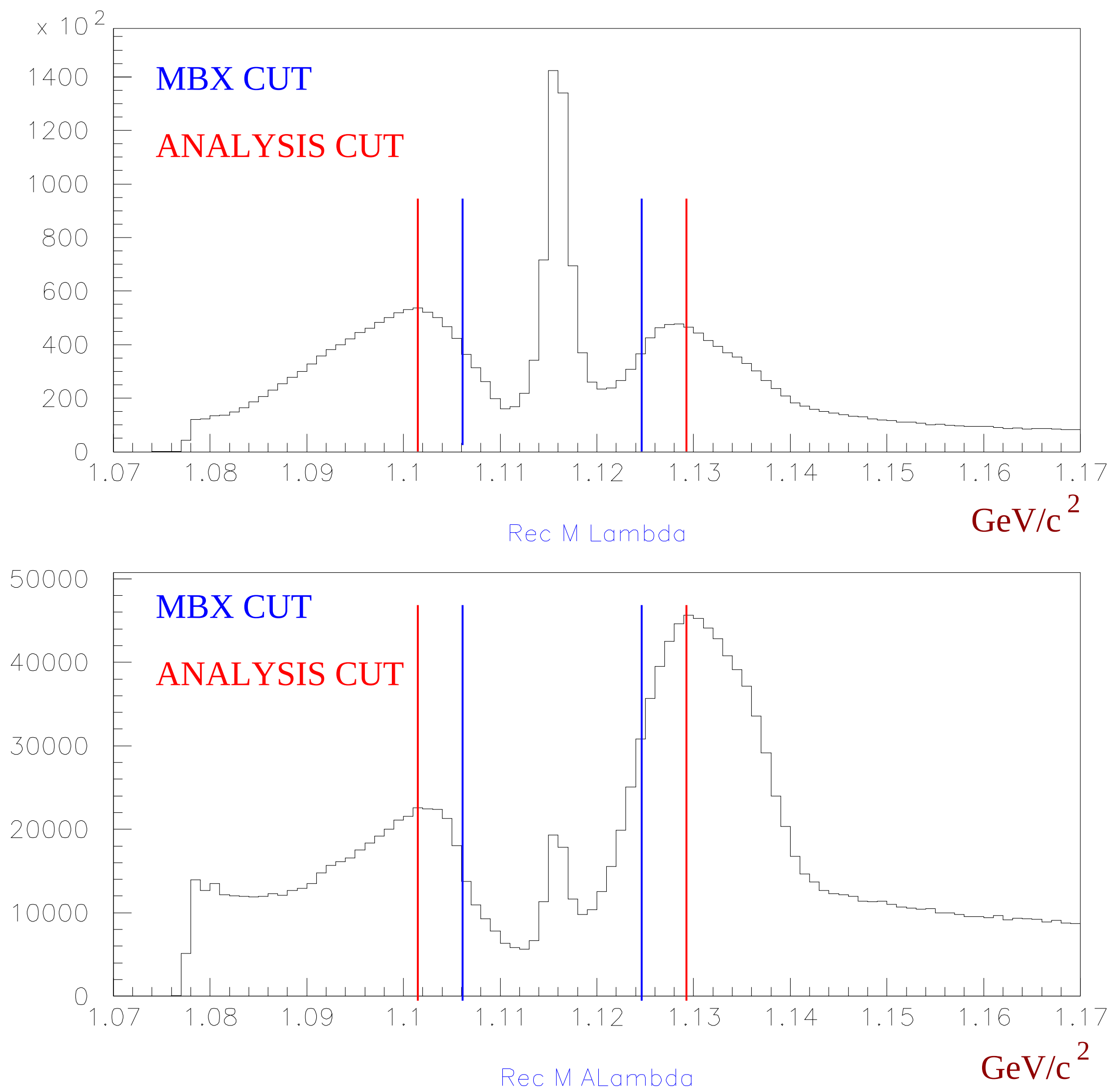

Figure 5.3: The plot on the top shows the proton-π^- invariant mass for our initial sample. The effect of LV2 cut for Λ rejection is clearly visible. The plot on the bottom shows the anti-proton-π^+ invariant mass. Also in this case we see the effect of the LV2 cut for anti-Λ rejection. The blue lines correspond to the LV2 cuts, the red lines to the analysis cuts.

5.2.4 Cuts on reconstructed Σ^+

After the proton and pion identification, as already explained, we can reconstruct the Σ^+ decay vertex and its momentum. The cuts applied are the following:
- Time difference between the π^0 (considering the average time of the two clusters) and the proton (time from charged hodoscope) lower than 3 ns (see again fig. 5.10).
- z of Σ^+ decay vertex between 5 and 50 m from K_S^0 target.
- Σ^+ energy greater than 70 GeV and lower than 240 GeV.

5.2.5 Electron selection

The cuts applied on the candidate track are the following:
- Track with negative charge and momentum greater than 5 GeV/c.
- Distance of the track from beam pipe axis at $DCH1$, $DCH2$, $DCH4$ and at LKr greater than 12 cm and lower than 110 cm.
- E/p of the track greater than 0.9; for the events coming from LV2 I show in fig. 5.4 the E/p distribution. The electron peak at 1 is already clear.
- Time difference between the proton track and the electron one lower than 3 ns using the time measured in the charged hodoscope (see fig. 5.10).
- No hits shared between proton and electron tracks at $DCH4$.

5.2.6 Primary vertex cut

At this point we have a fully reconstructed event. The following cuts are applied on the reconstructed primary vertex to reduce the background:
- closest distance of approach between the electron direction and the Σ^+ direction lower than 5 cm.
- z of the primary vertex between 4 and 46 meter from K_S^0 target.
- x of primary vertex between -2.5 and 2.5 cm.
- y of primary vertex between 2 and 11 cm.
- $-8\ m \leq z_{\Sigma^+} - z_{\Xi^0} \leq 16\ m$
- Invariant mass of Σ^+ and electron lower than Ξ^0 mass

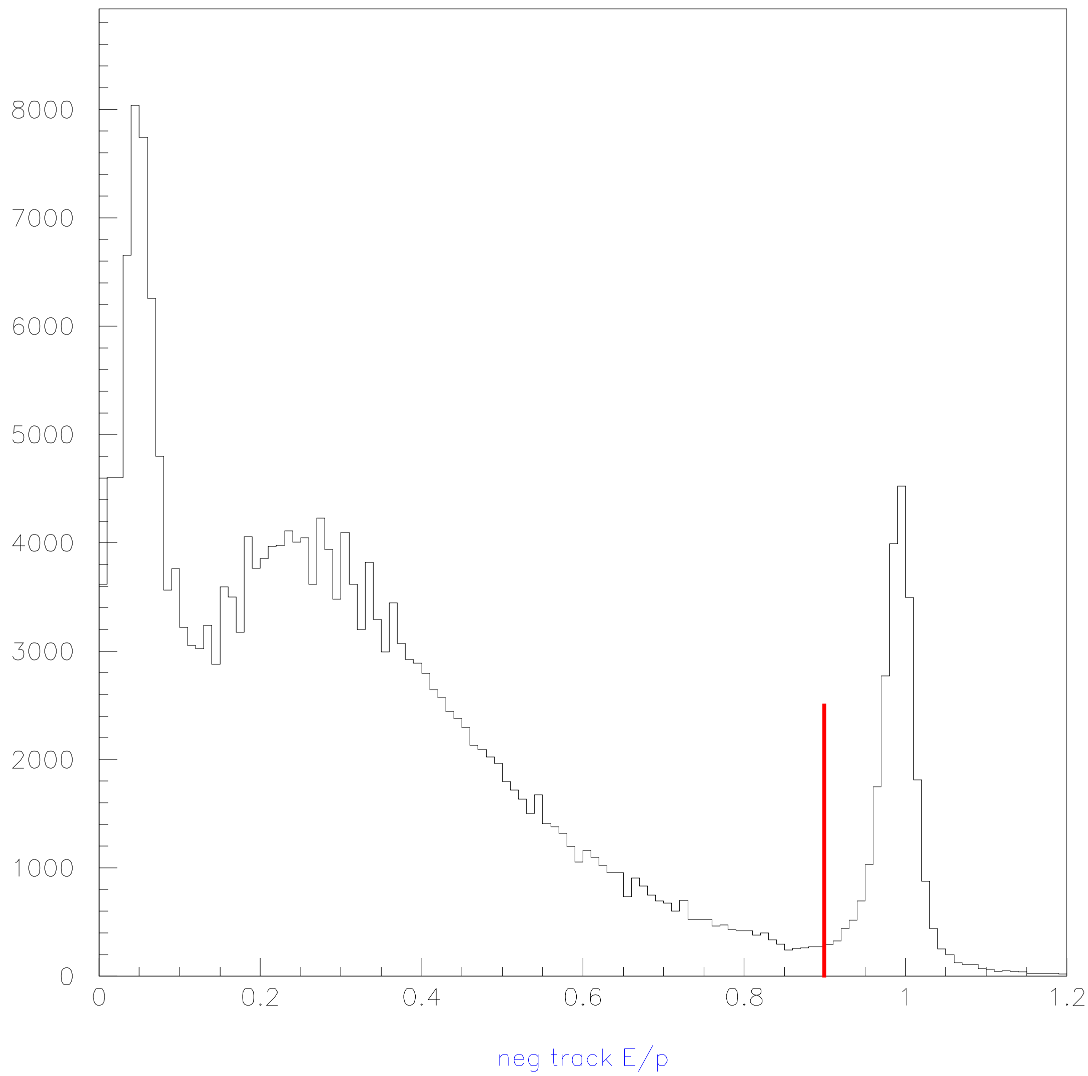

Figure 5.4: E/p for negative tracks (electron candidates). The line in red shows the analysis cut.

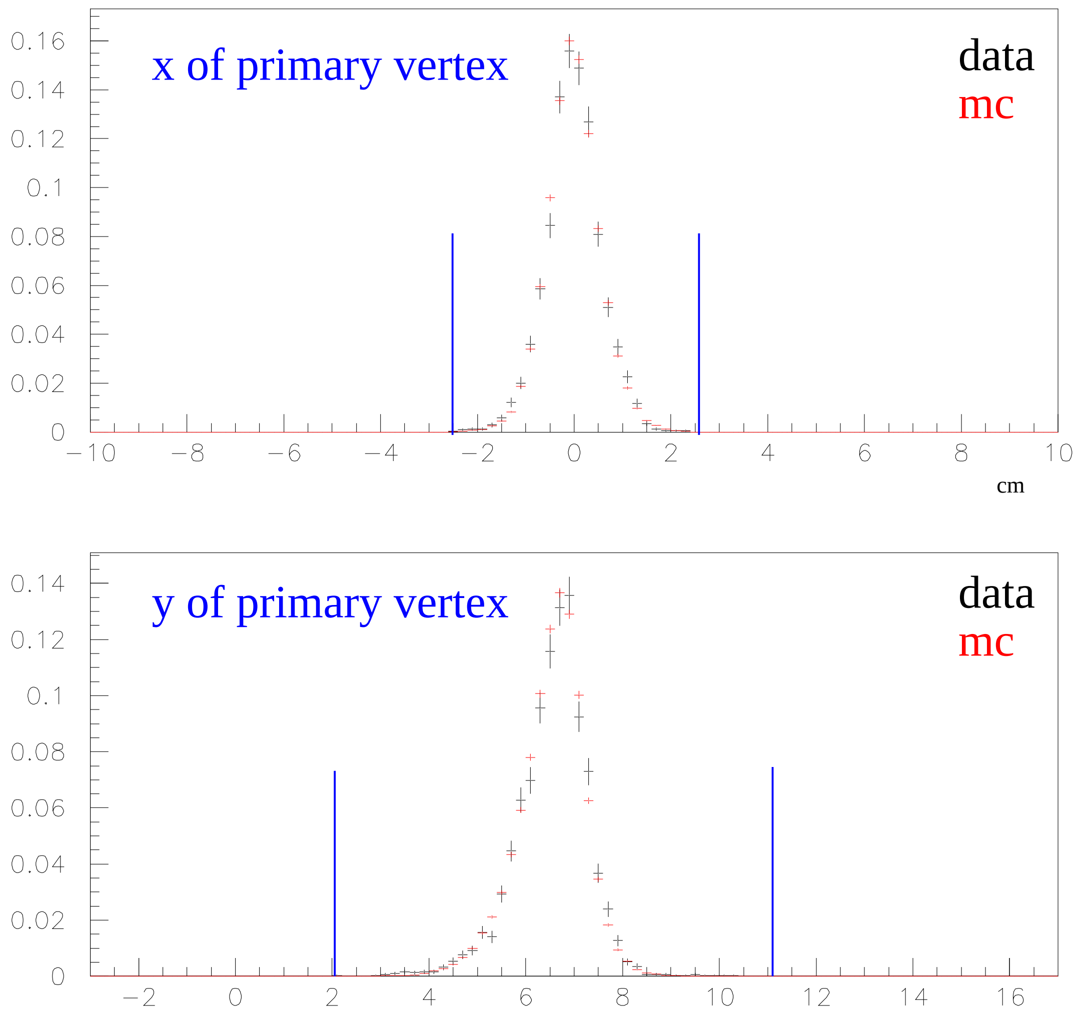

Figure 5.5: x and y distributions for the Ξ^0 decay vertex. The blue lines define the analysis cuts.

- Measured transverse momentum with respect to the beam axis less than 0.11 GeV/c.

These cuts have been designed, on the basis of the Monte-Carlo simulation of Ξ^0 semileptonic events in such a way that they have full efficiency for these events. Histograms for some of these quantities are presented in figures 5.5, 5.6.

Fig. 5.6 shows the transverse momentum distribution for data and for MC. Fig. 5.5 shows the x and y of Ξ^0 vertex after the selection for real data (black) and MC data (red).

5.2.7 Cleaning cuts

The last cut we apply is to avoid the presence of extra-clusters with energy greater than 3 GeV, and extra-tracks with momentum greater than 3 GeV/c, in time with the two tracks and the two clusters identifying the signal event. We avoid extra activity in a window from -20 and 20 ns centered in the event time. The event time is defined averaging the time of the two clusters and the time of the two tracks. The motivation for using a wide time window will be discussed in section 5.8.

At the end of the selection procedure, 10514 events are left. As shown in fig. 5.7 they show a rather clean Σ^+ mass peak. In the following, I will consider signal candidates the events in the mass range $m_{\Sigma^+_{PDG}} - 8\ MeV/c^2 < m(p, \pi^0) < m_{\Sigma^+_{PDG}} + 8\ MeV/c^2$.

5.3 Reconstruction of the normalization channel

In the normalization channel $\Xi^0 \to \Lambda\pi^0$ we can fully reconstruct the decay, since all the produced particles are detected and all the energy is measured. Again we start from the final products of the decay and we go back first searching for the Λ and then for the Ξ^0. The Λ decay vertex is found looking at the closest distance of approach between proton track and π^- track. We know the momenta of the two charged particles and then we can also reconstruct the Λ momentum. To find

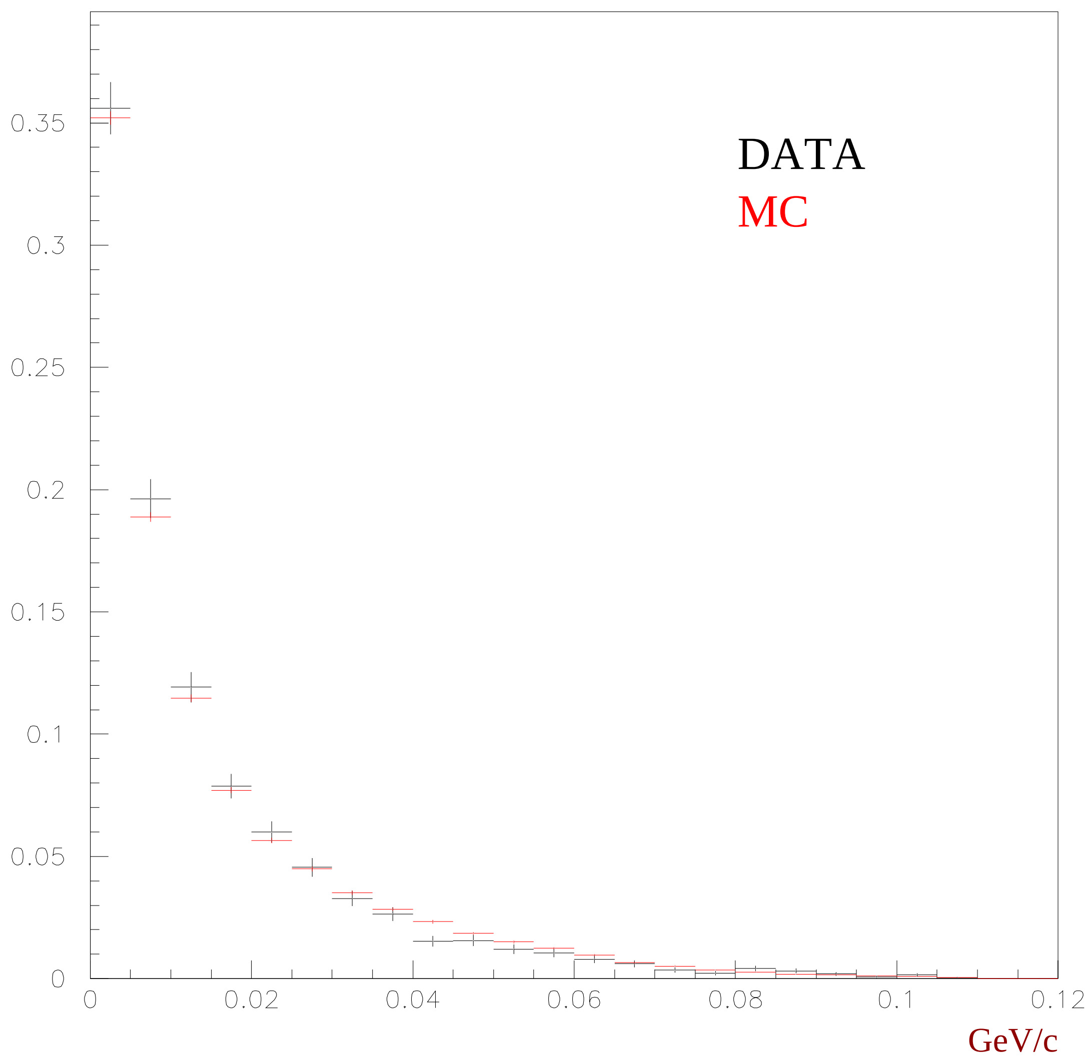

Figure 5.6: Transverse momentum of the event for data and Monte-Carlo.

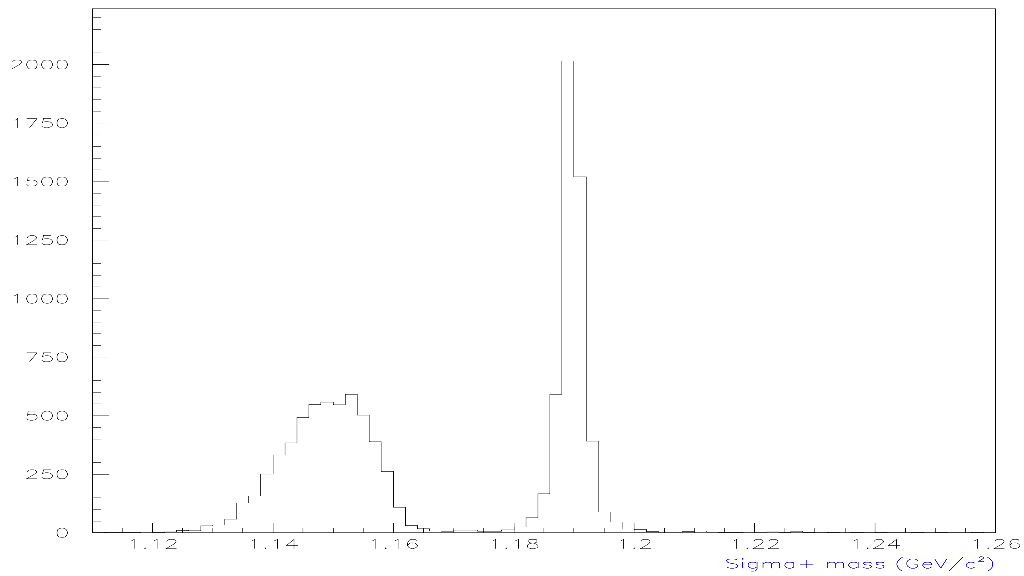

Figure 5.7: 2002 data: Final sample in the $\Xi^0 \to \Sigma^+ e^- \bar{\nu}_e$ channel after the selection.

the primary vertex one possibility is to search for the closest distance of approach between the Λ direction and the beam axis. However I prefer to apply the same method used for the signal and, with the two most energetic clusters (not associated to a track), I use equation 5.1 to find the z of the Ξ^0 decay vertex where the π^0 originates. At this z I take the x and y of the Λ trajectory extrapolated backwards from its decay vertex. Now again we can fully reconstruct the Ξ^0 momentum and its mass because we know both the π^0 and the Λ momentum.

In the normalization channel we have two mass spectra that can be used to identify the decay. First we can look at the invariant mass between proton and pion to search for the Λ peak and then we can also look to the invariant mass between Λ and π^0 searching for the Ξ^0 peak. At the end the normalization channel is well constrained and then we will see that the final background to this decay is negligible.

5.4 Selection of $\Xi^0 \to \Lambda\pi^0$ events

The events of the Ξ^0 channel, used for normalization, are collected using the "minimum bias" LV1 trigger discussed in chapter 3. This trigger does not use track reconstruction and is very efficient. Therefore in the offline analysis we don't need to apply specific cuts in order to improve the trigger efficiency. Event identification cannot follow the same line used for the signal channel because the event has a different topology and has no missing energy. The decay of the Λ, coming from a vertex detached from the completely neutral Ξ^0 vertex is fully reconstructed from the spectrometer and it is the main and clear signature of the decay. Since we don't have missing energy we can also fully reconstruct all the quantities related to the Ξ^0 decay. For all other cuts I try to use conditions as close as possible to the ones used for the signal channel. This is true, for example, for the cuts that define the detector acceptance. It is particularly important to apply exactly the same cuts for those conditions which cannot be simulated in the Monte-Carlo, like, e.g., those on the presence of accidental activity. In this way one can avoid to correct for the inefficiency of these cuts which cancel in the branching ratio measurement.

Now I start to describe the applied selection, and again I group the cuts taking into account their different aims.

5.4.1 Λ identification

Here I prefer to directly select the best charged vertex instead of selecting the positive and the negative track separately:

- No overflows from DCHs read-out and from the MBX.
- At least one charged vertex with a closest distance of approach between the two tracks lower than 2 cm.
- z of the vertex between 6 and 50 m from the K_S^0 target.
- Distance between the two tracks at $DCH1$ greater than 8 cm.
- Momentum of the positive track greater than 40 GeV/c.
- Momentum of the negative track greater than 7 GeV/c.

- E/p for both tracks lower than 0.8.
- Momentum ratio between the positive and the negative track greater than 5.
- Defining the center of gravity at $DCH1$ of the two tracks in the following way:

$$COG = \sqrt{\frac{(x_P p_P + x_N p_N)^2}{(p_P + p_N)^2} + \frac{(y_P p_P + y_N p_N)^2}{(p_P + p_N)^2}} \tag{5.2}$$

where P and N indexes identify the positive and the negative track respectively, I ask for a COG greater than 5 cm; this cut is applied to reject the Λ coming directly from the target.
- Distance of the two tracks from beam pipe axis at $DCH1$, $DCH2$, $DCH4$ and at LKr greater than 12 cm and lower than 110 cm.
- Time difference between the two tracks less than 3 ns.
- $|M_V(\pi,\pi) - m_{K^0}^{PDG}| > 0.030 GeV/c^2$ (kaon rejection).
- Finally I explicitly ask that the invariant mass of the vertex, supposing the two tracks to be a proton and a pion, has to be consistent with the Λ mass: $|m(p,\pi) - m_{\Lambda}^{PDG}| < 0.010 GeV/c^2$; Fig. 5.8 shows the invariant mass (p-π^-) for data and MC.
- If at the end of this selection we have more than one good Λ vertex, we take the one with the higher momentum for the positive track.

5.4.2 π^0 identification

I require two clusters in the LKr satisfying the following conditions:
- energy greater than 3 GeV.
- Distance from LKr dead cells greater than 2.5 cm.
- Distance from the beam pipe axis greater. than 15 cm and lower than 110 cm (clusters inside the geometrical acceptance of LKr).
- Distance from the reconstructed impact points of proton and π^- at the LKr greater than 20 cm.

For the two clusters so selected I require:
- Distance between the two clusters greater than 10 cm.
- Time difference between the two clusters less than 3 ns.
- z position of the decay vertex of π^0 between 6 and 50 m from K_S^0 target.

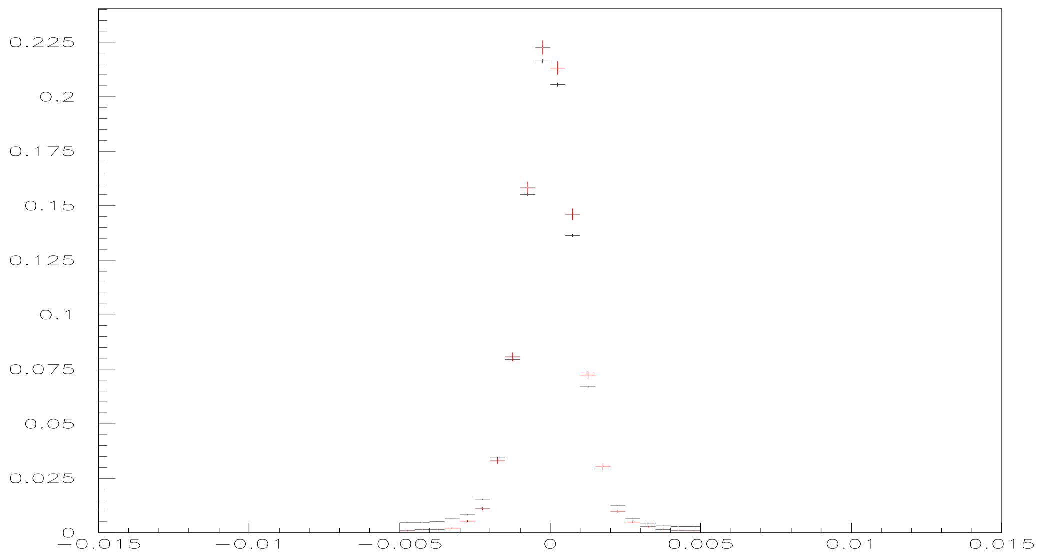

Figure 5.8: Difference between the reconstructed Λ mass and its PDG value. I superimpose the same distribution from MC (red).

5.4.3 Primary vertex cuts

After the identification of the primary vertex I can fully reconstruct the decay kinematics and I apply the following cuts to improve the background rejection:
-x of Ξ^0 decay vertex less than 1.5 cm in absolute value.
-y of Ξ^0 decay vertex greater than 4 cm and less than 8 cm.
- $z_\Lambda - z_{\Xi^0}$ greater than 0.
- Ξ^0 energy greater than 80 GeV and less than 250 GeV.
- transverse momentum along x axis less than 0.1 GeV/c in absolute value.
- transverse momentum along y axis greater than -0.2 GeV/c and less than 0 GeV/c.
- time difference between the two tracks and the two clusters less than 4 ns.

Again we avoid extra activity in a window from -20 and 20 ns centered in the event time. We will see that the background coming from accidental activity is quite small, but we need to apply this cut in order to not introduce a bias with respect to the signal selection.

There is still another cut to apply to symmetrize the efficiencies of the signal and normalization channels. The signal channel is collected through the MBX trigger and therefore is subject to a non negligible deadtime, which occurs when all the processors are busy and the event cannot be read from the ring buffers. When this happens the MBX system inhibits the LV1 trigger at the input of the MBX. For the normalization channel I'm only taking events coming from the downscaled LV1, which is not subject to the MBX's dead time. However the input to the MBX is recorded in the data and I can avoid the introduction of a bias between the signal and the normalization by demanding that the events coming from the downscaled LV1 also generate an input to the MBX. This request discards $\sim 2\%$ of the previously selected events. After all selection cuts 220984 events $\Xi^0 \to \Lambda\pi^0$ remain. Figure 5.9 shows the $\Lambda\pi^0$ mass plot for the final sample. The good events will be identified by a mass cut $m_{\Xi^0}^{PDG} - 7\ MeV/c^2 < m(\Lambda, \pi^0) < m_{\Xi^0}^{PDG} + 7\ MeV/c^2$.

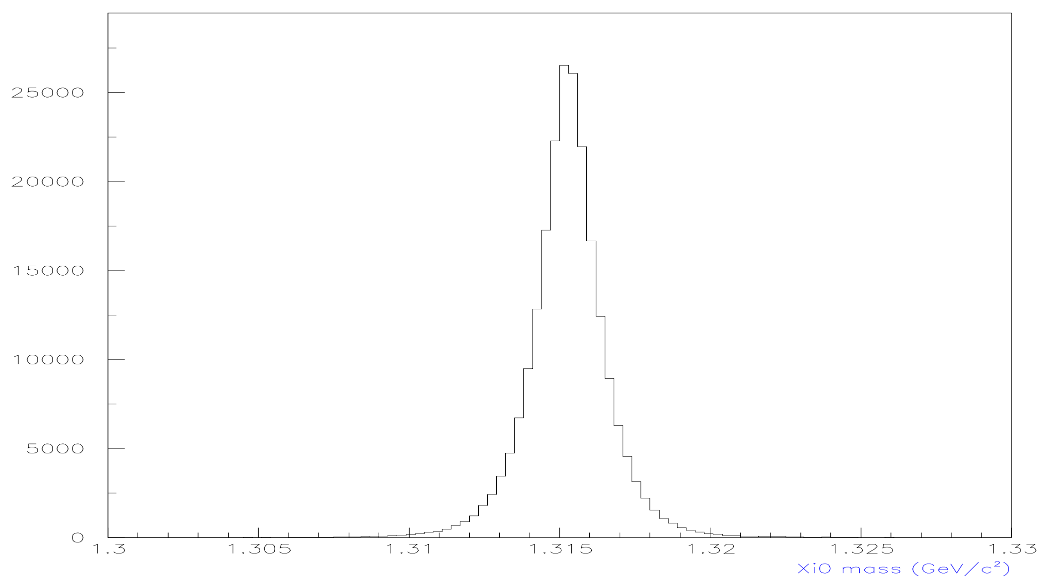

Figure 5.9: 2002 data: Final sample in the $\Xi^0 \to \Lambda\pi^0$ channel after the selection.

5.5 Trigger efficiencies

Trigger efficiency for events passing the final sets of cuts are measured using control samples collected with dowscaled triggers. I discuss this separately for the signal and the normalization channel.

5.5.1 Trigger Efficiency for signal events

The signal events to be collected have to satisfy the requirements of three levels of trigger: the main LV1 charged trigger, the LV2 hyperon beta decay trigger (or the LV2 "short cuts" to this main trigger) and finally the LV3 beta decay filter. Then we need to estimate 3 trigger efficiencies.

For the LV1 efficiency we could use a control sample of events collected with the $T0N$ trigger, based on the information of the neutral hodoscope (see page 45).

The $T0N$ was downscaled by a factor 100, and at the end of my selection I only have 51 events in the control sample and in all of them the LV1 is efficient. So I could only give a lower limit for the trigger efficiency and this limit would not be very stringent.

However, since the LV1 requirements are very loose (it only asks for two tracks and some energy in the calorimeters), and I carefully cut offline in the geometrical acceptance of the detector, one can argue that the LV1 trigger efficiency for the signal channel is the same as for the normalization. In this way the trigger efficiency is only monitored with the normalization channel, with an adequate statistics on the control sample, and I use the assumption that the effects of LV1 trigger efficiency on the BR cancel because we have the same multiplicative factor for the signal and for the normalization channel.

For what concerns the LV2 trigger efficiency in that case I use as control triggers the T0N and then the downscaled subsample of the LV1 trigger that was directly acquired during the run.

The LV2 trigger efficiency measured for the three periods in which I have divided the analysis is the following:

First period : 21/27 $\Rightarrow$ LV2 trigger efficiency=$(77.8 \pm 8.0)\%$

Second period: 148/163 $\Rightarrow$ LV2 trigger efficiency=$(90.8 \pm 2.3)\%$

Third period : 32/41 $\Rightarrow$ LV2 trigger efficiency=$(78.0 \pm 6.5)\%$

Considering the data as a unique sample we obtain the following L2 trigger efficiency:

201/231 $\Rightarrow$ trigger efficiency=$(87.0 \pm 2.2)\%$

Another check I perform for the LV2 trigger efficiency is to calculate it separately for the two different polarities of the spectrometer's magnet.

For this test the different periods cannot be mixed because they contain different fractions of data taken with the different polarities and I use only data from the second period. I find:

B field UP : 79/87 $\Rightarrow$ LV1 trigger efficiency=$(90.8 \pm 3.1)\%$

B field DW: 69/76 $\Rightarrow$ LV1 trigger efficiency=$(90.8 \pm 3.3)\%$

The error on the LV2 trigger efficiency for the signal is one of the main contributions to uncertainty on our final result and probably it will be the main limitation to the precision of NA48 measurement.

Finally for the signal events we measure the LV3 trigger efficiency using as control sample the 2% of data directly acquired without the application of any LV3 filter. The LV3 trigger is a software filter; therefore if we apply the same (or tighter) cuts of that filter in our offline selection, the inefficiency is expected to be small. Using the standard cuts I obtain the following result in the overall data sample:

137/137 $\Rightarrow$ LV3 trigger efficiency$> 98.3\%$ (90% CL)

In order to increase the statistics on the control sample I apply a looser selection by releasing the cuts on Σ^+ mass and the cuts on geometrical acceptance to find a more stringent lower limit. In this way I obtain:

2954/2954 $\Rightarrow$ LV3 trigger efficiency $> 99.92\%$ (90% CL)

The expectation of a high LV3 trigger efficiency is confirmed. The difference from one of the lower limit is quite negligible with respect to the other uncertainties and then I will not apply any asymmetric error on the BR measurement.

5.5.2 Efficiency for the normalization channel

For the decay $\Xi^0 \to \Lambda\pi^0$ we only need to measure the LV1 and the LV3 trigger efficiency because we only use the events coming from the downscaled LV1 trigger.

Again for the LV1 trigger efficiency we use as control sample the events collected by the T0N trigger. This time we have no problem from the size of the statistics sample and I obtain the following results for the three different periods:

First period: LV1 trigger efficiency=$(69.8 \pm 0.5)\%$

Second period: LV1 trigger efficiency=$(99.65 \pm 0.03)\%$

Third period: LV1 trigger efficiency=$(99.68 \pm 0.05)\%$

The results show clearly the effect of the problem in the definition of the two tracks trigger from DCHs in the first period (see section 3.2 where we have an inefficiency of 30 %.

For this inefficiency I will not apply any correction, but only the error will be considered in the systematics, assuming as discussed before, that the LV1 trigger efficiency is the same for the signal and for the normalization channel.

Concerning the LV3 trigger efficiency here I use the same dedicated control sample used for the signal and I obtain the following result (considering all 2002 run):

$6374/6381 \Rightarrow$ LV3 trigger efficiency $= (99.89 \pm 0.04)\%$

We have a small inefficiency coming from 7 inefficient events, but the effect is insignificant with respect to the other sources of error.

5.6 Acceptances

In principle the determination of the acceptance correction requires the knowledge of the polarization of the incoming Ξ^0. In the NA48 collaboration the work to measure that polarization is going on and still we have not even a preliminary result. Considering preliminary results from another experiment with a similar beam geometry[28], the polarization is expected to be along our x axis and negative with respect to the orientation of the same axis. The magnitude of the polarization is expected to be at the level of 10%.

In my studies of the acceptances for the signal and the normalization channels I choose to generate several samples changing the value of Ξ^0 polarization between 0 and -15% along x direction. For each value of Ξ^0 polarization I also produce two different samples, the first with a positive magnet polarity and the second with a negative magnet polarity. I'm referring to the spectrometer's magnet.

Table 5.1 summarizes the results I obtain:

Ξ^0 Polarization along x axis (%)	Magnet polarity	Signal acceptance (%)	Normalization acceptance (%)	Ratio (%)
0.	UP	1.768 ±0.030	0.444±0.004	3.98 ±0.07
0.	DOWN	1.749 ±0.018	0.445±0.003	3.93 ±0.05
-5.	UP	1.735 ±0.017	0.441±0.004	3.93 ±0.05
-5.	DOWN	1.756 ±0.018	0.444±0.004	3.95 ±0.05
-10.	UP	1.754 ±0.021	0.446±0.004	3.93 ±0.06
-10.	DOWN	1.772 ±0.020	0.441±0.004	4.02 ±0.06
-15.	UP	1.737 ±0.019	0.437±0.003	3.97 ±0.05
-15.	DOWN	1.739 ±0.019	0.443±0.003	3.93 ±0.05

Table 5.1: Effect of polarization on the signal acceptance.

This table shows that changing the initial Ξ^0 polarization doesn't affect so significantly the acceptance for both the signal and the normalization channels. In fact the differences between the different values are comparable with the uncertainties on those values coming from the MC statistics. Then we can merge the sample produced with different polarization and we can use the averaged values to apply the acceptance correction.

From that merging I obtain the following results:

Magnet polarity	Signal acceptance (%)	Normalization acceptance (%)	Ratio (%)
UP	1.765 ±0.009	0.442±0.002	3.99 ±0.03
DOWN	1.754 ±0.009	0.443±0.002	3.96 ±0.03
UP+DOWN	1.760 ±0.007	0.4424±0.0013	3.980 ±0.020

Table 5.2: Effect of polarization on the signal acceptance.

The first and the third period of the run have been taken almost entirely with magnet UP. For those samples I use the acceptance correction in the first row of table 5.2. For the second period, which has roughly the same number of events with magnet polarity UP and DOWN, I will use results of the third row of the same table.

A more precise treatment is not needed since from the comparison between the first and the second raw of table 5.2 the effect of magnet polarity appears to be negligible considering the uncertainties.

5.7 Time windows

The correction described in the last sections do not cover the inefficiencies generated by cuts based on the time measurements for which the Monte-Carlo simulation is not reliable. For this reason I do not apply time cuts in the MC, but I apply symmetric cuts based on the time measurement on time variables between signal and normalization channel. In such a way all the effects producing losses for a failure in the time measurement cancel in the ratio. The symmetrization is possible because the data for the two decays are collected with the same detector at the same time and in both channels we have four in-time particles, two tracks and two photons. For the accuracy required in this analysis the assumption to have a cancellation of these effects is quite safe, nevertheless it is useful to reduce the incidence of these effects in our final sample.

The errors on time measurement have mainly two sources. First, we can have inefficient channel in the sub-detectors or hardware problems in the read-out electronics. Errors can also be produced by accidental particles overlapping with the hits of the event we want to detect. To minimize the first class of problems in the analysis I don't include the bursts classified as "bad burst". We define "bad bursts" the bursts where at least one sub-detector has evident problems in the hardware and/or in the read-out. To minimize the second class of problem instead I reject candidates, for both the signal and the normalization channel, having in-time extra-activity on the detector.

5.8 Residual background

For both the signal and the normalization channel we expect to have residual background affecting our final samples. I will describe in detail the study of residual background for the signal, for the normalization channel I have applied almost the same method and only the results will be shown.

The background can be classified into two main groups: the "physical background", coming from other misidentified decays, and the "accidental background" produced by two overlapping accidental events.

The first type of background is studied with a MC simulation. For the Ξ^0 beta decay I consider, as possible background sources, decays with two tracks and two clusters:

- $\Xi^0 \to \Lambda\pi^0$, $\Lambda \to p\pi^-$
- $\Xi^0 \to \Lambda\pi^0$, $\Lambda \to pe^-\bar{\nu}_e$
- $K_L \to \pi^+\pi^-\pi^0$

For each of these categories 10^8, $2 \cdot 10^6$ and $2 \cdot 10^6$ events respectively have been generated and processed through the standard analysis cuts. The results have been absolutely normalized using PDG branching ratio and the total flux estimate[2] from the normalization channel. The resulting histograms for the effective mass of the positive particle and the π^0 is shown in fig. 5.11 and fig. 5.12, superimposed with the signal. The number of event in the region of the final cut $m_{\Sigma^+_{PDG}} - 8$ $MeV/c^2 < m(p,\pi^0) < m_{\Sigma^+_{PDG}} + 8\ MeV/c^2$ are also given in table 5.3.

channel	B.R.	MC generated	Events before mass cut	Background estimate
$\Xi^0 \to \Lambda\pi^0$, $\Lambda \to p\pi^-$	0.99522	10^8	8	0
$\Xi^0 \to \Lambda\pi^0$, $\Lambda \to pe^-\bar{\nu}_e$	$8.32 \cdot 10^{-4}(\Lambda)$	$2 \cdot 10^6$	4516	13 evts
$K_L \to \pi^+\pi^-\pi^0$	0.1258	$2 \cdot 10^6$	0	$< 10^{-3}$

Table 5.3: Physical background.

The first decay has a BR $\sim$ 4000 times bigger than the signal BR. Nevertheless it has π^- instead of an electron in the final state and is suppressed by the E/p cut which rejects pions with an efficiency of ~98%. In addition it is suppressed by the strong cut to veto Λ decays in the signal sample. At the end, the contribution of this decay to the background in the signal region is completely negligible.

The decay $\Xi^0 \to \Lambda\pi^0$, with $\Lambda \to pe^-\bar{\nu}_e$, has a decay rate, taking into account all the BRs, only $\sim$ 3 times bigger than the signal rate but here the 4 particles in the final state are the same we have in the Ξ^0 beta decay. This decay gives the main contribution to the "physical background".

Finally, for the decay $K_L \to \pi^+\pi^-\pi^0$ the decay rate in the fiducial region is $\sim 10^3$ times bigger with respect to the signal rate; nevertheless I have generated 2 millions $K_L \to \pi^+\pi^-\pi^0$ decays and no events survive to our signal selection. This is enough to exclude this channel from the sources of "physical background" at the level of 10^{-3}.

Concerning the "accidental background" we have several ways in which 2 different

[2] only an order of magnitude estimate for the flux of K^0_L is used, since the corresponding background is found to be negligible.

decays can be overlapped to reproduce a signal decay; in the following list the particles between the parentheses are assumed to come from the same decay:

- (p e^-) (γ γ)
- (p e^- γ) (γ)
- (p γ γ) (e^-)
- (e^- γ γ) (p)
- (e^- γ) (p γ)

It is almost impossible to reproduce this kind of background from the MC; we should generate all the possible pairs of decays taking into account all the particles composing the NA48/I neutral beam. We can instead study this background from data. By extrapolating from appropriate "side band" in the distribution of the time differences between the different tracks and clusters. The distributions, shown in fig. 5.8, are obtained releasing all cuts on the time differences. In order to check the shape of the distributions, in these figures also the final cut, $m_{\Sigma^+_{PDG}} - 8$ $MeV/c^2 < m(p,\pi^0) < m_{\Sigma^+_{PDG}} + 8\ MeV/c^2$, defining the signal region, is released. It is clear that under the Gaussian distributions peaked at 0 and given by the signal and by the "physical background", there are flat distributions due to accidental background.

I can then define out-of-time windows, that I call "side bands", and study the $m(p,\pi^0)$ distribution for events in these regions.

I choose the "side bands" windows to have the same width of signal windows; in this way the number of events to extrapolate in the signal region is exactly equal to the number of events we found in the "side bands". Figure 5.11 shows the resulting mass plot and table 5.4, summarizes the accidental background estimated with the side bands method for the 2002 run.

A final remark has to be made. My cut for background rejection include a condition that rejects events with extra tracks or clusters. I took particular care to

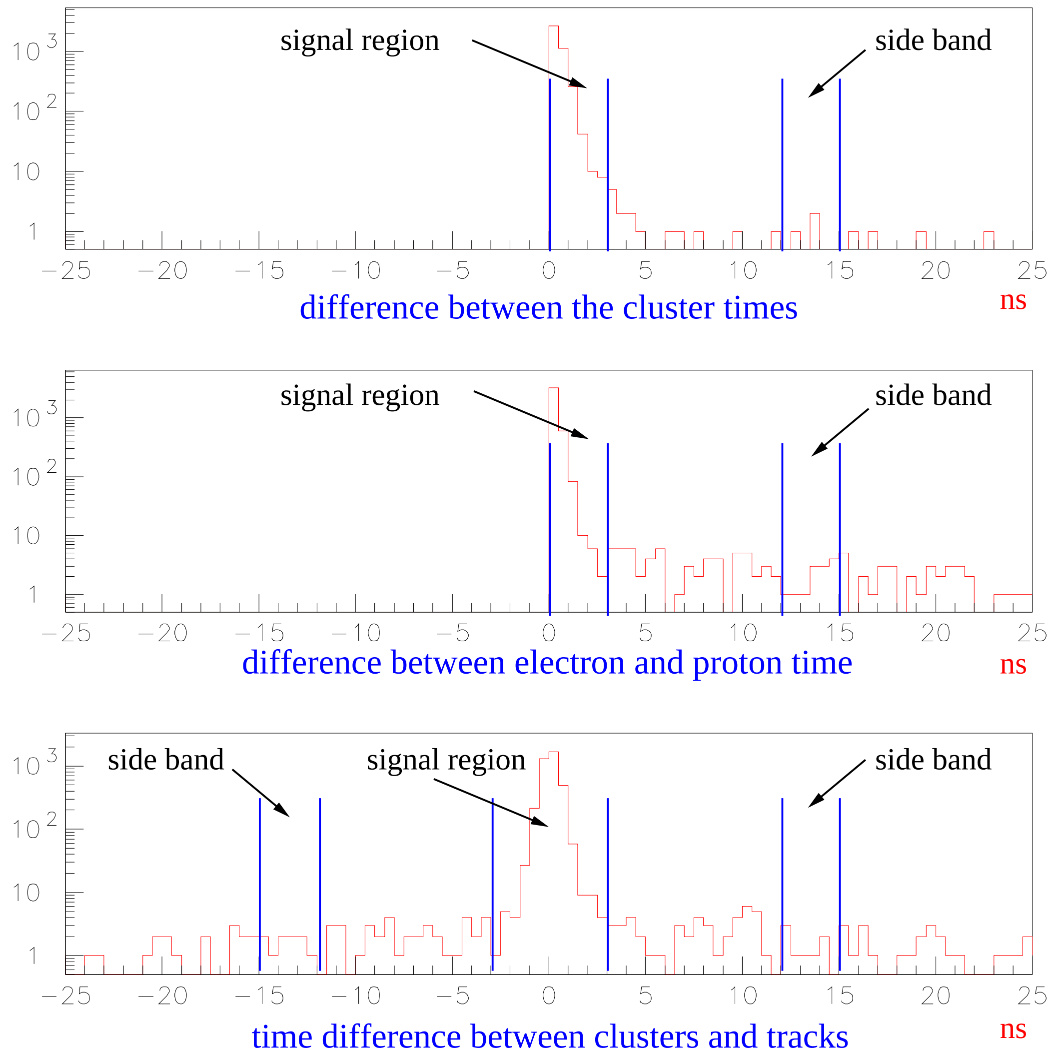

Figure 5.10: On the top the time difference between the two clusters measured from the LKr. On the center the time difference between the two tracks from the $CHOD$. On the bottom the time difference between the average time of the clusters and the average time of the tracks.

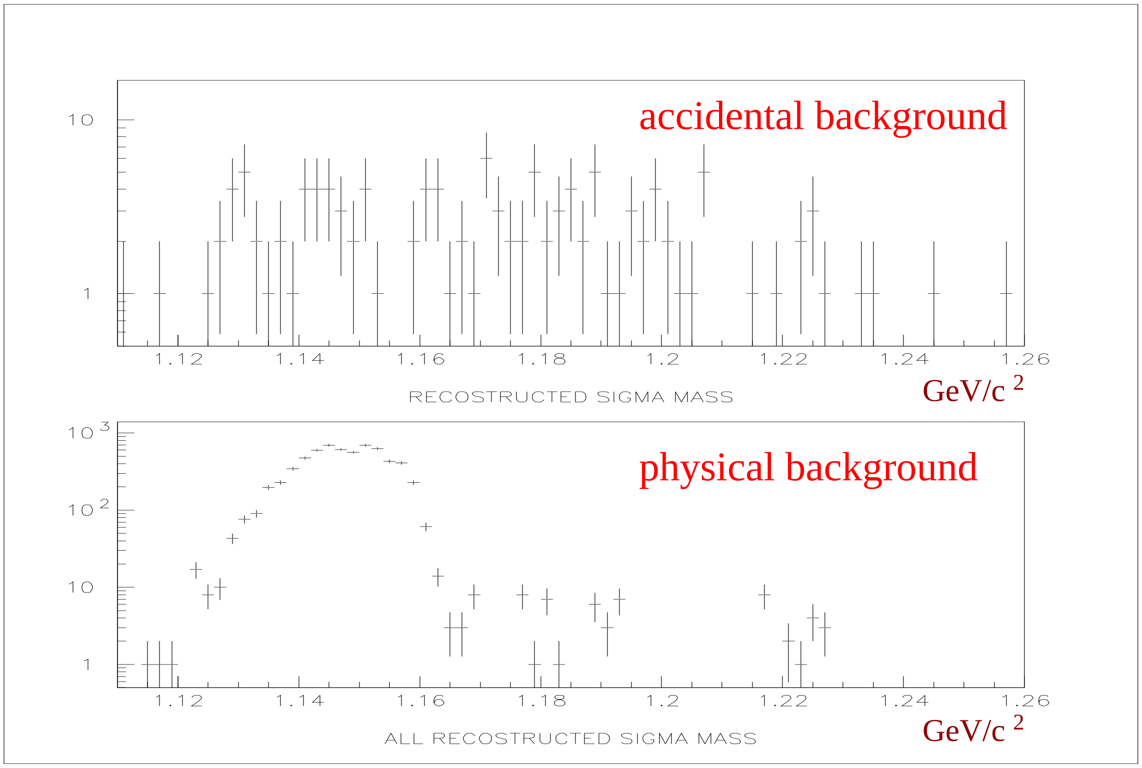

Figure 5.11: On the top the events coming from side bands and passing our selection. On the bottom the overall contribution from physical background (already normalized for the comparison with real data). In both the distributions the signal region is contaminated.

type	events before mass cut	final background
(p e^-) (γ γ)	52	4
(p e^- γ) (γ)	9	4
(p γ γ) (e^-)	7	2
(e^- γ γ) (p)	21	7
(e^- γ) (p γ)	0	0

Table 5.4: accidental background.

avoid to bias the events in the side bands with this condition. For this reason the time window used to veto extra-activity (see sec.5.2) is very wide with respect to the time resolution of the NA48 detector and such to include my "side bands". The overall estimation of the residual background to the signal is shown in fig. 5.13

For the normalization channel I follow the same procedure. In that case, for the "physical background" I consider the following sources:

- $\Xi^0 \to \Sigma^+ e^- \bar{\nu}_e$, $\Sigma^+ \to p\pi^0$

- $\Xi^0 \to \Lambda\pi^0$, $\Lambda \to pe^-\bar{\nu}_e$

- $K_L \to \pi^+\pi^-\pi^0$

but again after the MC simulation we find that only the second channel gives an appreciable contribution to the background.

For the accidental background I again use the "side bands" method. The results of the background study for the $\Xi^0 \to \Lambda\pi^0$ decay are summarized in fig. 5.13. In the table 5.5 I list the final statistics in both the signal and normalization channel for the three periods.

5.9 Final samples and BR measurement

We have now all the main ingredients for the BR measurement. Again I perform a separated calculation for the three different periods of the data taking.

In the table 5.5 I list the final statistics in both the signal and normalization channel for the three periods:

	Period	N. events	$\frac{\Delta N}{N}$ %
Signal	I	453 ± 21	4.7
Normalization	I	31834 ± 178	0.6
Signal	II	3570 ± 60	1.7
Normalization	II	145922 ± 382	0.3
Signal	III	822 ± 29	3.5
Normalization	III	42376 ± 206	0.5

Table 5.5: 2002 statistics.

Clearly the statistics is dominated by the second period. I remind that this is also the best period concerning the trigger efficiency.

The equation giving the BR is the following:

$$BR(\Xi^0 \to \Sigma^+ e^- \bar{\nu}_e) = \frac{N_S^{CORR}}{N_N^{CORR}} \frac{f_N}{f_S} \frac{T_E^{NORM}}{T_E^{SIGN}} \frac{BR(\Xi^0 \to \Lambda\pi^0) BR(\Lambda \to p\pi^-)}{BR(\Sigma^+ \to p\pi^0) D_{LV1}} \tag{5.3}$$

where:

- N_S^{CORR} is the number of events passing the $\Xi^0 \to \Sigma^+ e^- \bar{\nu}_e$ selection, corrected for background and acceptance.

- N_N^{CORR} is the number of events passing the $\Xi^0 \to \Lambda\pi^0$ selection, corrected for background and acceptance.

- f_S is the fraction of $\Xi^0 \to \Sigma^+ e^- \bar{\nu}_e$ decays generated in the Monte-Carlo which give a Σ^+ with momentum between 70 and 240 GeV/c.

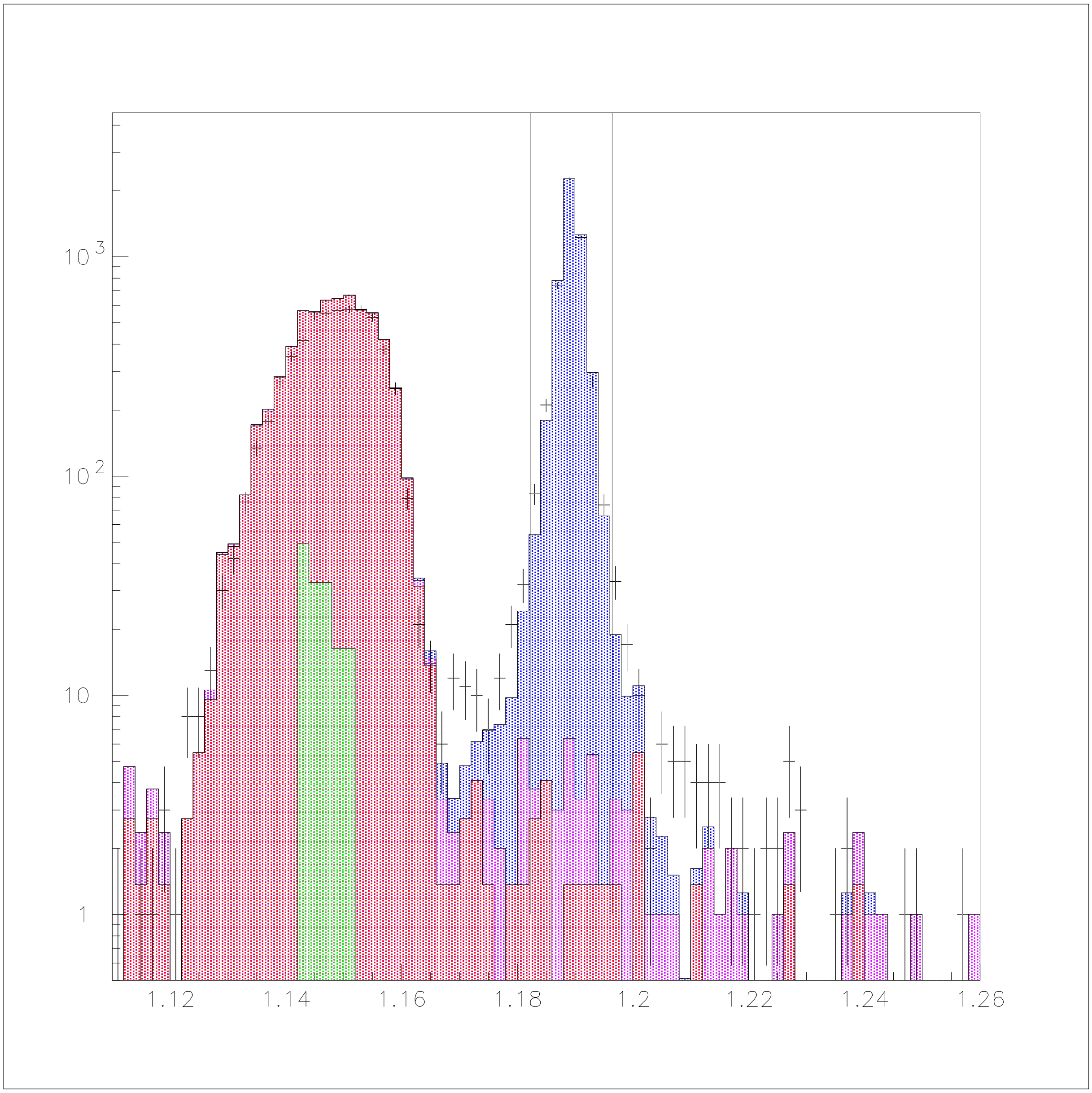

Figure 5.12: proton π^0 invariant mass; the black points with error bars are the data, in blue we have the MC events for the signal, then the other colors represent background coming from different sources (physical background and accidental background).

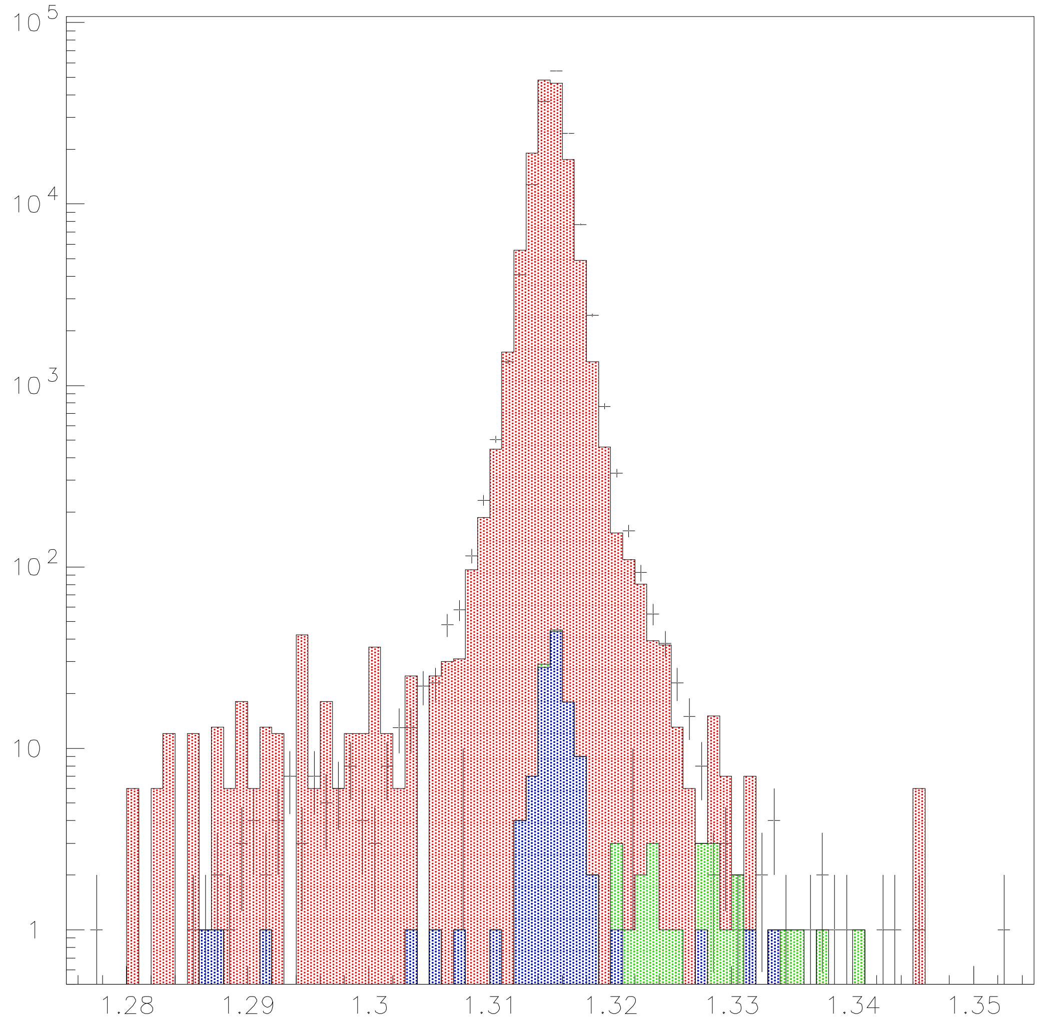

Figure 5.13: Λ π^0 invariant mass; the black points with error bars are the data, in red we have the MC events for the signal, then the other colors represent background coming from different sources (physical background and accidental background).

- f_N is the fraction of $\Xi^0 \to \Lambda\pi^0$ decays generated in the Monte-Carlo which give a Ξ^0 with momentum between 80 and 250 GeV/c.

- T_E^{SIGN} is the overall trigger efficiency for the signal channel.

- T_E^{NORM} is the overall trigger efficiency for the normalization channel.

- D_{LV1} is the LV1 downscaling factor and it is equal to 25 for the run before number 13941 and it is equal to 35 after the run 13941.

- $BR(\Xi^0 \to \Lambda\pi^0)$, $BR(\Lambda \to p\pi^-)$ and $BR(\Sigma^+ \to p\pi^0)$ are the branching ratio of the decays involved in the normalization procedure. For that BRs we take their measured values taken from the Particle Data Book.

  The values of those BRs are listed here:

  $BR(\Xi^0 \to \Lambda\pi^0)$=0.9951 ± 0.0005

  $BR(\Lambda \to p\pi^-)$=0.639 ± 0.005

  $BR(\Sigma^+ \to p\pi^0)$=0.5157 ±0.0030.

N_S^{CORR}, N_N^{CORR} are computed with acceptance corrections in bins of Σ^+ momentum for the signal channel and total momentum for the normalization channel; only the factors f_S and f_N are applied globally to account for the effect of the limited range of accepted momenta.

The formulae used are:

$$N_S^{CORR} = \sum \frac{(N_i - B_i)M_i^{GEN}}{M_i^{ACC}} \tag{5.4}$$

and similarly for the normalization channel, where the symbols N_i,B_i,M_i^{GEN}, andM_i^{ACC} stand for the number of events in the data, the background estimate and the number of generated and accepted events in the Monte-Carlo respectively in a particular bin of energy. Since the available statistics does not allow to estimate the backgrounds in momentum bins, the global background estimate has been subdivided proportionally to the number of events.

Finally, using all the collected information we obtain the following results:

First period : $BR(\Xi^0 \to \Sigma^+ e^- \bar{\nu}_e) = (2.37 \pm 0.30) \cdot 10^{-4}$

Second period: $BR(\Xi^0 \to \Sigma^+ e^- \bar{\nu}_e) = (2.48 \pm 0.09) \cdot 10^{-4}$

Third period : $BR(\Xi^0 \to \Sigma^+ e^- \bar{\nu}_e) = (2.19 \pm 0.22) \cdot 10^{-4}$

Averaging the measured values in the three periods I obtain my preliminary result on the Ξ^0 beta decay:

$$BR(\Xi^0 \to \Sigma^+ e^- \overline{\nu}_e) = [2.45 \pm 0.036(stat.)] \cdot 10^{-4}$$

In the first and in the third periods the measured BR is lower with respect to second period, nevertheless the errors on those measurements are large and then there is no way to search for a disagreement.

In the following section I will review the sources of systematic errors studied up to now.

5.10 Systematic errors and final result

The following sources of systematic errors have been investigated:

- Initial state polarization
- Form factors
- Background subtraction
- Efficiency of DCH at small radii
- Data-MC agreement

I discuss here the checks that I have performed up to now on each of these effects. This work has to be continued in more detail and therefore I give conservative estimates of the systematic errors that have to be considered preliminary.

5.10.1 Initial state polarization

As discussed before, the polarization of the decaying Ξ^0s has not been measured yet, but we have broad limits on its value from other experiments. In principle the polarization can affect the acceptance for both the signal and the normalization channel. In section 5.6 I have already shown the effects of varying the polarization from 0 to 15%. The conclusion is that there is no appreciable dependence of the acceptance within the errors of the Monte-Carlo calculation. I then take as systematic error only the statistical error of the Monte-Carlo on the acceptance ratio computed for a single value of the polarization. This corresponds to a 1.5% contribution to the error on the branching ratio.

5.10.2 Form factors

The form factors of the semileptonic decay are not well measured experimentally (see section 1.5). A change in the form factors can determine a change in the acceptance. In the Monte-Carlo I have used "reasonable" values based on the neutron form factors and assuming SU(3) symmetry. Here I will consider the effects of uncertainties for the parameters $g_1(0)$, $f_2(0)$, that determine the magnitude of the corresponding form factors, and for M_V and M_A that determine the slope of the form factors as a function of q^2. I will change one by one the values of these parameters and determine the change of acceptance between the central value and the border values. Technically I have done this without rerunning the full Monte-Carlo but reweighting the data with the ratio of the decay rates computed with the changed values of the form factors.

For $g_1(0)$ the range that I consider is the one corresponding to the experimental error of the KTEV measurement[21]. For $f_2(0)$ the experimental error from KTEV and the spread of the theoretical predictions for different models of SU(3) breaking [18][56] are quite large. I choose a range that includes all these values. Finally for M_V and M_A I use the errors quoted in reference [22].

The results I obtain are summarized in table 5.6. The parameter that produces

$g_1(0)$	$f_2(0)$	M_V	M_A	Signal acceptance (%)
1.32	2.6	0.97	1.25	1.760 ± 0.007
1.54	2.6	0.97	1.25	1.758 ± 0.007
1.14	2.6	0.97	1.25	1.764 ± 0.007
1.32	3.9	0.97	1.25	1.766 ± 0.007
1.32	1.3	0.97	1.25	1.737 ± 0.007
1.32	2.6	1.01	1.25	1.762 ± 0.007
1.32	2.6	0.93	1.25	1.762 ± 0.007
1.32	2.6	0.97	1.40	1.764 ± 0.007
1.32	2.6	0.97	1.10	1.760 ± 0.007

Table 5.6: Form factors variation: effect on the accptance.

the biggest change is f_2 and also the change of g_1 has some effect. I then decide to fix the values of the slope parameters M_V and M_A to their central value and to check for possible correlations between the changes due to f_2 and g_1 by varying both at the same time. The new results are shown in table 5.7.

$g_1(0)$	$f_2(0)$	M_V	M_A	Signal acceptance (%)
1.14	1.3	0.97	1.25	1.741 ± 0.007
1.54	1.3	0.97	1.25	1.730 ± 0.007
1.14	3.9	0.97	1.25	1.776 ± 0.007
1.54	3.9	0.97	1.25	1.766 ± 0.007

Table 5.7: Form factors variation: effect on the accptance.

The relative difference between the minimum and maximum acceptance obtained is 2.7 and I decide to add a systematic error of 0.8% to the final measurement.

5.10.3 Background subtraction

As discussed in section 5.8, the background is estimated as the sum of a contribution from accidental superposition of different events, estimated by extrapolation of the side bands of the time distributions, and of a physics background estimated from an absolutely normalized Monte-Carlo simulation of the relevant decay channels. Far from the sigma mass peak (fig. 5.12) the estimated background reproduces the data well, but near the peak the estimate is about a factor two lower than the data. Since this excess is not yet understood, I make the conservative assumption that this background subtraction can vary by 100% of its value.

For the normalization channel the background is small, but the Monte-Carlo predicts that this background is peaked under the signal and it is very hard to make experimental tests of this prediction. Again I quote an error corresponding to a variation of the background by 100%.

5.10.4 Efficiency of $DCH1$ at small radii

A systematic analysis of the effects of position dependent inefficiencies in the drift chambers has not been performed yet. As a first check in this direction, I try to evaluate how the result changes if I remove tracks near the beam pipe, where the drift chamber efficiency is known to be critical. For this I use only data from the second period, changing the inner radius cut in chamber 1 from 12 cm to 14 cm. Obviously I also change the cut for the MC data analysis in order to have the appropriate acceptances. The change in branching ratio is $0.01 \cdot 10^{-4}$ (0.4%). This difference is not statistically significant, and I will not apply a systematic error.

5.10.5 Agreement between data and Monte-Carlo

As shown in section 4.5, for the signal channel the agreement of the spectra of the final state particles between data and MC is not perfect. In particular in the electron spectrum, for low electron energies the data are below the MC prediction. In order to check the sensitivity of the result to this small disagreement I tried to reevaluate the branching ratio moving the lower cut on electron momentum from 5 to 10 GeV/c (see table 5.8). The biggest difference on the branching ratio with respect to the

cut	Statistics	BR	Trigger efficiency
$p_e \geq 5:$	$N_{events} = 3570$	$BR = (2.48 \pm 0.09) \cdot 10^{-4}$	90.8 ± 2.3
$p_e \geq 6:$	$N_{events} = 3213$	$BR = (2.48 \pm 0.09) \cdot 10^{-4}$	90.1 ± 2.5
$p_e \geq 7:$	$N_{events} = 2796$	$BR = (2.55 \pm 0.10) \cdot 10^{-4}$	89.8 ± 2.7
$p_e \geq 8:$	$N_{events} = 2313$	$BR = (2.56 \pm 0.11) \cdot 10^{-4}$	91.1 ± 2.8
$p_e \geq 9:$	$N_{events} = 1874$	$BR = (2.53 \pm 0.12) \cdot 10^{-4}$	92.5 ± 2.9
$p_e \geq 10:$	$N_{events} = 1489$	$BR = (2.47 \pm 0.14) \cdot 10^{-4}$	90.0 ± 3.7

Table 5.8: Change of the cut on the lower electron energy: effects on BR and on LV2 trigger efficiency.

standard selection comes from the sample obtained with the cut at 8 GeV/c. Here the BR goes from $2.48 \cdot 10^{-4}$ to $2.56 \cdot 10^{-4}$. We perform a statistical check, taking into account the correlations between the two samples (the first sample includes the second one), and we find that the two results differ by 1.3 standard deviations. Although the statistical evidence of a disagreement is not a compelling, I decide to account for the difference between the two values of the BR as systematic error.

Further studies will probably lead to an understanding of the discrepancy between data and Monte-Carlo and to a reduction of this error, that presently is the largest source of systematic.

In the following table I summarize the main source of error for the measurement including, together with the systematic errors already discussed, those coming from the knowledge of the normalizzation branching ratios of formula 5.3, from the measurement of the trigger efficiency and from the Monte-Carlo statistical error on acceptances:

Summing the systematic errors in quadrature, the final result is

$$BR(\Xi^0 \rightarrow \Sigma^+ e^- \overline{\nu}_e) = [2.45 \pm 0.036(stat.) \pm 0.112(syst.)] \cdot 10^{-4}$$

error sources	$\delta(BR)$ (10^{-4})	$\frac{\delta(BR)}{BR}$ (%)
Stat. sign.	0.036	1.5
Stat. norm.	0.005	0.2
PDG norm.	0.022	0.9
BG sign.	0.015	0.6
BG norm.	0.003	0.1
TE sign (LV2)	0.06	2.5
TE norm (LV1-LV3)	0.003	0.1
ACC sign.	0.010	0.4
ACC norm.	0.005	0.2
Polarization Syst.	0.04	1.5
Form factors Syst.	0.02	0.8
p_e Syst.	0.08	3.2

Table 5.9: Summary of the error on the branching ratio.

As already anticipated the limitation to the precision of our measurement doesn't come from the statistics but from the systematic error on the LV2 trigger efficiency and on the discrepancies between data and MC still visible from spectrum distributions.

Nevertheless our preliminary result at present has a lower error with respect to the most precise measurement already existing on the same item and we have the possibility to improve it improving the study of the systematics.

This measurement is substantially in agreement with the previous measurements of the same BR. There are only two measurements from $KTEV$, the first one already published[14] and giving:
$BR(\Xi^0 \to \Sigma^+ e^- \overline{\nu}_e) = [2.71 \pm 0.22(stat.) \pm 0.31(syst.)] \cdot 10^{-4}$.

The second one is instead a preliminary result[15]:
$BR(\Xi^0 \to \Sigma^+ e^- \overline{\nu}_e) = [2.54 \pm 0.11(stat.) \pm 0.16(syst.)] \cdot 10^{-4}$.

Conclusions

This work describes a preliminary measurement of Ξ^0 beta decay branching ratio.

The analysis is performed on the data collected during 2002 by the NA48/I experiment at the CERN SPS. After 89 days of data taking we collect the largest word sample of $\Xi^0 \rightarrow \Sigma^+ e^- \bar{\nu}_e$ beta decays.

My measured value of the branching ratio of the Ξ^0 beta decay is:

$$BR(\Xi^0 \rightarrow \Sigma^+ e^- \overline{\nu}_e) = [2.45 \pm 0.036(stat.) \pm 0.112(syst.)]$$

The main source of the error comes from systematics, and probably the final NA48 measurement on those data will be limited by the non-reducible error coming from LV2 trigger efficiency.

The analysis of systematic errors needs further refinement and for this reason I have been rather conservative in the estimate of some of them. I expect that, as a result of these ongoing studies, especially on the discrepancies that we still see between the data and the Monte-Carlo, the size of the final error will be reduced.

From this value, using formula 1.37 and the PDG values for the Ξ^0 lifetime and for the ratio g_1/f_1, I obtain the following result for V_{us}, the sine of the Cabibbo angle:

$$V_{us} = 0.212 \pm 0.030$$

The error is evaluated from the propagation of the errors on the BR, on the Ξ^0 lifetime and on the ratio g_1/f_1. For the BR I take the error evaluated with my analysis, for Ξ^0 lifetime and for g_1/f_1 I take the errors listed in the PDG. The error on V_{us} is dominated by the propagation of the error on g_1/f_1.

NA48 collaboration, using the 2002 data, has planned also to study the form factors of the Ξ^0 beta decay with the angular distributions.

Appendix A

Coefficients of the transition rate

In order to define the differential decay rate according to [22] we couple the standard form factors in the following way defining 4 new quantities:

$$
\begin{aligned}
F_1 &= f_1 - (1 + \frac{m_{\Sigma^+}}{m_{\Xi^0}})f_2 \\
F_2 &= -2f_2 \\
F_3 &= f_2 + f_3 \\
G_1 &= g_1 - (1 - \frac{m_{\Sigma^+}}{m_{\Xi^0}})g_2 \\
G_2 &= -2g_2 \\
G_3 &= g_2 + g_3
\end{aligned}
\tag{A.1}
$$

It is also convenient to define:

$$
x_e = \frac{(\vec{p_e} \cdot \vec{p_\nu})}{|\vec{p_e}| m_{\Xi^0}} \tag{A.2}
$$

$$
x_\nu = \frac{(\vec{p_e} \cdot \vec{p_\nu})}{|\vec{p_e}||\vec{p_\nu}|} \frac{\beta_e E_\nu}{m_{\Xi^0}} \tag{A.3}
$$

where $\beta = \frac{p_e}{E_e}$.

We have now all the ingredients to explicitly write the factors D_1, D_2, D_3, D_4 defined in the 1.13:

$$\begin{aligned}
D_1 &= (2-\frac{m_{\Sigma^+}}{m_{\Xi^0}}-\frac{E_e}{m_{\Xi^0}}-\frac{E_\nu}{m_{\Xi^0}}-\frac{m_e}{m_{\Xi^0}E_e})(F_1)^2+\\
&+ \frac{1}{2}(1+\frac{m_{\Sigma^+}}{m_{\Xi^0}}-\frac{E_e}{m_{\Xi^0}}-\frac{E_\nu}{m_{\Xi^0}})(F_2)^2+\\
&+ (1+\frac{m_{\Sigma^+}}{m_{\Xi^0}}-\frac{m_e^2}{m_{\Xi^0}E_e})\Re(F_1F_2)+\\
&+ \frac{m_e^2}{m_{\Xi^0}E_e}(1-\frac{E_e}{m_{\Xi^0}}+\frac{m_{\Sigma^+}}{m_{\Xi^0}})\Re(F_1F_3)+\\
&+ \frac{m_e^2}{m_{\Xi^0}E_e}(1+\frac{m_{\Sigma^+}}{m_{\Xi^0}}-\frac{E_e}{m_{\Xi^0}}-\frac{E_\nu}{m_{\Xi^0}})\Re(F_2F_3)+\\
&+ \frac{m_e^2}{2m_{\Xi^0}^2}(1+\frac{m_{\Sigma^+}}{m_{\Xi^0}}-\frac{E_e}{m_{\Xi^0}}-\frac{E_\nu}{m_{\Xi^0}})\Re(F_3)^2+\\
&+ (2+\frac{m_{\Sigma^+}}{m_{\Xi^0}}-\frac{E_e}{m_{\Xi^0}}-\frac{E_\nu}{m_{\Xi^0}}-\frac{m_e^2}{m_{\Xi^0}E_e})(G_1^2)+\\
&+ \frac{1}{2}(1-\frac{m_{\Sigma^+}}{m_{\Xi^0}}-\frac{E_e}{m_{\Xi^0}}-\frac{E_\nu}{m_{\Xi^0}})(G_2)^2+\\
&+ (-1+\frac{m_{\Sigma^+}}{m_{\Xi^0}}-\frac{m_e^2}{m_{\Xi^0}E_e})\Re(G_1G_2)+\\
&- \frac{m_e^2}{m_{\Xi^0}E_e}(1-\frac{m_{\Sigma^+}}{m_{\Xi^0}}-\frac{E_e}{m_{\Xi^0}})\Re(G_1G_3)+\\
&+ \frac{m_e^2}{m_{\Xi^0}E_e}(1-\frac{m_{\Sigma^+}}{m_{\Xi^0}}-\frac{E_e}{m_{\Xi^0}}-\frac{E_\nu}{m_{\Xi^0}})\Re(G_2G_3)+\\
&+ \frac{m_e^2}{2m_{\Xi^0}^2}(1-\frac{m_{\Sigma^+}}{m_{\Xi^0}}-\frac{E_e}{m_{\Xi^0}}-\frac{E_\nu}{mx})(G_3)^2+\\
&+ 2(\frac{E_e}{m_{\Xi^0}}-\frac{E_\nu}{m_{\Xi^0}}-\frac{m_e^2}{m_{\Xi^0}E_e})\Re(F_1G_1)
\end{aligned}\tag{A.4}$$

$$\begin{aligned}
D_2 &= \left(\frac{E_\nu}{m_{\Xi^0}}+\frac{E_e}{m_{\Xi^0}}+\frac{m_{\Sigma^+}}{m_{\Xi^0}}\right)(F_1)^2+\\
&+ \frac{1}{2}\left(1+\frac{m_{\Sigma^+}}{m_{\Xi^0}}-\frac{E_e}{m_{\Xi^0}}-\frac{E_\nu}{m_{\Xi^0}}\right)(F_2)^2+\\
&+ \left(1+\frac{m_{\Sigma^+}}{m_{\Xi^0}}\right)\Re(F_1F_2)+\left(\frac{m_e^2}{m_{\Xi^0}^2}\right)\Re(F_1F_3)+\\
&+ \left(\frac{m_e^2}{2m_{\Xi^0}^2}\right)\left(-1-\frac{m_{\Sigma^+}}{m_{\Xi^0}}+\frac{E_e}{m_{\Xi^0}}+\frac{E_\nu}{m_{\Xi^0}}\right)(F_3)^2+\\
&+ \left(-\frac{m_{\Sigma^+}}{m_{\Xi^0}}+\frac{E_e}{m_{\Xi^0}}+\frac{E_\nu}{m_{\Xi^0}}\right)(G_1)^2+
\end{aligned}$$

$$
\begin{aligned}
&+ \quad \frac{1}{2}\left(1-\frac{m_{\Sigma^+}}{m_{\Xi^0}}-\frac{E_e}{m_{\Xi^0}}-\frac{E_\nu}{m_{\Xi^0}}\right)(G_2)^2+ \\
&+ \quad \left(-1+\frac{m_{\Sigma^+}}{m_{\Xi^0}}\right)\Re\left(G_1G_2\right)-\left(\frac{m_e^2}{m_{\Xi^0}^2}\right)\Re\left(G_1G_3\right)+ \\
&+ \quad \left(\frac{m_e^2}{2m_{\Xi^0}^2}\right)\left(-1+\frac{m_{\Sigma^+}}{m_{\Xi^0}}+\frac{E_e}{m_{\Xi^0}}+\frac{E_\nu}{m_{\Xi^0}}\right)(G_3)^2+ \\
&+ \quad 2\left(-\frac{E_e}{m_{\Xi^0}}+\frac{E_\nu}{m_{\Xi^0}}\right)\Re\left(F_1G_1\right)
\end{aligned}
\tag{A.5}
$$

$$
\begin{aligned}
D_3 \quad = \quad & \left(-1+\frac{m_{\Sigma^+}}{m_{\Xi^0}}+\frac{E_e}{m_{\Xi^0}}-x_e\right)(F_1)^2+ \\
+ \quad & \left(-\frac{E_\nu}{m_{\Xi^0}}-x_e\right)\Re\left(F_1F_2\right)+ \\
+ \quad & \left(-1-\frac{m_{\Sigma^+}}{m_{\Xi^0}}+\frac{E_e}{m_{\Xi^0}}-x_e\right)(G_1)^2+ \\
+ \quad & \left(\frac{E_\nu}{m_{\Xi^0}}+x_e\right)\Re\left(G_1G_2\right)+ \\
+ \quad & 2\left(1-\frac{E_e}{m_{\Xi^0}}+x_e\right)\Re\left(F_1G_1\right)+ \\
+ \quad & \left(-1+\frac{m_{\Sigma^+}}{m_{\Xi^0}}+\frac{E_e}{m_{\Xi^0}}-x_e\right)\left(\frac{m_e^2}{m_{\Xi^0}^2}\right)+ \\
+ \quad & \left(1+\frac{m_{\Sigma^+}}{m_{\Xi^0}}-\frac{E_\nu}{m_{\Xi^0}}+x_e\right)\Re\left(G_1F_2\right)+ \\
- \quad & \left(\frac{m_e^2}{m_{\Xi^0}^2}\right)\left[\Re\left(F_1G_3\right)-\Re\left(G_1F_3\right)+\Re\left(F_2G_3\right)+\Re\left(F_3G_2\right)\right]+ \\
- \quad & \left(\frac{E_e}{m_{\Xi^0}}+x_e\right)\Re\left(F_2G_2\right)+ \\
+ \quad & \left(\frac{m_e^2}{m_{\Xi^0}^2}\right)\left(-\frac{E_e}{m_{\Xi^0}}+x_e\right)\Re\left(F_3G_3\right)
\end{aligned}
\tag{A.6}
$$

$$
\begin{aligned}
D_4 \quad = \quad & \left(1-\frac{m_{\Sigma^+}}{m_{\Xi^0}}-\frac{E_\nu}{m_{\Xi^0}}-\frac{m_e^2}{m_{\Xi^0}E_e}+x_\nu\right)(F_1)^2+ \\
+ \quad & \left(\frac{E_e}{m_{\Xi^0}}-\frac{m_e^2}{m_{\Xi^0}E_e}+x_\nu\right)\Re\left(F_1F_2\right)+ \\
+ \quad & \left(1+\frac{m_{\Sigma^+}}{m_{\Xi^0}}-\frac{E_\nu}{m_{\Xi^0}}-\frac{m_e^2}{m_{\Xi^0}E_e}+x_\nu\right)(G_1)^2+ \\
+ \quad & \left(-\frac{E_e}{m_{\Xi^0}}+\frac{m_e^2}{m_{\Xi^0}E_e}-x_\nu\right)\Re\left(G_1G_2\right)+
\end{aligned}
$$

$$
\begin{aligned}
&+ \quad 2\left(1-\frac{E_\nu}{m_{\Xi^0}}-\frac{m_e^2}{m_{\Xi^0}E_e}+x_\nu\right)\Re\left(G_1F_1\right)+\\
&+ \quad \left(-1+\frac{m_{\Sigma^+}}{m_{\Xi^0}}+\frac{E_e}{m_{\Xi^0}}-x_\nu\right)\Re\left(F_1G_2\right)+\\
&+ \quad \left(1+\frac{m_{\Sigma^+}}{m_{\Xi^0}}-\frac{E_e}{m_{\Xi^0}}+x_\nu\right)\Re\left(G_1F_2\right)+\\
&+ \quad \left(\frac{m_e^2}{m_{\Xi^0}E_e}\right)\left(-1+\frac{m_{\Sigma^+}}{m_{\Xi^0}}+\frac{E_e}{m_{\Xi^0}}\right)\Re\left(F_1G_3\right)+\\
&+ \quad \left(\frac{m_e^2}{m_{\Xi^0}E_e}\right)\left(1+\frac{m_{\Sigma^+}}{m_{\Xi^0}}-\frac{E_e}{m_{\Xi^0}}\right)\Re\left(G_1F_3\right)+\\
&- \quad \left(\frac{E_\nu}{m_{\Xi^0}}+x_\nu\right)\Re\left(F_2G_2\right)+\\
&- \quad \left(\frac{m_e^2}{m_{\Xi^0}E_e}\right)\left(\frac{E_\nu}{m_{\Xi^0}}\right)\left[\Re\left(F_2G_3\right)+\Re\left(F_3G_2\right)\right]+\\
&+ \quad \left(\frac{m_e^2}{m_{\Xi^0}^2}\right)\left(-\frac{E_\nu}{m_{\Xi^0}}+x_\nu\right)\Re\left(F_3G_3\right)
\end{aligned}
\tag{A.7}
$$

Appendix B

Terms of Σ^+ polarization

In the following $(p_X \cdot p_Y) = (p_X)_\mu (p_Y)^\mu$ (scalar product between 4-vectors)

$$
\begin{aligned}
K_{00} \;=\;& (F_1)^2 \left[2\left(p_{\Xi^0}\cdot p_e\right)\left(p_{\Sigma^+}\cdot p_\nu\right) + \left(p_{\Xi^0}\cdot p_\nu\right)\left(p_{\Sigma^+}\cdot p_e\right) - m_{\Xi^0} m_{\Sigma^+}\left(p_e\cdot p_\nu\right)\right] + \\
+\;& \left[\frac{2\Re\left(F_1F_2\right)}{m_{\Xi^0}}\right]\left[m_{\Xi^0}\left(p_{\Sigma^+}\cdot p_e\right)\left(p_{\Xi^0}\cdot p_\nu\right) + m_{\Xi^0}\left(p_{\Sigma^+}\cdot p_\nu\right)\left(p_{\Xi^0}\cdot p_e\right) + \right. \\
+\;& 2m_{\Sigma^+}\left(p_{\Xi^0}\cdot p_e\right)\left(p_{\Xi^0}\cdot p_\nu\right) - m_{\Xi^0}\left(p_e\cdot p_\nu\right)\left(p_{\Xi^0}\cdot p_{\Sigma^+}\right) + \\
-\;& \left. m^2_{\Xi^0} m_{\Sigma^+}\left(p_e\cdot p_\nu\right)\right] + \left[\frac{2\Re\left(F_1F_3\right) m_e^2}{m_{\Xi^0}}\right]\left[m_{\Xi^0}\left(p_{\Sigma^+}\cdot p_\nu\right) + \right. \\
+\;& \left. m_{\Sigma^+}\left(p_{\Xi^0}\cdot p_\nu\right)\right] + \left[\frac{\left(F_2\right)^2}{m^2_{\Xi^0}}\right]\left[2\left(p_{\Xi^0}\cdot p_e\right)\left(p_{\Xi^0}\cdot p_\nu\right) + \right. \\
-\;& \left. m^2_{\Xi^0}\left(p_e\cdot p_\nu\right)\right]\left[\left(p_{\Xi^0}\cdot p_{\Sigma^+}\right) + m_{\Xi^0} m_{\Sigma^+}\right] + \\
+\;& \left[\frac{2\Re\left(F_2F_3\right) m_e^2\left(p_{\Xi^0}\cdot p_\nu\right)}{m^2_{\Xi^0}}\right]\left[\left(p_{\Xi^0}\cdot p_{\Sigma^+}\right) + m_{\Xi^0} m_{\Sigma^+}\right] + \\
+\;& \left[\frac{2\left(F_3\right)^2 m_e^2\left(p_e\cdot p_\nu\right)}{m^2_{\Xi^0}}\right]\left[\left(p_{\Xi^0}\cdot p_{\Sigma^+}\right) + m_{\Xi^0} m_{\Sigma^+}\right] + \\
+\;& \Re\left(F_1G_1\right)\left\{2\left[\left(p_{\Xi^0}\cdot p_e\right)\left(p_{\Sigma^+}\cdot p_\nu\right) - \left(p_{\Xi^0}\cdot p_\nu\right)\left(p_{\Sigma^+}\cdot p_e\right)\right]\right\} + \\
+\;& (G_1)^2 \left[2\left(p_{\Xi^0}\cdot p_e\right)\left(p_{\Sigma^+}\cdot p_\nu\right) + \left(p_{\Xi^0}\cdot p_\nu\right)\left(p_{\Sigma^+}\cdot p_e\right) + m_{\Xi^0} m_{\Sigma^+}\left(p_e\cdot p_\nu\right)\right] + \\
+\;& \left[-\frac{2\Re\left(G_1G_2\right)}{m_{\Xi^0}}\right]\left[m_{\Xi^0}\left(p_{\Sigma^+}\cdot p_e\right)\left(p_{\Xi^0}\cdot p_\nu\right) + m_{\Xi^0}\left(p_{\Sigma^+}\cdot p_\nu\right)\left(p_{\Xi^0}\cdot p_e\right) + \right. \\
-\;& 2m_{\Sigma^+}\left(p_{\Xi^0}\cdot p_e\right)\left(p_{\Xi^0}\cdot p_\nu\right) - m_{\Xi^0}\left(p_e\cdot p_\nu\right)\left(p_{\Xi^0}\cdot p_{\Sigma^+}\right) + \\
+\;& \left. m^2_{\Xi^0} m_{\Sigma^+}\left(p_e\cdot p_\nu\right)\right] + \left[-\frac{2\Re\left(G_1G_3\right) m_e^2}{m_{\Xi^0}}\right]\left[m_{\Xi^0}\left(p_{\Sigma^+}\cdot p_\nu\right) + \right. \\
-\;& \left. m_{\Sigma^+}\left(p_{\Xi^0}\cdot p_\nu\right)\right] + \left[\frac{\left(G_2\right)^2}{m^2_{\Xi^0}}\right]\left[2\left(p_{\Xi^0}\cdot p_e\right)\left(p_{\Xi^0}\cdot p_\nu\right) + \right.
\end{aligned}
$$

$$
\begin{aligned}
- \quad & m_{\Xi^0}^2 \left(p_e \cdot p_\nu\right)\big] \left[\left(p_{\Xi^0} \cdot p_{\Sigma^+}\right) - m_{\Xi^0} m_{\Sigma^+}\right] + \\
+ \quad & \left[\frac{2\Re\left(G_2 G_3\right) m_e^2 \left(p_{\Xi^0} \cdot p_\nu\right)}{m_{\Xi^0}^2}\right] \left[\left(p_{\Xi^0} \cdot p_{\Sigma^+}\right) - m_{\Xi^0} m_{\Sigma^+}\right] + \\
+ \quad & \left[\frac{2\left(G_3\right)^2 m_e^2 \left(p_e \cdot p_\nu\right)}{m_{\Xi^0}^2}\right] \left[\left(p_{\Xi^0} \cdot p_{\Sigma^+}\right) - m_{\Xi^0} m_{\Sigma^+}\right] + \\
+ \quad & \Re\left(G_1 F_1\right) \left\{2\left[\left(p_{\Xi^0} \cdot p_e\right)\left(p_{\Sigma^+} \cdot p_\nu\right) - \left(p_{\Xi^0} \cdot p_\nu\right)\left(p_{\Sigma^+} \cdot p_e\right)\right]\right\}
\end{aligned}
\tag{B.1}
$$

$$
\begin{aligned}
\left(K \cdot P_{\Xi^0}\right) \quad = \quad & \left[2\left(F_1\right)^2\right] \left\{\left[m_{\Xi^0}\left(p_{\Sigma^+} \cdot p_\nu\right) - m_{\Sigma^+}\left(p_{\Xi^0} \cdot p_\nu\right)\right]\left(P_{\Xi^0} \cdot p_e\right) + \right. \\
- \quad & \left.\left[m_{\Xi^0}\left(p_{\Sigma^+} \cdot p_e\right) - m_{\Sigma^+}\left(p_{\Xi^0} \cdot p_e\right)\right]\left(P_{\Xi^0} \cdot p_\nu\right)\right\} + \\
+ \quad & \left[\frac{2\Re\left(F_1 F_2\right)}{m_{\Xi^0}}\right] \left\{-\left[\left(p_{\Xi^0} \cdot p_{\Sigma^+}\right)\left(p_{\Xi^0} \cdot p_\nu\right) - m_{\Xi^0}^2\left(p_{\Sigma^+} \cdot p_\nu\right)\right]\left(P_{\Xi^0} \cdot p_e\right) + \right. \\
+ \quad & \left.\left[\left(p_{\Xi^0} \cdot p_{\Sigma^+}\right)\left(p_{\Xi^0} \cdot p_e\right) - m_{\Xi^0}^2\left(p_{\Sigma^+} \cdot p_e\right)\right]\left(P_{\Xi^0} \cdot p_\nu\right)\right\} + \\
+ \quad & \left[2\Re\left(F_1 G_1\right) m_{\Xi^0}\right]\left[\left(p_{\Sigma^+} \cdot p_\nu\right)\left(P_{\Xi^0} \cdot p_e\right) + \left(p_{\Sigma^+} \cdot p_e\right)\left(P_{\Xi^0} \cdot p_\nu\right)\right] + \\
+ \quad & \left[\frac{2\Re\left(F_1 G_2\right)}{m_{\Xi^0}}\right] \left\{\left[m_{\Xi^0} m_{\Sigma^+}\left(p_{\Xi^0} \cdot p_\nu\right) - \left(p_{\Xi^0} \cdot p_{\Sigma^+}\right)\left(p_{\Xi^0} \cdot p_\nu\right) + \right.\right. \\
- \quad & \left. 2\left(p_{\Xi^0} \cdot p_e\right)\left(p_{\Xi^0} \cdot p_\nu\right) + m_{\Xi^0}^2\left(p_e \cdot p_\nu\right)\right]\left(P_{\Xi^0} \cdot p_e\right) + \\
+ \quad & \left[m_{\Xi^0} m_{\Sigma^+}\left(p_{\Xi^0} \cdot p_e\right) - \left(p_{\Xi^0} \cdot p_{\Sigma^+}\right)\left(p_{\Xi^0} \cdot p_e\right) + \right. \\
- \quad & \left.\left. 2\left(p_{\Xi^0} \cdot p_e\right)\left(p_{\Xi^0} \cdot p_\nu\right) + m_{\Xi^0}^2\left(p_e \cdot p_\nu\right)\right]\left(P_{\Xi^0} \cdot p_\nu\right)\right\} + \\
+ \quad & \left[\frac{2 m_e^2 \Re\left(F_1 G_3\right)}{m_{\Xi^0}}\right] \left\{-\left(p_{\Xi^0} \cdot p_\nu\right)\left(P_{\Xi^0} \cdot p p_e\right) + \right. \\
- \quad & \left.\left[\left(p_{\Xi^0} \cdot p_{\Sigma^+}\right) - m_{\Xi^0} m_{\Sigma^+}\left(p_{\Xi^0} \cdot p_\nu\right)\right]\left(P_{\Xi^0} \cdot p_\nu\right)\right\} + \\
+ \quad & \left[\frac{\Re\left(F_2 G_2\right)}{m_{\Xi^0}^2}\right]\left[2\left(p_{\Xi^0} \cdot p_e\right)\left(p_{\Xi^0} \cdot p_\nu\right) - m_{\Xi^0}^2\left(p_e \cdot p_\nu\right)\right] \cdot \\
\cdot \quad & \left[-m_{\Xi^0}\left(P_{\Xi^0} \cdot p_e\right) - m_{\Xi^0}\left(P_{\Xi^0} \cdot p_\nu\right)\right] + \\
+ \quad & \left[\frac{2\Re\left(F_2 G_3\right) m_e^2\left(p_{\Xi^0} \cdot p_\nu\right)}{m_{\Xi^0}^2}\right]\left[-m_{\Xi^0}\left(P_{\Xi^0} \cdot p_e\right) - m_{\Xi^0}\left(P_{\Xi^0} \cdot p_\nu\right)\right] + \\
+ \quad & \left[\frac{\Re\left(F_3 G_3\right) m_e^2\left(p_e \cdot p_\nu\right)}{m_{\Xi^0}^2}\right]\left[-m_{\Xi^0}\left(P_{\Xi^0} \cdot p_e\right) - m_{\Xi^0}\left(P_{\Xi^0} \cdot p_\nu\right)\right] + \\
+ \quad & \left[2\left(G_1\right)^2\right] \left\{\left[m_{\Xi^0}\left(p_{\Sigma^+} \cdot p_\nu\right) + m_{\Sigma^+}\left(p_{\Xi^0} \cdot p_\nu\right)\right]\left(P_{\Xi^0} \cdot p_e\right) + \right. \\
- \quad & \left.\left[m_{\Xi^0}\left(p_{\Sigma^+} \cdot p_e\right) + m_{\Sigma^+}\left(p_{\Xi^0} \cdot p_e\right)\right]\left(P_{\Xi^0} \cdot p_\nu\right)\right\} + \\
- \quad & \left[\frac{2\Re\left(G_1 G_2\right)}{m_{\Xi^0}}\right] \left\{-\left[\left(p_{\Xi^0} \cdot p_{\Sigma^+}\right)\left(p_{\Xi^0} \cdot p_\nu\right) - m_{\Xi^0}^2\left(p_{\Sigma^+} \cdot p_\nu\right)\right]\left(P_{\Xi^0} \cdot p_e\right) + \right. \\
+ \quad & \left.\left[\left(p_{\Xi^0} \cdot p_{\Sigma^+}\right)\left(p_{\Xi^0} \cdot p_e\right) - m_{\Xi^0}^2\left(p_{\Sigma^+} \cdot p_e\right)\right]\left(P_{\Xi^0} \cdot p_\nu\right)\right\} + \\
+ \quad & \left[2\Re\left(F_1 G_1\right) m_{\Xi^0}\right]\left[\left(p_{\Sigma^+} \cdot p_\nu\right)\left(P_{\Xi^0} \cdot p_e\right) + \left(p_{\Sigma^+} \cdot p_e\right)\left(P_{\Xi^0} \cdot p_\nu\right)\right] + \\
- \quad & \left[\frac{2\Re\left(G_1 F_2\right)}{m_{\Xi^0}}\right] \left\{\left[-m_{\Xi^0} m_{\Sigma^+}\left(p_{\Xi^0} \cdot p_\nu\right) - \left(p_{\Xi^0} \cdot p_{\Sigma^+}\right)\left(p_{\Xi^0} \cdot p_\nu\right) + \right.\right.
\end{aligned}
$$

$$
\begin{aligned}
- &\quad 2\left(p_{\Xi^0}\cdot p_e\right)\left(p_{\Xi^0}\cdot p_\nu\right)+m_{\Xi^0}^2\left(p_e\cdot p_\nu\right)\Big]\left(P_{\Xi^0}\cdot p_e\right)+\\
+ &\quad \left[-m_{\Xi^0}m_{\Sigma^+}\left(p_{\Xi^0}\cdot p_e\right)-\left(p_{\Xi^0}\cdot p_{\Sigma^+}\right)\left(p_{\Xi^0}\cdot p_e\right)+\right.\\
- &\quad 2\left(p_{\Xi^0}\cdot p_e\right)\left(p_{\Xi^0}\cdot p_\nu\right)+m_{\Xi^0}^2\left(p_e\cdot p_\nu\right)\Big]\left(P_{\Xi^0}\cdot p_\nu\right)\Big\}+\\
+ &\quad \left[-\frac{2m_e^2\Re\left(G_1F_3\right)}{m_{\Xi^0}}\right]\left\{-\left(p_{\Xi^0}\cdot p_\nu\right)\left(P_{\Xi^0}\cdot pp_e\right)+\right.\\
- &\quad \left.\left[\left(p_{\Xi^0}\cdot p_{\Sigma^+}\right)+m_{\Xi^0}m_{\Sigma^+}\left(p_{\Xi^0}\cdot p_\nu\right)\right]\left(P_{\Xi^0}\cdot p_\nu\right)\right\}+\\
+ &\quad \left[\frac{\Re\left(F_2G_2\right)}{m_{\Xi^0}^2}\right]\left[2\left(p_{\Xi^0}\cdot p_e\right)\left(p_{\Xi^0}\cdot p_\nu\right)-m_{\Xi^0}^2\left(p_e\cdot p_\nu\right)\right]\cdot\\
\cdot &\quad \left[-m_{\Xi^0}\left(P_{\Xi^0}\cdot p_e\right)-m_{\Xi^0}\left(P_{\Xi^0}\cdot p_\nu\right)\right]+\\
+ &\quad \left[\frac{2\Re\left(G_2F_3\right)m_e^2\left(p_{\Xi^0}\cdot p_\nu\right)}{m_{\Xi^0}^2}\right]\left[-m_{\Xi^0}\left(P_{\Xi^0}\cdot p_e\right)-m_{\Xi^0}\left(P_{\Xi^0}\cdot p_\nu\right)\right]+\\
+ &\quad \left[\frac{\Re\left(F_3G_3\right)m_e^2\left(p_e\cdot p_\nu\right)}{m_{\Xi^0}^2}\right]\left[-m_{\Xi^0}\left(P_{\Xi^0}\cdot p_e\right)-m_{\Xi^0}\left(P_{\Xi^0}\cdot p_\nu\right)\right] \qquad \text{(B.2)}
\end{aligned}
$$

$$
\begin{aligned}
K^\mu &= 2(F_1)^2\left\{\left[m_{\Xi^0}\left(p_{\Sigma^+}\cdot p_\nu\right)-m_{\Sigma^+}\left(p_{\Xi^0}\cdot p_\nu\right)\right]p_e^\mu+\right.\\
&- \left.\left[m_{\Xi^0}\left(p_{\Sigma^+}\cdot p_e\right)-m_{\Sigma^+}\left(p_{\Xi^0}\cdot p_e\right)\right]p_\nu^\mu\right\}+\\
&+ \left[\frac{2\Re\left(F_1F_2\right)}{m_{\Xi^0}}\right]\left\{\left[\left(p_{\Xi^0}\cdot p_{\Sigma^+}\right)\left(p_{\Sigma^+}\cdot p_\nu\right)-m_{\Sigma^+}^2\left(p_{\Xi^0}\cdot p_\nu\right)\right]p_e^\mu+\right.\\
&- \left.\left[\left(p_{\Xi^0}\cdot p_{\Sigma^+}\right)\left(p_{\Sigma^+}\cdot p_e\right)-m_{\Sigma^+}^2\left(p_{\Xi^0}\cdot p_e\right)\right]p_\nu^\mu\right\}+\\
&+ \left[\Re\left(F_1G_1\right)2m_{\Sigma^+}\right]\left[\left(p_{\Xi^0}\cdot p_\nu\right)p_e^\mu+\left(p_{\Xi^0}\cdot p_e\right)p_\nu^\mu\right]+\\
&+ \left[\frac{2\Re\left(F_1G_2\right)}{m_{\Xi^0}}\right]\left\{\left[-m_{\Xi^0}m_{\Sigma^+}\left(p_{\Xi^0}\cdot p_\nu\right)+\left(p_{\Xi^0}\cdot p_{\Sigma^+}\right)\left(p_{\Xi^0}\cdot p_\nu\right)-\right.\right.\\
&+ \left.\left(p_{\Xi^0}\cdot p_e\right)\left(p_{\Sigma^+}\cdot p_\nu\right)-\left(p_{\Xi^0}\cdot p_\nu\right)\left(p_{\Sigma^+}\cdot p_e\right)+m_{\Xi^0}m_{\Sigma^+}\left(p_e\cdot p_\nu\right)\right]p_e^\mu+\\
&+ \left[-m_{\Xi^0}m_{\Sigma^+}\left(p_{\Xi^0}\cdot p_e\right)+\left(p_{\Xi^0}\cdot p_{\Sigma^+}\right)\left(p_{\Xi^0}\cdot p_e\right)+\right.\\
&- \left.\left.\left(p_{\Xi^0}\cdot p_e\right)\left(p_{\Sigma^+}\cdot p_\nu\right)-\left(p_{\Xi^0}\cdot p_\nu\right)\left(p_{\Sigma^+}\cdot p_e\right)+m_{\Xi^0}m_{\Sigma^+}\left(p_e\cdot p_\nu\right)\right]p_\nu^\mu\right\}+\\
&+ \left[\frac{2m_e^2\Re\left(F_1G_3\right)}{m_{\Xi^0}}\right]\left\{-\left(p_{\Sigma^+}\cdot p_\nu\right)p_e^\mu-\left[-\left(p_{\Xi^0}\cdot p_{\Sigma^+}\right)+\right.\right.\\
&+ \left.\left.m_{\Xi^0}m_{\Sigma^+}+\left(p_{\Sigma^+}\cdot p_\nu\right)\right]p_\nu^\mu\right\}+\\
&+ \left[\frac{\Re\left(F_2G_2\right)}{m_{\Xi^0}^2}\right]\left[2\left(p_{\Xi^0}\cdot p_e\right)\left(p_{\Xi^0}\cdot p_\nu\right)-m_{\Xi^0}^2\left(p_e\cdot p_\nu\right)\right]\left(-m_{\Sigma^+}p_e^\mu-m_{\Sigma^+}p_\nu^\mu\right)+\\
&+ \left[\frac{2\Re\left(F_2G_3\right)m_e^2\left(p_{\Xi^0}\cdot p_\nu\right)}{m_{\Xi^0}^2}\right]\left(-m_{\Sigma^+}p_e^\mu-m_{\Sigma^+}p_\nu^\mu\right)+\\
&+ \left[\frac{\Re\left(F_3G_3\right)\left(p_e\cdot p_\nu\right)m_e^2}{m_{\Xi^0}^2}\right]\left(-m_{\Sigma^+}p_e^\mu-m_{\Sigma^+}p_\nu^\mu\right)+\\
&- 2(G_1)^2\left\{\left[m_{\Xi^0}\left(p_{\Sigma^+}\cdot p_\nu\right)+m_{\Sigma^+}\left(p_{\Xi^0}\cdot p_\nu\right)\right]p_e^\mu+\right.\\
&- \left.\left[m_{\Xi^0}\left(p_{\Sigma^+}\cdot p_e\right)+m_{\Sigma^+}\left(p_{\Xi^0}\cdot p_e\right)\right]p_\nu^\mu\right\}+
\end{aligned}
$$

$$
\begin{aligned}
+ & \left[-\frac{2\Re\left(G_1G_2\right)}{m_{\Xi^0}}\right]\left\{\left[\left(p_{\Xi^0}\cdot p_{\Sigma^+}\right)\left(p_{\Sigma^+}\cdot p_\nu\right)-m_{\Sigma^+}^2\left(p_{\Xi^0}\cdot p_\nu\right)\right]p_e^\mu+\right.\\
- & \left.\left[\left(p_{\Xi^0}\cdot p_{\Sigma^+}\right)\left(p_{\Sigma^+}\cdot p_e\right)-m_{\Sigma^+}^2\left(p_{\Xi^0}\cdot p_e\right)\right]p_\nu^\mu\right\}+\\
+ & \left[-\Re\left(F_1G_1\right)2m_{\Sigma^+}\right]\left[\left(p_{\Xi^0}\cdot p_\nu\right)p_e^\mu+\left(p_{\Xi^0}\cdot p_e\right)p_\nu^\mu\right]+\\
+ & \left[-\frac{2\Re\left(G_1F_2\right)}{m_{\Xi^0}}\right]\left\{\left[+m_{\Xi^0}m_{\Sigma^+}\left(p_{\Xi^0}\cdot p_\nu\right)+\left(p_{\Xi^0}\cdot p_{\Sigma^+}\right)\left(p_{\Xi^0}\cdot p_\nu\right)+\right.\right.\\
- & \left.\left(p_{\Xi^0}\cdot p_e\right)\left(p_{\Sigma^+}\cdot p_\nu\right)-\left(p_{\Xi^0}\cdot p_\nu\right)\left(p_{\Sigma^+}\cdot p_e\right)-m_{\Xi^0}m_{\Sigma^+}\left(p_e\cdot p_\nu\right)\right]p_e^\mu+\\
+ & \left[m_{\Xi^0}m_{\Sigma^+}\left(p_{\Xi^0}\cdot p_e\right)+\left(p_{\Xi^0}\cdot p_{\Sigma^+}\right)\left(p_{\Xi^0}\cdot p_e\right)+\right.\\
- & \left.\left.\left(p_{\Xi^0}\cdot p_e\right)\left(p_{\Sigma^+}\cdot p_\nu\right)-\left(p_{\Xi^0}\cdot p_\nu\right)\left(p_{\Sigma^+}\cdot p_e\right)-m_{\Xi^0}m_{\Sigma^+}\left(p_e\cdot p_\nu\right)\right]p_\nu^\mu\right\}+\\
+ & \left[-\frac{2m_e^2\Re\left(G_1F_3\right)}{m_{\Xi^0}}\right]\left\{-\left(p_{\Sigma^+}\cdot p_\nu\right)p_e^\mu-\left[-\left(p_{\Xi^0}\cdot p_{\Sigma^+}\right)+\right.\right.\\
- & \left.\left.m_{\Xi^0}m_{\Sigma^+}+\left(p_{\Sigma^+}\cdot p_\nu\right)\right]p_\nu^\mu\right\}+\\
+ & \left[\frac{\Re\left(G_2F_2\right)}{m_{\Xi^0}^2}\right]\left[2\left(p_{\Xi^0}\cdot p_e\right)\left(p_{\Xi^0}\cdot p_\nu\right)-m_{\Xi^0}^2\left(p_e\cdot p_\nu\right)\right]\left(+m_{\Sigma^+}p_e^\mu+m_{\Sigma^+}p_\nu^\mu\right)+\\
+ & \left[\frac{2\Re\left(G_2F_3\right)m_e^2\left(p_{\Xi^0}\cdot p_\nu\right)}{m_{\Xi^0}^2}\right]\left(+m_{\Sigma^+}p_e^\mu+m_{\Sigma^+}p_\nu^\mu\right)+\\
+ & \left[\frac{\Re\left(F_3G_3\right)\left(p_e\cdot p_\nu\right)m_e^2}{m_{\Xi^0}^2}\right]\left(m_{\Sigma^+}p_e^\mu+m_{\Sigma^+}p_\nu^\mu\right)
\end{aligned}
\tag{B.3}
$$

$$
\begin{aligned}
K^{\nu\lambda}\left(P_{\Xi^0}\right)_\lambda = & \; 2\left(F_1\right)^2\left\{\left(P_{\Xi^0}\cdot p_e\right)\left[2\left(p_{\Xi^0}\cdot p_\nu\right)-m_{\Xi^0}^2+m_{\Xi^0}m_{\Sigma^+}\right]p_\nu^\mu+\right.\\
+ & \left(P_{\Xi^0}\cdot p_\nu\right)\left[2\left(p_{\Xi^0}\cdot p_e\right)-m_{\Xi^0}^2+m_{\Xi^0}m_{\Sigma^+}-m_e^2\right]p_e^\mu+\\
+ & \left(P_{\Xi^0}\cdot p_\nu\right)-m_e^2p_\nu^\mu+\left[m_{\Xi^0}^2\left(p_e\cdot p_\nu\right)+\right.\\
- & \left.\left.2\left(p_{\Xi^0}\cdot p_e\right)\left(p_{\Xi^0}\cdot p_\nu\right)+m_e^2\left(p_{\Xi^0}\cdot p_\nu\right)\right]pippo\right\}+\\
+ & \left[\frac{2\Re\left(F_1F_2\right)}{m_{\Xi^0}}\right]\left\{\left(P_{\Xi^0}\cdot p_e\right)\left[m_{\Sigma^+}\left(p_{\Xi^0}\cdot p_\nu\right)-m_{\Xi^0}\left(p_{\Sigma^+}\cdot p_\nu\right)\right]p_e^\mu+\right.\\
+ & \left(P_{\Xi^0}\cdot p_e\right)\left[m_{\Sigma^+}\left(p_{\Xi^0}\cdot p_\nu\right)-m_{\Xi^0}\left(p_{\Sigma^+}\cdot p_e\right)-m_{\Xi^0}m_e^2\right]p_\nu^\mu+\\
+ & \left(P_{\Xi^0}\cdot p_\nu\right)\left[m_{\Sigma^+}\left(p_{\Xi^0}\cdot p_e\right)-m_{\Xi^0}\left(p_{\Sigma^+}\cdot p_\nu\right)\right]p_e^\mu+\\
+ & \left(P_{\Xi^0}\cdot p_\nu\right)\left[m_{\Sigma^+}\left(p_{\Xi^0}\cdot p_\nu\right)-m_{\Xi^0}\left(p_{\Sigma^+}\cdot p_e\right)-m_{\Xi^0}m_e^2\right]p_\nu^\mu+\\
+ & \left[m_{\Xi^0}^2\left(m_{\Xi^0}+m_{\Sigma^+}\right)\left(p_e\cdot p_\nu\right)-2\left(m_{\Xi^0}+m_{\Sigma^+}\right)\left(p_{\Xi^0}\cdot p_e\right)\left(p_{\Xi^0}\cdot p_\nu\right)+\right.\\
+ & \left.\left.m_e^2\left(m_{\Xi^0}+m_{\Sigma^+}\right)\left(p_{\Xi^0}\cdot p_\nu\right)\right]\left(P_{\Xi^0}\right)_\nu g^{\mu\nu}\right\}+\\
+ & \left[\frac{2\Re\left(F_1F_3\right)m_e^2}{m_{\Xi^0}}\right]\left\{-m_{\Xi^0}\left(p_e\cdot p_\nu\right)p_\nu^\mu+\right.\\
+ & m_{\Sigma^+}\left(P_{\Xi^0}\cdot p_\nu\right)p_e^\mu+\left(P_{\Xi^0}\cdot p_\nu\right)\left(-m_{\Xi^0}+m_{\Sigma^+}\right)p_\nu^\mu+\\
+ & \left.\left[m_{\Xi^0}\left(p_{\Sigma^+}\cdot p_\nu\right)+m_{\Sigma^+}\left(p_{\Xi^0}\cdot p_\nu\right)\right]\left(P_{\Xi^0}\right)_\nu g^{\mu\nu}\right\}+\\
+ & \left[-\frac{\left(F_2\right)^2}{m_{\Xi^0}^2}\right]\left[2\left(p_{\Xi^0}\cdot p_e\right)\left(p_{\Xi^0}\cdot p_\nu\right)-m_{\Xi^0}^2\left(p_e\cdot p_\nu\right)\right]\cdot
\end{aligned}
$$

$$
\begin{aligned}
\cdot \quad & \left\{\left(P_{\Xi^0}\cdot p_e\right)p_e^{\mu}+\left(P_{\Xi^0}\cdot p_e\right)p_\nu^{\mu}+\left(P_{\Xi^0}\cdot p_\nu\right)p_e^{\mu}+\right.\\
+ \quad & \left.\left(P_{\Xi^0}\cdot p_\nu\right)p_\nu^{\mu}+\left[\left(p_{\Xi^0}\cdot p_{\Sigma^+}\right)+m_{\Xi^0}m_{\Sigma^+}\right]\left(P_{\Xi^0}\right)_\nu g^{\mu\nu}\right\}+\\
+ \quad & \left[\frac{-2\Re\left(F_2F_3\right)m_e^2\left(p_{\Xi^0}\cdot p_\nu\right)}{m_{\Xi^0}^2}\right]\cdot\\
\cdot \quad & \left\{\left(P_{\Xi^0}\cdot p_e\right)p_e^{\mu}+\left(P_{\Xi^0}\cdot p_e\right)p_\nu^{\mu}+\left(P_{\Xi^0}\cdot p_\nu\right)p_e^{\mu}+\right.\\
+ \quad & \left.\left(P_{\Xi^0}\cdot p_\nu\right)p_\nu^{\mu}+\left[\left(p_{\Xi^0}\cdot p_{\Sigma^+}\right)+m_{\Xi^0}m_{\Sigma^+}\right]\left(P_{\Xi^0}\right)_\nu g^{\mu\nu}\right\}+\\
- \quad & \left[\frac{\left(F_3\right)^2m_e^2\left(p_e\cdot p_\nu\right)}{m_{\Xi^0}^2}\right]\left\{\left(P_{\Xi^0}\cdot p_e\right)p_e^{\mu}+\right.\\
+ \quad & \left(P_{\Xi^0}\cdot p_e\right)p_\nu^{\mu}+\left(P_{\Xi^0}\cdot p_\nu\right)p_e^{\mu}+\left(P_{\Xi^0}\cdot p_\nu\right)p_\nu^{\mu}+\\
+ \quad & \left.\left[\left(p_{\Xi^0}\cdot p_{\Sigma^+}\right)+m_{\Xi^0}m_{\Sigma^+}\right]\left(P_{\Xi^0}\right)_\nu g^{\mu\nu}\right\}+\\
+ \quad & \left[\Re\left(F_1G_1\right)2m_{\Xi^0}m_{\Sigma^+}\right]\left[\left(P_{\Xi^0}\cdot p_e\right)p_\nu^{\mu}-\left(P_{\Xi^0}\cdot p_\nu\right)p_e^{\mu}\right]+\\
+ \quad & \left[\frac{2\Re\left(F_1G_2\right)}{m_{\Xi^0}}\right]\left\{\left(P_{\Xi^0}\cdot p_e\right)\left[-m_{\Xi^0}\left(p_{\Sigma^+}\cdot p_\nu\right)+m_{\Sigma^+}\left(p_{\Xi^0}\cdot p_\nu\right)\right]p_e^{\mu}+\right.\\
+ \quad & \left(P_{\Xi^0}\cdot p_e\right)\left[-m_{\Xi^0}\left(p_{\Sigma^+}\cdot p_\nu\right)+m_{\Sigma^+}\left(p_{\Xi^0}\cdot p_\nu\right)+\right.\\
+ \quad & \left.m_{\Xi^0}\left(p_{\Xi^0}\cdot p_{\Sigma^+}\right)-m_{\Xi^0}^2m_{\Sigma^+}\right]p_\nu^{\mu}+\\
+ \quad & \left(P_{\Xi^0}\cdot p_\nu\right)\left[m_{\Xi^0}\left(p_{\Sigma^+}\cdot p_e\right)-m_{\Sigma^+}\left(p_{\Xi^0}\cdot p_e\right)+\right.\\
- \quad & \left.m_{\Xi^0}\left(p_{\Xi^0}\cdot p_{\Sigma^+}\right)+m_{\Xi^0}^2m_{\Sigma^+}\right]p_e^{\mu}+\\
+ \quad & \left.\left(P_{\Xi^0}\cdot p_\nu\right)\left[m_{\Xi^0}\left(p_{\Sigma^+}\cdot p_e\right)-m_{\Sigma^+}\left(p_{\Xi^0}\cdot p_e\right)\right]p_\nu^{\mu}\right\}+\\
- \quad & \left\{-\left[2\left(G_1\right)^2\right]\left\{\left(P_{\Xi^0}\cdot p_e\right)\left[2\left(p_{\Xi^0}\cdot p_\nu\right)-m_{\Xi^0}^2-m_{\Xi^0}m_{\Sigma^+}\right]p_\nu^{\mu}+\right.\right.\\
+ \quad & \left(P_{\Xi^0}\cdot p_\nu\right)\left[2\left(p_{\Xi^0}\cdot p_e\right)-m_{\Xi^0}^2-m_{\Xi^0}m_{\Sigma^+}-m_e^2\right]p_e^{\mu}+\\
+ \quad & \left(P_{\Xi^0}\cdot p_\nu\right)-m_e^2p_\nu^{\mu}+\left[m_{\Xi^0}^2\left(p_e\cdot p_\nu\right)+\right.\\
- \quad & \left.\left.2\left(p_{\Xi^0}\cdot p_e\right)\left(p_{\Xi^0}\cdot p_\nu\right)+m_e^2\left(p_{\Xi^0}\cdot p_\nu\right)\right]\left(P_{\Xi^0}\right)_\nu g^{\mu\nu}\right\}+\\
+ \quad & \left[\frac{2\Re\left(G_1G_2\right)}{m_{\Xi^0}}\right]\left\{\left(P_{\Xi^0}\cdot p_e\right)\left[-m_{\Sigma^+}\left(p_{\Xi^0}\cdot p_\nu\right)-m_{\Xi^0}\left(p_{\Sigma^+}\cdot p_\nu\right)\right]p_e^{\mu}+\right.\\
+ \quad & \left(P_{\Xi^0}\cdot p_e\right)\left[-m_{\Sigma^+}\left(p_{\Xi^0}\cdot p_\nu\right)-m_{\Xi^0}\left(p_{\Sigma^+}\cdot p_e\right)-m_{\Xi^0}m_e^2\right]p_\nu^{\mu}+\\
+ \quad & \left(P_{\Xi^0}\cdot p_\nu\right)\left[-m_{\Sigma^+}\left(p_{\Xi^0}\cdot p_e\right)-m_{\Xi^0}\left(p_{\Sigma^+}\cdot p_\nu\right)\right]p_e^{\mu}+\\
+ \quad & \left(P_{\Xi^0}\cdot p_\nu\right)\left[-m_{\Sigma^+}\left(p_{\Xi^0}\cdot p_\nu\right)-m_{\Xi^0}\left(p_{\Sigma^+}\cdot p_e\right)-m_{\Xi^0}m_e^2\right]p_\nu^{\mu}+\\
+ \quad & \left[m_{\Xi^0}^2\left(m_{\Xi^0}-m_{\Sigma^+}\right)\left(p_e\cdot p_\nu\right)-2\left(m_{\Xi^0}-m_{\Sigma^+}\right)\left(p_{\Xi^0}\cdot p_e\right)\left(p_{\Xi^0}\cdot p_\nu\right)+\right.\\
+ \quad & \left.\left.m_e^2\left(m_{\Xi^0}-m_{\Sigma^+}\right)\left(p_{\Xi^0}\cdot p_\nu\right)\right]\left(P_{\Xi^0}\right)_\nu g^{\mu\nu}\right\}+\\
+ \quad & \left[\frac{2\Re\left(G_1G_3\right)m_e^2}{m_{\Xi^0}}\right]\left\{-m_{\Xi^0}\left(p_e\cdot p_\nu\right)p_\nu^{\mu}+\right.\\
- \quad & m_{\Sigma^+}\left(P_{\Xi^0}\cdot p_\nu\right)p_e^{\mu}+\left(P_{\Xi^0}\cdot p_\nu\right)\left(-m_{\Xi^0}-m_{\Sigma^+}\right)p_\nu^{\mu}+\\
+ \quad & \left.\left[m_{\Xi^0}\left(p_{\Sigma^+}\cdot p_\nu\right)-m_{\Sigma^+}\left(p_{\Xi^0}\cdot p_\nu\right)\right]\left(P_{\Xi^0}\right)_\nu g^{\mu\nu}\right\}+
\end{aligned}
$$

$$
\begin{aligned}
+ \quad & \left[\frac{(G_2)^2}{m_{\Xi^0}^2}\right]\left[2\left(p_{\Xi^0}\cdot p_e\right)\left(p_{\Xi^0}\cdot p_\nu\right)-m_{\Xi^0}^2\left(p_e\cdot p_\nu\right)\right]\cdot \\
\cdot \quad & \left\{\left(P_{\Xi^0}\cdot p_e\right)p_e^\mu+\left(P_{\Xi^0}\cdot p_e\right)p_\nu^\mu+\left(P_{\Xi^0}\cdot p_\nu\right)p_e^\mu+\right. \\
+ \quad & \left.\left(P_{\Xi^0}\cdot p_\nu\right)p_\nu^\mu+\left[\left(p_{\Xi^0}\cdot p_{\Sigma^+}\right)-m_{\Xi^0}m_{\Sigma^+}\right]\left(P_{\Xi^0}\right)_\nu g^{\mu\nu}\right\}+ \\
+ \quad & \left[\frac{2\Re\left(G_2G_3\right)m_e^2\left(p_{\Xi^0}\cdot p_\nu\right)}{m_{\Xi^0}^2}\right]\cdot \\
\cdot \quad & \left\{\left(P_{\Xi^0}\cdot p_e\right)p_e^\mu+\left(P_{\Xi^0}\cdot p_e\right)p_\nu^\mu+\left(P_{\Xi^0}\cdot p_\nu\right)p_e^\mu+\right. \\
+ \quad & \left.\left(P_{\Xi^0}\cdot p_\nu\right)p_\nu^\mu+\left[\left(p_{\Xi^0}\cdot p_{\Sigma^+}\right)-m_{\Xi^0}m_{\Sigma^+}\right]\left(P_{\Xi^0}\right)_\nu g^{\mu\nu}\right\}+ \\
+ \quad & \left[\frac{(G_3)^2 m_e^2\left(p_e\cdot p_\nu\right)}{m_{\Xi^0}^2}\right]\left\{\left(P_{\Xi^0}\cdot p_e\right)p_e^\mu+\right. \\
+ \quad & \left(P_{\Xi^0}\cdot p_e\right)p_\nu^\mu+\left(P_{\Xi^0}\cdot p_\nu\right)p_e^\mu+\left(P_{\Xi^0}\cdot p_\nu\right)p_\nu^\mu+ \\
+ \quad & \left.\left[\left(p_{\Xi^0}\cdot p_{\Sigma^+}\right)-m_{\Xi^0}m_{\Sigma^+}\right]\left(P_{\Xi^0}\right)_\nu g^{\mu\nu}\right\}+ \\
+ \quad & \left[-\Re\left(F_1G_1\right)2m_{\Xi^0}m_{\Sigma^+}\right]\left[\left(P_{\Xi^0}\cdot p_e\right)p_\nu^\mu-\left(P_{\Xi^0}\cdot p_\nu\right)p_e^\mu\right]+ \\
+ \quad & \left[\frac{2\Re\left(G_1F_2\right)}{m_{\Xi^0}}\right]\left\{\left(P_{\Xi^0}\cdot p_e\right)\left[-m_{\Xi^0}\left(p_{\Sigma^+}\cdot p_\nu\right)-m_{\Sigma^+}\left(p_{\Xi^0}\cdot p_\nu\right)\right]p_e^\mu+\right. \\
+ \quad & \left(P_{\Xi^0}\cdot p_e\right)\left[-m_{\Xi^0}\left(p_{\Sigma^+}\cdot p_\nu\right)-m_{\Sigma^+}\left(p_{\Xi^0}\cdot p_\nu\right)+\right. \\
+ \quad & \left.m_{\Xi^0}\left(p_{\Xi^0}\cdot p_{\Sigma^+}\right)+m_{\Xi^0}^2m_{\Sigma^+}\right]p_\nu^\mu+ \\
+ \quad & \left(P_{\Xi^0}\cdot p_\nu\right)\left[m_{\Xi^0}\left(p_{\Sigma^+}\cdot p_e\right)+m_{\Sigma^+}\left(p_{\Xi^0}\cdot p_e\right)+\right. \\
- \quad & \left.m_{\Xi^0}\left(p_{\Xi^0}\cdot p_{\Sigma^+}\right)-m_{\Xi^0}^2m_{\Sigma^+}\right]p_e^\mu+ \\
+ \quad & \left.\left(P_{\Xi^0}\cdot p_\nu\right)\left[m_{\Xi^0}\left(p_{\Sigma^+}\cdot p_e\right)+m_{\Sigma^+}\left(p_{\Xi^0}\cdot p_e\right)\right]p_\nu^\mu\right\}\}
\end{aligned} \tag{B.4}
$$

Bibliography

[1] J.R. Batley *et al.*, Phys. Lett. B, 544: 97-112 (2002).

[2] F.J. Gilman, K. Kleinknecht, B. Renk "The Cabibbo-Kobayashi-Maskawa quark-mixing matrix", Particle Data Book, Phys. Rev. D, Vol. 66: 113, (2002)

[3] M. Battaglia, L. Gibbons "Determination of $|V_{ub}|$", Particle Data Book, Phys. Rev. D, Vol. 66: 706, (2002)

[4] H. Leutwyler, M. Roos Z. Phys. C 25: 91 (1984)

[5] V. Cirigliano *et al*. Eur. Phys. J. C 23: 121 (2002)

[6] A. Sirlin, W.J. Marciano Phys. Rev. Lett. 56: 22 (1986)

[7] Yu.a. Mostovoi *et al*. Phys. Atomic Nucl. 64: 1955 (2001)

[8] A. Sher, *et al*. e-Print Archive: hep-ex/0305042

[9] By KLOE Collaboration (M. Moulson for the collaboration), To appear in the proceedings of 8th Conference on the Intersections of Particle and Nuclear Physics (CIPANP 2003), New York, New York: 19-24 May (2003). e-Print Archive: hep-ex/0308023

[10] J.F. Donoghue,B.R. Holstein, S.W. Klimt Phys. Rev. D 35: 934 (1987)

[11] N. Cabibbo, E.C. Swallow, R. Winston, "Semileptonic hyperon decays and CKM unitarity" e-Print Archive: hep-ph/0307214 (2003).

[12] H. Abele *et al*. Phys.Lett.B 407: 212 (1997)

[13] P. Liaud *et al*. Nucl. Phys. A 612: 53 (1997)

[14] A. Affolder *et al*. Phys. Rev. Lett. 82: 3751 (1999).

[15] A. Alavi-Harati proceedings to DPF99, hep-ex: 990301 (1999)

[16] "Hyperon Beta Decay: A Contemporary Review" presented at BEACH2002, 5th International Conference on Hyperons, charm and beauty hadrons. Vancouver June 25-29, (2002)

[17] R. Flores-Mendieta, A. Garcia and G. Sanchez-Colon, Phys.Rev.D54: 6855-6860, (1996).

[18] F. Schlumpf, Phys. Rev. D 51: 2262 (1995).

[19] A. Krause, Helv. Phys. Acta 63: 3 (1990).

[20] J. Anderson and M.A. Luty, Phys. Rev. D 47: 4975 (1993).

[21] A. Alavi-Harati *et al*. Phys. Rev. Lett. 87: 132001 (2001).

[22] A. Garcia, P. Kielanowsky "The Beta Decay of Hyperons", Lecture Notes in Physics Vol. 222 (Springer-Verlag, Berlin, 1985).

[23] A. Sirlin, Rev. Mod. Phys. 50: 573 (1978)

[24] N. Cabibbo, E.C. Swallow, R. Winston "Semileptonic hyperon decays", Submitted to Annual Review of Nuclear and Particle Physics e-Print Archive: hep-ph/0307298

[25] M. Gaillard and G. Sauvage, Ann.Rev.Nucl.Part.Sci.34: 351, (1984).

[26] V. Linke "Leptonic decays of polarized baryons", Nuclear Physics B. 9: 141-152, (1969)

[27] S. Bright *et al*. "Effective hamiltonian approach to hyperon beta decay with final state baryon polarization", Physics Review D. 60: 117505, (1999) - Erratum 62: 059904, (2000)

[28] T. Alexopoulos, A.R. Erwin (Wisconsin U., Madison). Sep 1999. Prepared for Hyperon 99: Hyperon Physics Symposium, Batavia, Illinois, 27-29 In "Batavia 1999, Hyperon physics" 48-52.

[29] E.D. Commins, "Baryon decay parameters", Particle Data Book, Phys. Rev. D, Vol. 66: 767, (2002).

[30] E.D. Commins and P.H. Bucksbaum, "Weak interactions of Leptons and Quarks" (Cambridge University Press) Cambridge, England, (1983).

[31] A. Garcia, Phys. Lett. B 105: 224 (1981).

[32] A. Garcia, Phys. Rev. D 25: 1348 (1982).

[33] V. Fanti *et al*. Phys.Lett.B 465: 335, (1999).

[34] "Nonlinear resonances" CERN Accelerator School: Course on Advanced AcceleretorPhysics (CAS), Rhodes; Greece, 20 Sep -1 Oct 1993.

[35] A. Lai *et al*., Eur. Phys. J. C 22, 231-255, (2001).

[36] N. Doble *et al*., Nucl. Instr. Meth. B 119: 181-191, (1996).

[37] P. Grafstrom *et al*., Nucl. Instr. Meth. A 370: 413-424 (1994).

[38] R. Moore *et al*., "Measurement of pair-production by high energy photons in an aligned tungsten crystal" Nucl. Instrum. Methods Phys. Res., B 119: 149-155 (1996).

[39] NA48 Torino Group. "NA48 Anticounters: Design, Construction, Installation ant 93 -94 Test Beam" NA48 note 96-03, (1996).

[40] D. Deberede *et al* "High resolution drift chambers for the NA48 experiment at CERN Nucl. Instrum. Meth., A 367: 88, (1995).

[41] E. Griesmayer *et al*. "Comparison of field calculations and measurements of a spectrometer magnet" Nucl Instrum Meth, A 361: 466, (1995).

[42] J. Ocariz "The NA48 liquid krypton calorimeter description and performances" hep-ex: 9901013 (1999).

[43] S. Palestini "The liquid kripton calorimeter for experiment CERN-NA48" Nucl. Instrm, Meth. A 367: 263, (1995).

[44] F Bal *et al*. "The Calorimeter Pipeline Digitizer CPD F690 C". NA48 note 97-35, (1997).

[45] Perugia and Cagliari Groups. "The NA48 charged hodoscope" NA48 note 94-37, (1994).

[46] A. Lai and L. Musa, "Pipeline Memory Boards Specs" NA48 note 95-96, (1995).

[47] G. Anzivino, P. Lubrano and M. Pepe "Neutral Hodoscope Calibration and Preliminary Results from the 1996 Run" NA48 note 97-22, (1997).

[48] G. Fisher *et al*. Nucl. Instrum. Methods Phys. A 419: 695, (1998).

[49] M. Jeitler *et al*. "The clock and control signal distribution system for the NA48 experiment" Nucl. Instrum. Methods Phys. Res., A 400 no.1: 101-106, (1997).

[50] R. Arcidiacono *et al*. "The Trigger Supervisor of the NA48 experiment at the CERN SPS" Nucl.Instr.Meth. A,443 no.1: 20-26, (2000).

[51] S. Anvar *et al*. "The charged trigger system of NA48 at CERN" Nucl. Instrum. Methods Phys. Res., A 419 no.2-3: 686-694, (1998).

[52] M. Wittgen *et al*. "The NA48 event-building PC farm" IEEE Trans. Nucl. Sci. 47: 348-352 (2000).

[53] M. De Beer and F. Derue "NASIM User's guide" NA48 note 00-23, (2000).

[54] R. Brun, R. Hagelberg, M. Hansroul, J.C. Lassalle, CERN-DD-78-2-REV: 76pp, (1978).

[55] A. Michetti, private comunications

[56] L.J. Carlson, R.J. Oakes, C.R. Willcox Phys. Rew. D 37: 3197 (1988).